Simulation of Particle Fluxes
at the DESY-II Test Beam Facility

Anne Schütz

Master's Thesis

Karlsruhe Institute of Technology
Department of Physics
Institute of Experimental Nuclear Physics (IEKP)

In collaboration with:
Deutsches Elektronen-Synchrotron (DESY)

Reviewer: Prof. Dr. Günter Quast (IEKP)
Second reviewer: Prof. Dr. Eckhard Elsen (DESY)
Advisor: Dr. Marcel Stanitzki (DESY)

February 23, 2015

I declare that I have developed and written the enclosed thesis completely by myself, and have not used sources or means without declaration in the text.

Hamburg, February 23, 2015

. . . .
(Anne Schütz)

Kurzzusammenfassung

Im Zuge dieser Masterarbeit zur Simulation der Teilchenflüsse am DESY-II Teststrahl wurde die Teststrahlerzeugung mit dem Simulationsprogramm SLIC simuliert, welches auf Geant4 basiert. Geant4 macht sich Monte Carlo Algorithmen zunutze, um Teilchen und ihre Wechselwirkung mit Detektormaterialien realitätsnah zu simulieren.

Nach einem kurzen theoretischen Umriss der physikalischen Prozesse, die für die Strahlerzeugung am DESY-II Teststrahl relevant sind, wird das Prinzip der Teststrahlerzeugung genauer erläutert. Daraufhin folgt eine Beschreibung der verwendeten Programme, sowie der prinzipiellen Funktionsweise einer Monte Carlo Simulation mit Geant4. Die Simulation des Teststrahls ist gemäß des Ablaufs der Strahlerzeugung gegliedert. Dementsprechend wird zunächst auf die Simulation des Strahles des DESY-II Synchrotrons eingegangen, bevor sukzessive die Simulation der einzelnen Komponenten erklärt wird, die zur Strahlerzeugung verwendet werden. Eine zusätzliche Leistung dieser Masterarbeit ist die Visualisierung des Teilchenflusses und der Teilchenspuren entlang des simulierten Teststrahles. Auf den entstandenen Teilchenflusskarten werden schließlich die einzelnen Schritte der Strahlerzeugung sichtbar, da die Teilchenspurdichte in Materialien und Magnetfeldern variiert.

Hauptresultat der Simulation sind Diagramme zur Strahlzusammensetzung und Energiespektrum des finalen Teststrahles, die zum Vergleich zu gemessenen Strahleigenschaften und damit zum besseren Verständnis der physikalischen Prozesse am Teststrahl dienen. Diese DESY-II Teststrahlsimulation wird in Zukunft bei technischen Verbesserungen der Teststrahlkompontenten behilfreich sein.

Abstract

In the course of this Master's thesis *"Simulation of Particle Fluxes at the DESY-II Test Beam Facility"* the test beam generation for the DESY test beam line was studied in detail and simulated with the simulation software SLIC. SLIC uses the GEANT4 toolkit for realistic Monte Carlo simulations of particles passing through detector material.

After discussing the physics processes relevant for the test beam generation and the principles of the beam generation itself, the software used is introduced together with a description of the functionality of the GEANT4 Monte Carlo simulation. The simulation of the test beam line follows the sequence of the test beam generation. Therefore, it starts with the simulation of the beam bunch of the synchrotron accelerator DESY-II, and proceeds step by step with the single test beam line components. An additional benefit of this thesis is the provision of particle flux and trajectory maps, which make fluxes directly visible by following the particle tracks through the simulated beam line. These maps allow us to see each of the test beam line components, because flux rates and directions change rapidly at these points. They will also guide the decision for placements of future test beam line components and measurement equipment.

In the end, the beam energy and its spread, and the beam rate of the final test beam in the test beam area were studied in the simulation, so that the results can be compared to the measured beam parameters. The test beam simulation of this Master's thesis will serve as a key input for future test beam line improvements.

Contents

List of Figures

Chapter 1.

Introduction

Every individual component of each technical device is tested during its research and development phase, regardless of the purpose the device serves. The environment in which it is tested is supposed to mimic the realistic conditions to which the device will be exposed.

Therefore, for the field of particle detector development, it is important to test new sensors and their performance in the most realistic conditions possible, and hence expose it to a particle beam. In contrast to radioactive sources or cosmic rays, a test beam is a well defined particle source. The beam has a small energy spread, and provides a collimated timed stream of minimum ionising particles at high rates. Its energy and rate are adjustable and can therefore be adapted to the needs of the test beam user and their devices. Beyond that, in order to be able to provide optimal testing environments the attributes of the test beam should be very well known.

DESY (Deutsches Elektronen-Synchrotron) is one of very few research institutes world wide with a test beam facility. The DESY-II test beam facility has three independent test beam lines and provides users from all over the world with electron or positron beams for the purpose of testing sensors for particle tracking systems and calorimeters. The largest part of the DESY-II test beam user community is represented by the Large Hadron Collider (LHC) experiments. The groups are testing new sensors and detectors for the LHC phase I and II upgrades that is planned to take place in 2017 and 2022.

The electron/positron beams that are provided have an energy up to $6.3\,\mathrm{GeV}$ and a rate between $1\,\mathrm{Hz}$ and far beyond $10\,\mathrm{kHz}$. Users are able to adjust the energy distribution and rate of the test beam as needed. As there are only a few test beam facilities in the world with beam energies higher than $1\,\mathrm{GeV}$, it is in high demand.

DESY was founded in 1959 and is a German research centre of the Helmholtz Association [3], which is the largest scientific organisation in Germany. Its campuses are located in Hamburg and Zeuthen near Berlin. At the site in Hamburg, DESY operates several particle accelerators for high energy physics. Synchrotron radiation from the accelerators is also used for photon science.

One of the currently operating accelerators is DESY-II. It is an electron/positron synchrotron and serves as an injector for PETRA-III, a synchrotron photon source with currently the highest brilliance in the world. Additionally, DESY-II is the source for the DESY test beams, which are parasitically produced.

In Figure 1.2, the three test beam lines originating from the DESY-II synchrotron are illustrated. The generation of the test beam includes several steps. First, bremsstrahlung photons are created by letting the DESY-II beam bunch hit a primary target. The photons are then converted to electron/positron pairs due to pair production. This electron/positron beam is then widened into a particle fan after
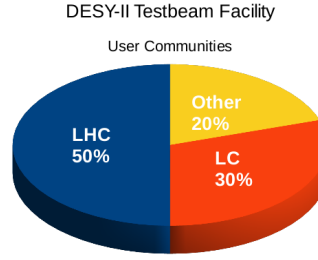
Figure 1.1.: *Chart of fractions of the DESY-II test beam user community in 2013 and the beginning of 2014. [2] Most of the test beam users were from LHC experiments, in particular the groups ATLAS and CMS testing pixel sensors for their tracking systems. 30 % of all users were collaborations for the new International Linear Collider (ILC). Other groups included Belle-II, FAIR, XFEL and ITER.*

entering a dipole magnet, behind which a collimator is placed. The users can select the final beam energy by adjusting the current through the magnet and therefore the particle deflection. The steps are described in detail in Chapter 3.2.
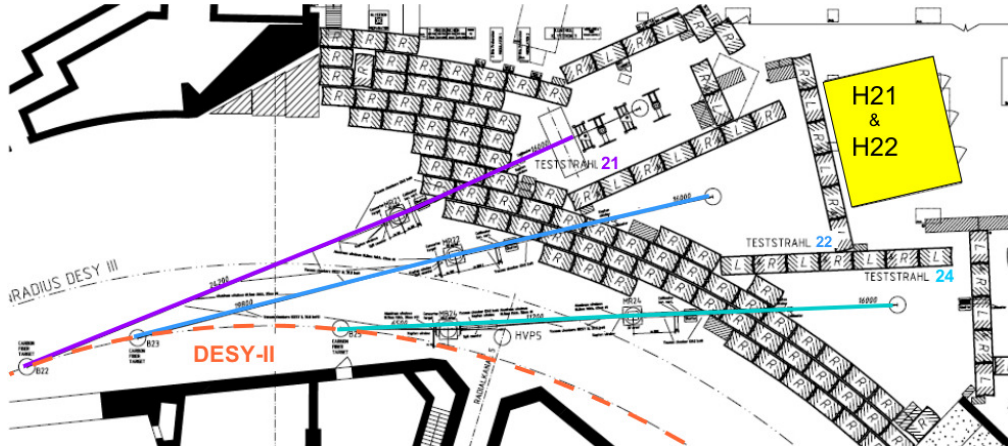
Figure 1.2.: *A map of the DESY test beam lines in the DESY-II tunnel from 2002.[4] The current state of the beam lines deviates slightly from the shown state. Unlike the Figure shows, the particles travel not only through evacuated beam pipes but also through the air of the DESY-II tunnel.*

The goal of this Master's thesis is a realistic and detailed simulation of the test beam generation. With the help of the simulated data, deeper understanding is gained about the beam attributes for all possible settings: the particle fluxes in the accelerator tunnel, the beam energy distributions, and the beam rate for the final electron/positron beam. At the same time the information from the simulation serves as the key input for future test beam line improvements.

Future users will benefit from the better understanding and modelling of the provided test beams and can optimise their experimental set-up in order to reduce their systematic and statistical uncertainties. The simulation can be used as an input for other Monte Carlo simulations and studies. This will allow future users to do even more accurate simulation/data comparisons, giving higher confidence to the physics results obtained.

2 Chapter 2.

Passage of particles through matter and fields

This chapter introduces the principle of particle interactions in material relevant for the physics pro-
cesses at the DESY-II test beam, such as for the beam generation and propagation. Additionally,
hadronic interactions, synchrotron radiation and charged particle deflection in a homogeneous magnetic
field are discussed. Table A.1 in Appendix A.1.1 lists several constants and their values, which are used
in the following sections.

2.1. Particle interactions in material

Since the test beam generation is based on electromagnetic particle processes, this section covers the
theory of interactions of photons and charged particles, especially of electrons, positrons, and protons,
as they pass through matter. That includes the definition of the radiation length, the stopping power,
bremsstrahlung, photon conversion, and multiple scattering.

2.1.1. Radiation length

The radiation length X_0 is a material specific constant and has two definitions [5, page 404]:

- In terms of electrons and other charged particles, the radiation length is the mean length after
  which the particle energy E_0 is reduced to E_0/e due to bremsstrahlung (with the Euler's number
  e).

- In terms of photons, the radiation length is 7/9 of the mean free path for pair production.

The predominant pair production for high energy photons is into an e^+e^- pair. The radiation length
can be estimated by the following Equation 2.1 (cf. [5, page 404]). The values for α, A, Z, N_A and r_e
can be found in Table A.1.

$$X_0 = \frac{A}{4\alpha N_A r_e^2 Z^2 \ln(183/Z^{1/3})} \tag{2.1}$$

X_0 is measured in [g cm^{-2}] and is also the scale length used for cascades of electromagnetic showers.
The main dependency of the radiation length is the atomic number Z. A photon, for instance, which

passes through matter with a high atomic number, is therefore stopped after a shorter distance than in a material with a small atomic number.

2.1.2. Stopping power

Charged particles passing through matter interact with the bound electrons in the material. The result is excitation or ionisation of the atoms and energy loss of the incident particle. The "Bethe equation", Equation 2.2, describes the mean rate of energy loss per traversed matter for charged heavy particles for $0.1 \gtrsim \beta\gamma \lesssim 1000$. [5, page 399]

$\left\langle -\frac{\mathrm{dE}}{\mathrm{dx}} \right\rangle$ has the unit $[\mathrm{MeVg}^{-1}\mathrm{cm}^2]$, as $\mathrm{x} = \mathrm{X} \cdot \rho$, where X is the distance travelled in matter.

$$\left\langle -\frac{\mathrm{dE}}{\mathrm{dx}} \right\rangle [\mathrm{MeVg}^{-1}\mathrm{cm}^2] = Kz^2\frac{Z}{A}\frac{1}{\beta^2}\left[\frac{1}{2}\ln\frac{2m_ec^2\beta^2\gamma^2 W_{max}}{I^2} - \beta^2 - \frac{\delta(\beta\gamma)}{2}\right] \qquad (2.2)$$

The dependency of the "Bethe formula" on β^{-2} can be interpreted as the effect that low energy particles remain longer in the electric field of the atoms. Their energy depositions are therefore higher. The smaller β, the higher the amount of energy being deposited.

In a cloud chamber, for example, this effect becomes visible. Particles with smaller velocity create thicker tracks, because they lose their energy over a shorter distance. Alpha and beta particles from natural background radiation are therefore easily distinguishable. In terms of energy loss due to ionisation, beta particles, i.e. electrons or positrons, behave differently because of their special qualities. This will be discussed in more detail below.

The $\beta\gamma$ term causes a relativistic increase, for $\beta\gamma > 4$. For relativistic particles, the electric field of the atomic shell is compressed and the transverse electric field intensified, as can be seen in Figure 2.1. Therefore, the energy loss is higher because of this relativistic increase.

Figure 2.1.: *Compression and intensification of the transverse electric field around an atom for a relativistic particle.*

The density effect term $\delta/2$ is a correction for distant-collision contributions, which reduce the stopping power. It is necessary to be included in the "Bethe formula" for high energy particles, as their impact parameter increases with the energy. The particle field extends and therefore the smallest distance possible between the particle and the atom increases. The charge density of the electrons of the atomic shell shields the electric field of the incident particle, so that the electric field has less effect on the atom than taken into account in the formula.

For low energy particles, a shell correction term $-\frac{C}{Z}$ is to be included instead of the density effect term, where C is a constant. The approximation that the atomic electrons are at rest, is no longer appropriate, so that atomic absorption and excitation processes have to be taken into account.

The mean excitation energy I is an empirically attained number. Tables with values gained from experimental stopping power measurements are available on the web page for "Physical Reference Data"

of "The National Institute of Standards and Technology" (NIST) [6].

The stopping power for electrons differs from the stopping power for heavy particles due to the kinematics and the fact that incident and ionised particles are both electrons. The "Bethe formula" is then to be written as follows [5, page 404]:

$$\left\langle -\frac{\mathrm{dE}}{\mathrm{dx}} \right\rangle = \frac{1}{2}K\frac{Z}{A}\frac{1}{\beta^2}\left[\ln\frac{m_ec^2\beta^2\gamma^2\{m_ec^2(\gamma-1)/2\}}{I^2} + (1-\beta^2) - \frac{2\gamma-1}{\gamma^2}\ln2 + \frac{1}{8}\left(\frac{\gamma-1}{\gamma}\right)^2 - \delta\right] \tag{2.3}$$

Figure 2.2 shows the normalised energy loss per radiation length for electrons and positrons in lead. The energy loss due to ionising dominates up to an energy of about 10 MeV and is then outranged by the energy loss due to bremsstrahlung. In Figure 2.3, one can see that this is also true for higher ranges up to 10 GeV. It is to be noted, that in Figure 2.3 the energy loss is neither normalised nor divided by the radiation length of lead. However, it becomes clear that electrons are minimal ionising particles (MIPs) for energies higher than 10 MeV. This progression of the "Bethe formula" is in general true for all materials, only the energy scale varies since the energy loss is dependent on some material specific factors, as explained above.
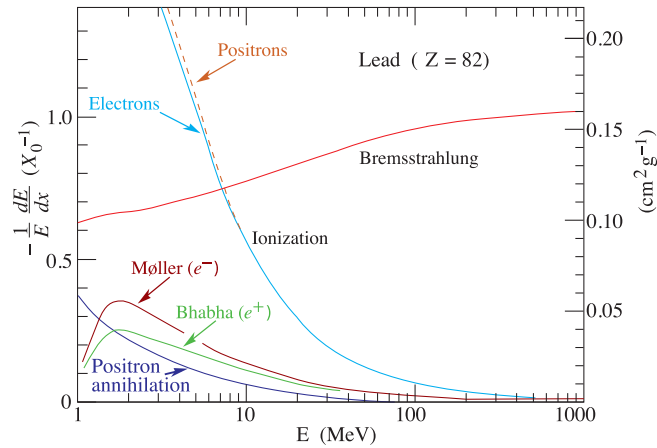
Figure 2.2.: *Normalised energy loss per radiation length $\frac{1}{\mathrm{E}}\frac{\mathrm{dE}}{\mathrm{dx}}(X_0^{-1})$ in lead as a function of the energy of electrons/positrons. The y-axis on the right hand side shows the normalised energy loss not divided by the radiation length. The radiation length for lead is X_0=6.37 g/cm^2. [5, page 404]*

2.1.3. Bremsstrahlung

Bremsstrahlung is the dominant physics process for high energy charged particles. Due to this, the curve for the energy loss is increasing for higher energies, as can be seen in Figure 2.2 and 2.3. In
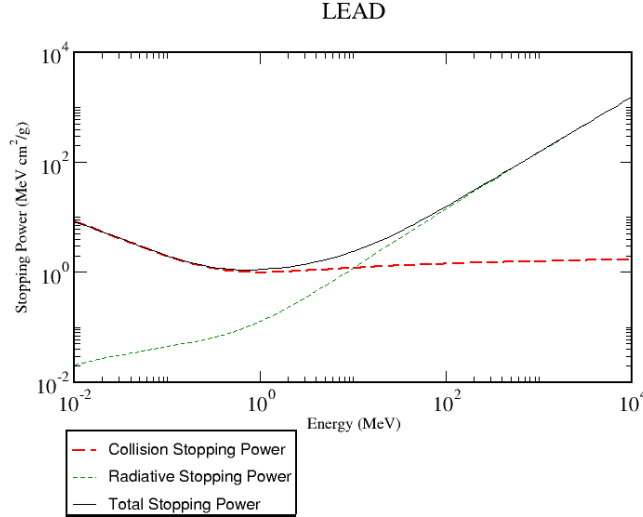
Figure 2.3.: *Energy loss $\frac{dE}{dx}$ in lead as a function of the energy of electrons. [7] The collision stopping power stands for the energy loss due to ionisation, the radiative stopping power for the energy loss due to bremsstrahlung.*

Figure 2.3, the increase is linear due to the approximation [5, page 406]:

$$\left|\frac{dE}{dx}\right|_{brems} = \frac{E}{X_0} \tag{2.4}$$

An incoming high energy electron is deflected by an atomic nucleus and decelerated at the same time. The kinetic energy, which the electron loses, is converted into a photon. The photon is boosted in approximately the same direction as the initial direction of the electron. The electron produces bremsstrahlung photons until it leaves the material or is stopped.

The bremsstrahlung spectrum is continuous and shows a $\frac{1}{E}$ dependency. The number of photons produced by an electron with energy E_0 in a target with thickness dt and in an energy interval dk can be expressed by Equation 2.5. [8, page 833]
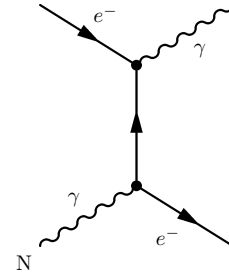
Figure 2.4.: *The first order Feynman diagram of the generation of bremsstrahlung photons. (cf. [9, page 905])*

$$\rho(E_0, k)dtdk = \frac{d\sigma_b}{dk}\frac{N_A}{A}X_0dtdk \tag{2.5}$$

with the cross section $\frac{d\sigma_b}{dk}$ given in Equation 2.6, where $y = \frac{k}{E}$ is the ratio of photon energy transferred from the electron and the initial electron energy. [8, page 831]

$$\frac{d\sigma_b}{dk} = 4\alpha r_e^2 k^{-1} \left[\left(\frac{4}{3} - \frac{4}{3}y + y^2 \right) \left[Z^2 \left(L_{rad} - f \right) + Z L'_{rad} \right] + \frac{1}{9} \left(1 - y \right) \left(Z^2 + Z \right) \right] \tag{2.6}$$

The constants L_{rad} and L'_{rad} are element specific and can be calculated with [5, page 404]:

$$L_{rad} = ln(184.15 Z^{-1/3}) \tag{2.7}$$

$$L'_{rad} = ln(1194 Z^{-2/3}) \tag{2.8}$$

For the case of a very thin target ($dt \to d \ll X_0$) one can make an approximation for the number of emitted photons with an energy between k_{min} and k_{max} [5, page 405]:

$$N_\gamma = \frac{d}{X_0} \left[\frac{4}{3} ln \left(\frac{k_{max}}{k_{min}} \right) - \frac{4(k_{max} - k_{min})}{3E} + \frac{k_{max}^2 - k_{min}^2}{2E^2} \right] \tag{2.9}$$

In both Equations 2.5 and 2.9 the characteristic $\frac{1}{E}$ dependency of the bremsstrahlung spectrum is clear. Equation 2.9 will serve as the fit function for the bremsstrahlung spectrum of the simulated photons occurring in the course of the DESY test beam generation (see Chapter 5.2).

2.1.4. Photon conversion

Energy loss for photons is caused by the photoelectric effect and the Compton effect for low energy photons. For high energy photons the dominant process is pair production especially to an electron/positron pair.

Figure 2.5 shows the first order Feynman diagram for photon conversion to an $e^+ e^-$ pair in the presence of atoms in matter. It can be interpreted as the annihilation of the photon with a photon, which is produced in the material, to a lepton pair, predominantly an $e^+ e^-$ pair. The energy spectrum of the created electrons/positrons is therefore continuous.
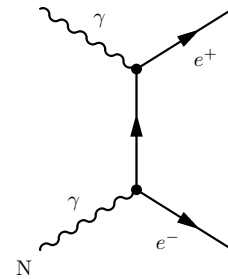
Figure 2.5.: *The first order Feynman diagram of the conversion of a photon into an electron/positron pair. (cf. [9, page 905])*

Figure 2.6 shows that the probability for pair production increases with the photon energy. The fact that the slope of the probability curve varies for different materials leads to the conclusion that the cross section is dependent on the material: [5, page 406]

$$\frac{d\sigma}{dx} = \frac{A}{X_0 N_A} [1 - \frac{4}{3} x (1 - x)] \tag{2.10}$$

With $x = E/k$ and E being the transferred energy to the produced electron/positron and k being

the initial energy of the incident photon, Equation 2.10 leads to the following high energy limit to the cross section, as x can be maximal unity:

$$\sigma = \frac{7}{9} \frac{A}{X_0 N_A} \tag{2.11}$$
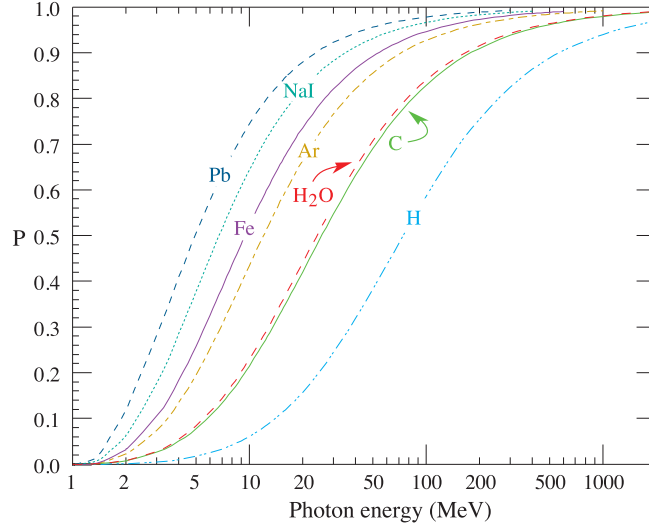
Figure 2.6.: *The probability P that a photon interaction is a conversion to an $e^+ e^-$ pair, for different materials. The other possible interaction in the shown energy range is Compton scattering. Between 10 and 20 MeV photonuclear absorption gives a small contribution to the possible photon interactions. [5, page 406]*

2.1.5. Multiple scattering

The passage of particles through matter can lead to multiple elastic and inelastic collisions with small changes of direction. Although the scattering particles can lose energy due to inelastic collisions, one has to differentiate between multiple scattering and the energy loss due to ionisation described by the "Bethe equation". The loss in the particle momentum of the scattering particle is arbitrary and leads to small atomic displacements or excitation of an electron in the atomic shell. The incident particle continues its passage with a small change of direction. The angle θ_{plane}, which is illustrated in Figure 2.7, is the deflection angle in the same plane that the particle is incident. θ_{plane} is Gaussian distributed and its RMS value $\theta_0 = \theta_{plane}^{RMS}$ can be defined with the "Highland formula" [5, page 403]:

$$\theta_0 = \frac{13.6\,[\text{MeV}]}{\beta c p} z \sqrt{\frac{x}{X_0}} \left[1 + 0.038 ln \left(\frac{x}{X_0} \right) \right] \tag{2.12}$$

In Equation 2.12 the momentum of the incident particle is given by p, the velocity by βc and its charge number by z, x is the thickness of the medium and X_0 its radiation length which was defined in Section 2.1.1.
Equation 2.12 implies that the smaller the radiation length X_0, the broader the Gaussian distribution of θ_{plane} is. The particle has therefore a higher probability to be more deflected. The dependency

$\theta_0 \propto 1/p$ can be interpreted such that the distribution is broader for low energy particles, as they are more strongly influenced by the Coulomb fields of the atoms in the material, also leading to a larger width of the scattering distribution.

For thin materials, i.e. small x, θ_0 is small, the particles are only slightly deflected.
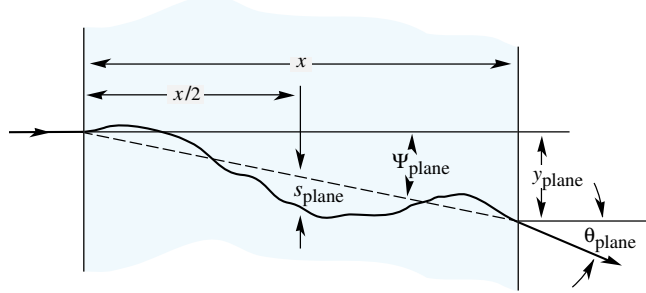
Figure 2.7.: *A scheme of multiple Coulomb scattering in matter. x is the distance in the medium, after which the incident particle is deflected by the angle θ_{plane}. Equation 2.12 describes the RMS value of θ_{plane}, e.g. $\theta_0 = \theta_{plane}^{RMS}$.*

2.2. Synchrotron radiation

The DESY test beam lines originate from the DESY-II synchrotron ring, which emits synchrotron radiation also along the test beam lines. As the photons interact with particles and materials, it is important to study the origin of the synchrotron radiation and its energy spectrum.

2.2.1. Synchrotron radiation power

Accelerated charged particles emit electromagnetic radiation, the synchrotron radiation. Both acceleration forms, transverse and parallel to the direction of movement, contribute to the synchrotron radiation. However, only the transverse radiation power leads to a loss in the kinetic energy of the charged particle, as the loss due to longitudinal acceleration is negligible.

The total synchrotron radiation power can be written as shown in Equation 2.13 [10, page 31]:

$$P_s = \frac{e^2 c}{6\pi\epsilon_0} \frac{1}{(m_0 c^2)^2} \gamma^2 \left[\left(\frac{d\vec{p}}{dt} \right)^2 - \frac{1}{c^2} \left(\frac{dE}{dt} \right)^2 \right] \tag{2.13}$$

In the case of linear acceleration, the particle energy gained per distance is known, so that the radiated power is found to be:

$$P_s = \frac{e^2 c}{6\pi\epsilon_0 (m_0 c^2)^2} \left(\frac{dE}{dx} \right)^2 \tag{2.14}$$

The radiated loss due to linear acceleration is negligible, which can be shown by the example of an accelerator with gained energy per metre of $\frac{dE}{dx} \approx 15\,\text{MeV/m}$. With Equation 2.14 the radiated power is calculated to be about $4 \cdot 10^{-17}$ Watts.

If the particles are bent perpendicular to the direction of motion, the particle energy does not change

and the synchrotron radiation power for the transverse acceleration can be written as [10, page 33]:

$$P_s = \frac{e^2 c}{6\pi\epsilon_0} \frac{1}{(m_0 c^2)^4} \frac{E^4}{R^2} \tag{2.15}$$

With this radiation power, one can calculate the energy ΔE that the particles lose after one turn in a synchrotron accelerator with radius R:

$$\begin{aligned}
\Delta E &= \oint P_s dt \\
&= P_s \cdot T \\
&= P_s \frac{2\pi R}{c} \\
\rightarrow \Delta E &= \frac{e^2}{3\epsilon_0 (m_0 c^2)^4} \frac{E^4}{R}
\end{aligned} \tag{2.16}$$

In terms of operating such a synchrotron accelerator, the beam bunch has to gain at least an energy of ΔE per turn, in order to counteract the losses due to synchrotron radiation. Due to the E^4 dependency, synchrotron accelerators have to have a large radius to compensate the energy. The higher the energy, the larger the radius has to be.

There is the $1/m^4$ dependency, which causes the extreme difference of synchrotron radiation power radiated from protons compared to electrons that are accelerated along a storage ring of radius R.[1] Table 2.1 gives the energy losses per turn for the DESY-II synchrotron ring as well as for the LHC. For comparison, the energy loss for the LHC was calculated for the case of accelerated protons and accelerated electrons.

	E [GeV]	R [m]	ΔE [MeV]
DESY-II (Electrons/positrons)	6.3	46.60	2.96
LHC (Protons)	7000	2804	$6.59{\cdot}10^{-3}$
LHC (Electrons)	7000	2804	$7.49{\cdot}10^{10}$
LEP	105	2804	$3.79{\cdot}10^3$

Table 2.1.: *Table of energy loss per turn due to synchrotron radiation for DESY-II and LHC (as a proton accelerator and only for comparison as an electron accelerator).*

2.2.2. Synchrotron radiation cone

In the centre of mass frame K' of an relativistic electron emitting synchrotron radiation, the radiation is similar to the radiation of a Hertz dipole. In the left part of Figure 2.8a the characteristic donut shape is shown. After the Lorentz transformation to the laboratory frame K, the spacial distribution of the synchrotron radiation is peaked in the forward direction tangentially to the beam path, in the

---

[1]With the same conditions and in the same storage ring of radius R, the difference in radiated power originates simply from the large difference in mass of protons and electrons: $\frac{P_{s,e}}{P_{s,p}} = \frac{m_p^4}{m_e^4} \approx \frac{(1836 m_e)^4}{m_e^4} \approx 1.13 \cdot 10^{13}$
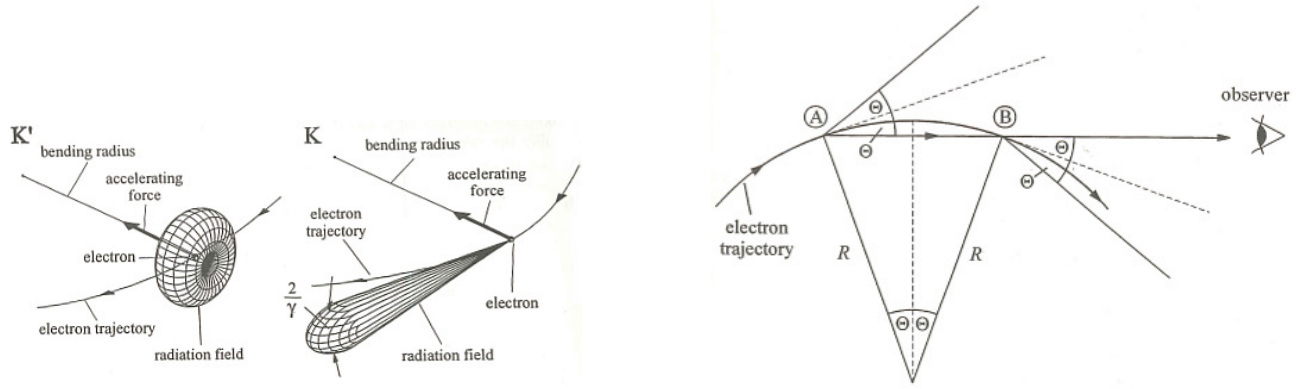
(a) *The synchrotron radiation is similar to a Hertz dipole in the frame of reference K'. When the frame is Lorentz transformed to the centre of mass frame K of the relativistic electron, the synchrotron radiation gets its characteristic cone shape sharply peaked in the direction of acceleration.*

(b) *Scheme of the emission of synchrotron radiation tangentially to the circular beam path. The synchrotron radiation cone has an opening angle of 2θ with $\theta = arctan\left(\frac{1}{\gamma}\right)$.*

Figure 2.8.: *Theoretical conceptions of synchrotron radiation emission in a cone shape and derivation of its opening angle θ. [10, page 36 ff]*

direction of acceleration. The radiation cone has an opening angle of *2θ* with [10, page 36]:

$$tan\theta = \frac{1}{\gamma} \tag{2.17}$$

The opening angle θ is also illustrated in Figure 2.8b, with which one can derive the pulse length. The pulse length is the time, during which an observer can see the radiation cone of a passing electron. The pulse length is approximately $\Delta t \approx \frac{4R}{3c\gamma^3}$, from which the characteristic and the more commonly used critical frequency of the synchrotron radiation are obtained [10, page 38]:

$$\omega_{char} = \frac{2\pi}{\Delta t} \qquad\qquad = \frac{3\pi c\gamma^3}{2R} \tag{2.18}$$

$$\omega_c = \frac{\omega_{char}}{\pi} \qquad\qquad = \frac{3c\gamma^3}{2R} \tag{2.19}$$

The critical frequency is commonly used for specifying the synchrotron radiation spectrum of an accelerator storage ring, since it marks the frequency over which half of the total synchrotron power is radiated.

The critical energy is therefore given by:

$$E_c = \hbar\omega_c = \frac{3\hbar c\gamma^3}{2R} \tag{2.20}$$

2.2.3. Synchrotron radiation spectrum

The spectral photon density of synchrotron radiation emitted by relativistic electrons that are deflected by a homogeneous magnetic field can be expressed by Equation 2.21 with the critical frequency ω_c from Equation 2.19. [10, page 38]

$$\frac{d\dot{N}}{d\epsilon/\epsilon} = \frac{P_0}{\hbar\omega_c} S_s\left(\frac{\omega}{\omega_c}\right) \tag{2.21}$$

This formula for the spectral photon density contains a spectral function S_s next to the total radiation power from N electrons $P_0 = N\frac{e^2c\gamma^4}{6\pi\epsilon_0 R^2}$, which is directly attained from Equation 2.15. The course of the spectral function S_s shown in Figure 2.9 is responsible for the characteristic form of the synchrotron radiation spectrum, which is plotted for the DESY-II synchrotron accelerator in Figure 2.10.
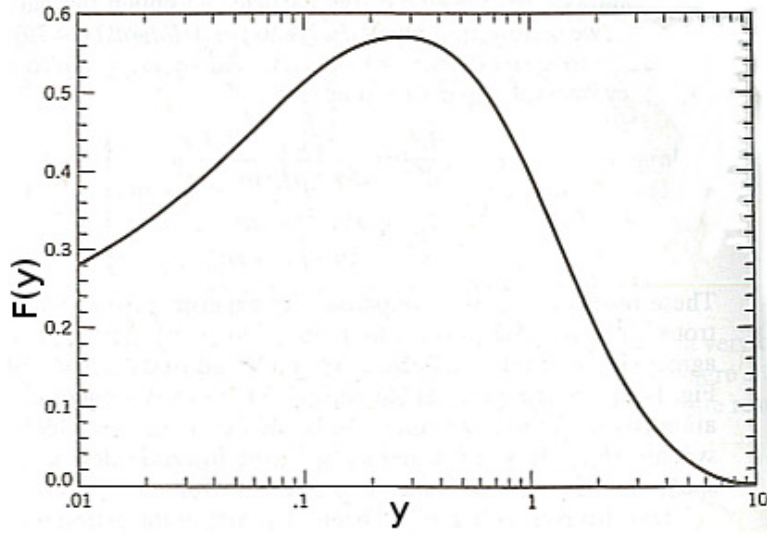
Figure 2.9.: *The synchrotron radiation density $\frac{d\dot{N}}{d\epsilon/\epsilon}$ contains the spectral function S_s, a function of $y = \omega/\omega_c$.*
$S_s(y) = \frac{9\sqrt{3}}{8\pi} y \int\limits_{y}^{\infty} K_{5/3}(x)dx$ with the modified Bessel function $K_{5/3}$. The Figure shows the normalised synchrotron spectral function, here named as $F(y) = S_s(y)$, with a logarithmic x-axis. [11, 682]

2.3. Hadronic interactions

Not only electromagnetic but also hadronic processes are relevant for the test beam generation at DESY, since secondary particles are created in the interactions of the test beam particles with matter, e.g. the collimators in the beam line. To understand how the secondary particles affect the test beam generation and the beam purity, it is important to look at hadronic interactions.
Heavy charged particles, like charged hadrons, have significantly different interaction and energy loss signatures than electrons, for example. This section discusses briefly the stopping power of hadrons
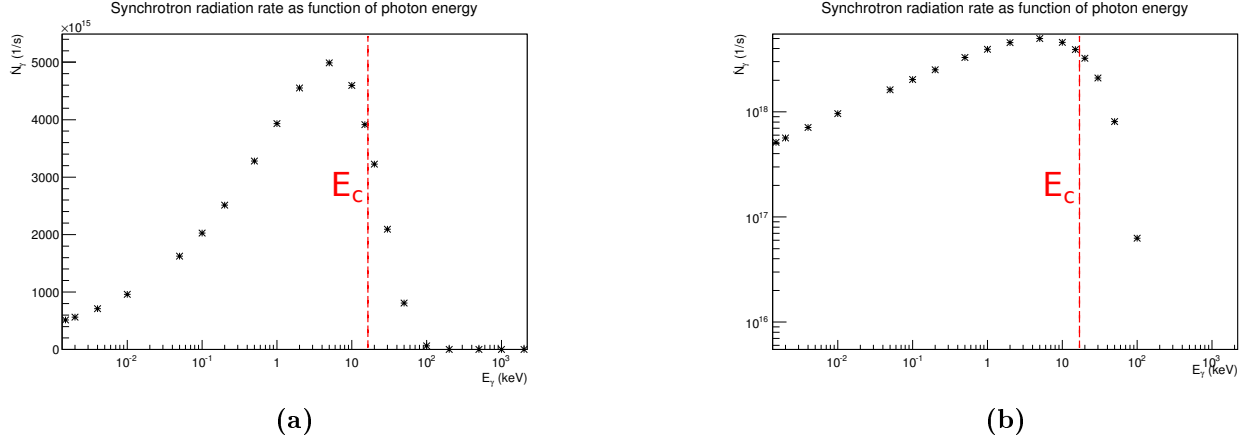
Figure 2.10.: *Synchrotron radiation spectrum of the DESY-II synchrotron accelerator. Here, the electron beam bunch is bent along the accelerator ring with a radius of 27.12 m at an energy of 6.0 GeV. The critical energy E_c is 17.7 keV. [12] (a) logarithmic x-axis (b) logarithmic y and x-axis*

compared to leptons as well as giant resonances. Giant resonances are interactions between photons and heavy atomic nuclei which can result in the emission of neutrons. This is especially relevant, as synchrotron radiation is emitted from the DESY-II synchrotron and additionally many photons are created during the test beam generation.

2.3.1. Stopping power

Section 2.1.2 already introduced the "Bethe formula" in Equation 2.2 for heavy particles. It describes the energy loss per length of a particle passing through matter, which is caused by excitation or ionisation of the electrons of the atomic shells in the material.

In Figure 2.11 the energy loss of a lepton and a hadron is shown, in this case a muon and a proton. For the same particle momentum and material the particle passes through, the energy loss of protons is higher than the loss of muons by about a factor of 10. That means that a proton is stopped after 1/10 of the length after which a muon has lost 1/e of its kinetic energy.

2.3.2. Giant resonances

The giant dipole resonance (GDR) was found in 1947 by G. C. Baldwin and G. S. Klaiber as an excitation of heavy atomic nuclei in photonuclear reactions [13]. Giant dipole resonances are caused by irradiation with photons at energies in the MeV-range. GDR can also be caused by electrons with an energy higher than 50 MeV by coupling to the nucleus via a virtual photon. The excitation energy is dependent on the atomic mass number A of the nucleus and can be expressed by the following formula [14]:

$$E_{GDR} = 31.2A^{-1/3} + 20.6A^{-1/6}(MeV) \tag{2.22}$$

The photons couple to the nuclei and transfer their energy. As a consequence, the dipole moment of those nuclei is increased in such a way that the charges in the nuclei are separated. Therefore, the giant dipole resonance is understood as a collective motion of the protons against the neutrons of the
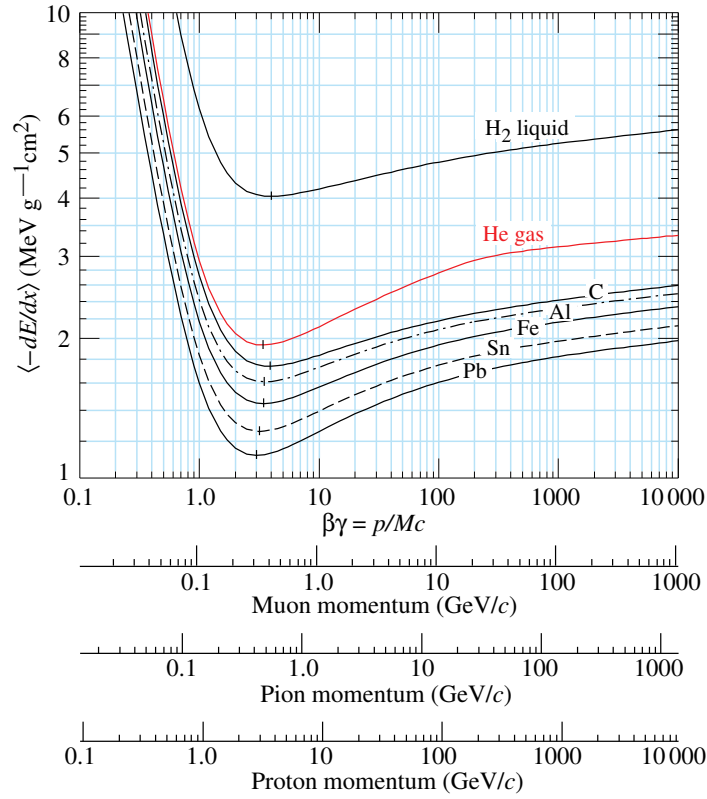
Figure 2.11.: *Plot of the energy loss $\langle -\frac{dE}{dx} \rangle$ derived from the "Bethe formula" for muons, pions and protons. On the x-axis the momentum is shown in GeV/c in different scales for the single particles. The energy loss is also shown in different matter, which shows a small dependency on the properties of the absorber material. The higher the atomic number of the absorber, the lower is the energy loss per length. The reason for this is the density effect correction term $\delta(\beta\gamma)$, which was explained in Section 2.1.2. $\beta\gamma$ is decreasing, when Z increases.[5, page 400]*

nucleus. These motions can be interpreted as vibrations or oscillations around the stable solution. There are several models of a macroscopic description of the highly collective nuclear excitations, e.g. the Goldhaber and Teller model, which considers the vibration as an oscillation of a non-deformed neutron sphere against a proton sphere [15]. The result of the excitations can be emission of neutrons or gamma rays, or even nuclear fission.

2.4. Particle deflection in a homogeneous magnetic field

The dipole magnet is an important part of the test beam generation, as it is necessary for the selection of the beam momentum. The electron/positron pairs enter the dipole magnet and are deflected by its magnetic field. In general, charged particles undergo circular motion in a homogeneous magnetic field, if the Lorentz and the centripetal force are in equilibrium. Therefore, by equalising the two forces, the radius of the deflection can be expressed by:

$$q\vec{v} \times \vec{B} = \frac{m\vec{v}^2}{\vec{r}}$$

$$qvB \cdot \vec{e_r} = \frac{mv^2}{r} \cdot \vec{e_r}$$

$$r = \frac{mv}{q \cdot B}$$

$$r = \frac{p}{q \cdot B} \tag{2.23}$$

To express the radius with respect to the particle energy, the following simplification can be made for electrons/positrons with the charge e:

$$r = \frac{p}{e \cdot B}$$

$$r = \frac{E}{ce \cdot B}$$

$$r[m] \approx \frac{E[10^9 eV]}{0.3[10^9 \frac{m}{s}] \cdot e \cdot B[\frac{Vs}{m^2}]}$$

$$r[m] \approx \frac{E[GeV]}{0.3 \cdot B[T]} \tag{2.24}$$

In the test beam magnet, the particles do not perform an entire circle but are deflected from the original particle path and leave the magnet under an angle to the original particle path. The deflection angle can easily be derived from the simulated data, as can be seen in Chapter 5.5. Therefore, it is useful to calculate the deflection angle theoretically with the following considerations: An electron moving along the z-axis through this magnetic field is deflected on the xz-plane as to be seen in Figure 2.12.

The deflection angle of the electron is derived as follows:

$$cos(\theta) = \frac{d}{l} \qquad\qquad sin(\theta) = \frac{l/2}{r}$$

$$\Rightarrow 2r \cdot sin(\theta) = \frac{d}{cos(\theta)}$$

$$sin(\theta) \cdot cos(\theta) = \frac{d}{2r}$$

$$\frac{1}{2}sin(2\theta) = \frac{d}{2r}$$

$$\theta = \frac{1}{2}arcsin\left(\frac{d}{r}\right) \tag{2.25}$$

As the radius of the particle deflection can be calculated as shown in Equation 2.24, the formula with which the deflection angle can be received from, is:

$$\theta[Radian] = \frac{1}{2}arcsin\left(\frac{d[\text{m}] \cdot 0.3B[\text{T}]}{E[\text{GeV}]}\right) \tag{2.26}$$
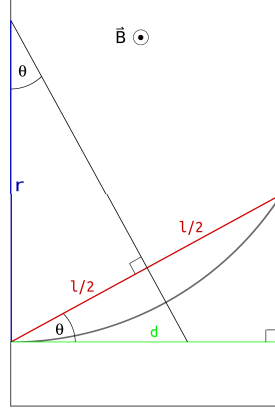
Figure 2.12.: *Scheme of the deflection of a particle with negative electrical charge in a homogeneous magnetic field. The particle is coming in from the right hand side and is bent on a circular path due to the Lorentz force.*

Table 5.19 shows the calculated deflection angle of electrons/positrons for a magnetic field of thickness d = 1 m and certain field strengths.

	B [T]		
E [GeV]	0.2	0.5	5.0
1	1.720°	4.313°	N/A
2	0.860°	2.151°	24.295°
3	0.573°	1.433°	15.000°
4	0.430°	1.075°	11.012°
5	0.344°	0.860°	8.729°
6	0.286°	0.716°	7.239°
6.3	0.273°	0.682°	6.887°

Table 2.2.: *Table of deflection angles in degree calculated for certain magnetic field strengths and particle energies with Equation 2.26. The distance d is defined as 1.0 m for this example. For an energy of E = 1.0 GeV and a magnetic field strength of B = 5.0 T, the equation does not attain a result, as the arcsin(x) is not defined for x > 1. The equation brakes down for particles that are bent in such a way that θ > 90°, e.g. particles that move in spiral paths as a extreme case.*

The dependency between the deflection angle and the magnetic field strength or the particle energy can also be shown from simulated data in a small test geometry. Figure 2.13 contains plots of the deflection angles of electrons with different energies or in homogeneous magnetic fields with different field strengths. The test geometry for this simulation contains only a homogeneous magnetic field of 1 m length. It is designed to be indefinite in the x- and y-direction. The plotted deflection angle was calculated as the angle between the incoming and the outgoing direction of the simulated charged particles. The theoretically calculated values for the deflection angle (listed in Table 5.19) are marked in each of the plots and can directly be compared. The deviation of the experimental value from the theoretical value is about 1.5 - 2.5 %, which is caused by the approximation of the theoretical derivation.
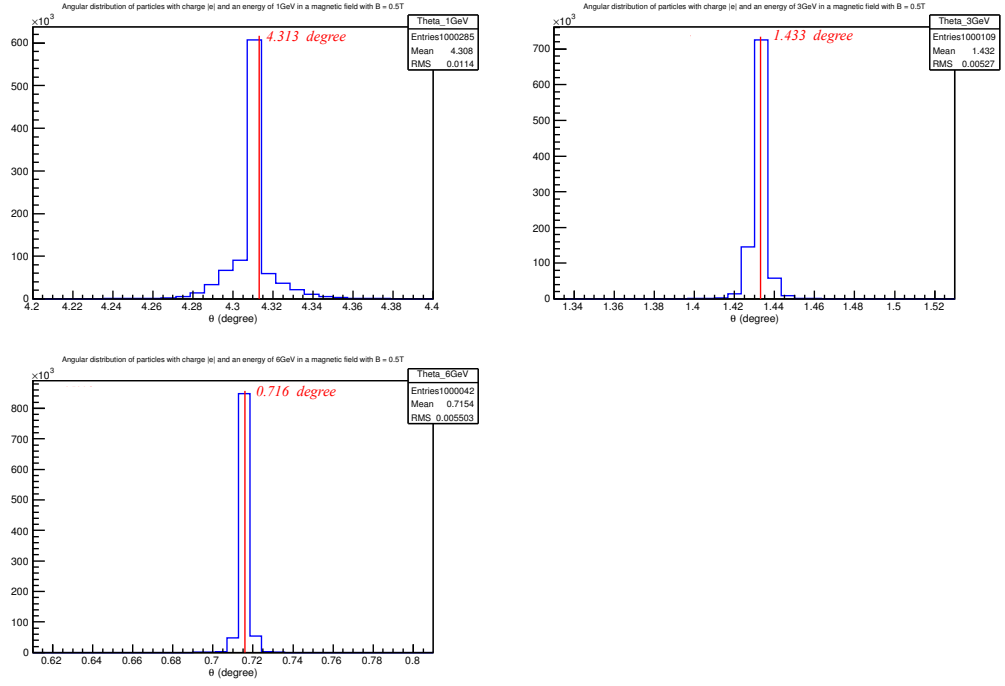
(a) *E = 1 GeV / 3 GeV / 6 GeV, B = 0.5 T*
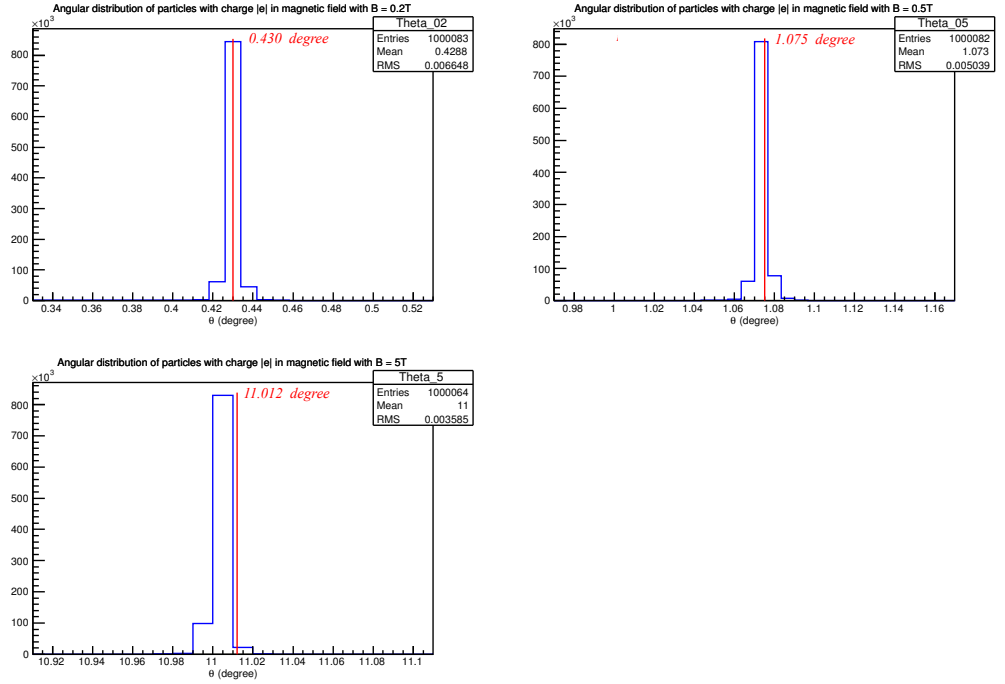
(b) *E = 4 GeV, B = 0.2 T / 0.5 T / 5 T*

Figure 2.13.: *The plots show the deflection angle θ of simulated electrons (a) of different energies in a homogeneous magnetic field with B = 0.5 T. (b) with an energy of 4 GeV in a homogeneous magnetic field of different magnetic field strengths.*
θ is smaller for higher particle energies and greater for stronger magnetic fields. The theoretically calculated deflection angle (see Table 5.19) are highlighted in red colour.

3 Chapter 3.
The DESY-II Test Beam

This chapter gives the principle of the test beam generation and the theoretical background to the simulation of the test beam line components. Therefore, the calculation of the DESY-II beam bunch size will be discussed as well, since the DESY-II bunch is the first step of simulating the DESY-II test beam lines.

3.1. DESY-II synchrotron beam

The DESY-II accelerator is an electron/positron synchrotron ring and has a radius of about 46.6 m. It can accelerate the electron/positron bunch up to about 6.3 GeV.
DESY-II was put into operation in 1987, one year later the proton synchrotron DESY-III, which was based on the old electron synchrotron DESY-I. DESY-I was the first accelerator and the foundation for the research centre DESY. Both DESY-II and DESY-III served as pre-accelerators for HERA (Hadron-Elektron-Ring-Anlage), till HERA was shut down in 2007. DESY-II also fed the storage rings DORIS (Doppel-Ring-Speicher) and PETRA (Positron-Elektron-Tandem-Ring-Anlage) with electrons and positrons.
The main task of DESY-II is nowadays the pre-acceleration for PETRA-III, DESY's synchrotron photon source with the highest brilliance in the world. Additionally, the three test beam lines are fed by DESY-II.

The electrons/positrons from DESY-II are first created and accelerated up to 450 MeV by the LINAC-II, a linear accelerator. The electron source is an electron gun consisting of a heated cathode and an anode. By heating the cathode, an electron stream is created due to thermionic emission. Together with the anode, an electric field is created, which accelerates the electrons away from the cathode, additional focussing electrodes collimate and focus the electron stream. If positrons are needed, the electron beam is directed onto a conversion target, which has an efficiency of creating positrons of 1 %. Before the positron beam is injected into DESY-II, it is accumulated in PIA (Positronen-Intensitäts-Akkumulator), a small storage ring with a circumference of 24 m.[16]

The DESY-II synchrotron ring has eight accelerating cavities, and a lattice of optical elements with static magnetic fields to bend the beam along the accelerator ring and focus it at the same time.
The acceleration of charged particles in the forward direction can only be achieved in an electric field, in contrast bending the particles without acceleration requires a magnetic field. This becomes clear by describing the Lorentz force in Equation 3.1:

$$\vec{F} = q(\vec{E} + \frac{\vec{v}}{c} \times \vec{B}) \tag{3.1}$$

The electromagnetic force is effective in the direction of the electric field and perpendicularly to the plane spanned by magnetic field and direction of movement.

With an homogeneous electric field in the direction of movement, one can accelerate the particle arbitrarily depending on the strength of the electric field. With a homogeneous magnetic field perpendicular to the direction of movement, the particles can be bent in a desired direction. The deflection is dependent on the particle momentum and the magnetic field strength as already shown in Chapter 2.4. This homogeneous magnetic field is provided by dipole magnets, which are designed in such a way that they focus the beam slightly. The effect is called weak focusing.

A better way of focusing is the strong focusing. The simplest and most common strong focusing structure is called "FODO", which is a lattice of focusing and defocusing quadrupole magnets. In between these quadrupole magnets, from which "FODO" got its name ("F" for focussing, "D" for defocussing), there are dipole magnets placed.[17, page 115 ff.] As a quadrupole in general focuses in one plane (e.g. the horizontal plane) and defocuses in the perpendicular plane (e.g. the vertical plane), a structure of alternating focusing and defocusing quadrupoles focuses a beam in both planes simultaneously.

Additionally, one can find sextupole and octopole magnets in a synchrotron accelerator lattice, which are also focusing magnets for adjusting the resonant oscillations, so-called betatron oscillations, of the beam motion. The DESY-II beam bunch consists of 10^{10} electrons/positrons, which vary in momentum and therefore in their trajectories. This variation in energy is commonly given as $\frac{\sigma_E}{E}$ with the width σ_E of the Gaussian energy distribution of the accelerator beam. Its value in listed in Table 3.1.

Electrons with more or less momentum than the ideal value see a different phase of the electric field, so that lower energy particles are accelerated more than the particles with ideal momentum and higher energy particles are less accelerated. The change in the betatron oscillation frequency due to the deviation of the particle relative momentum is described by the chromaticity. A large chromaticity value results from variations in the quadrupole strength according to different particle momentum, and can by reduced the sextupoles and ocopole magnets as mentioned before. Therefore the sextupoles and ocopoles stabilise the betatron oscillations about the ideal path. The overall beam size can be calculated as the statistical deviation from the ideal beam particle position due to betatron oscillations and momentum spread and is shown in Equation 3.2. [17, page 110]

$$\sigma_{tot} = \sqrt{\sigma_\beta^2 + \left(\eta \frac{\sigma_p}{p}\right)^2} \tag{3.2}$$

The deviation due to betatron oscillations is described as $\sigma_\beta^2 = \epsilon_x \cdot \beta_x$, whereas the deviation due to the momentum spread has to be weighted by the dispersion function η. The betatron function $\beta(s)$ is defined as $\beta(s) = \sqrt{\omega(s)}$, where $\omega(s)$ is the amplitude function of the particles motion along the orbit s in a periodic strong focusing lattice, such as "FODO". Hence, $\beta(s)$ describes the envelope of all particle trajectories.[17, cf. page 100 ff.] In the phase space, there is a region of acceptance, in which the particles motion is stable. This region is approximated as an ellipse, which will always contain the same fraction of beam on successive cycles around the synchrotron ring. The theorem of a conserved area of the ellipse is called Liouville's theorem. The area is defined as $\pi\epsilon$, with ϵ being the emittance.[17, cf. page 106] The dispersion function describes the change in the particle trajectory due to the deviation

from the nominal particle momentum p_0. Therefore, the dispersion function is defined as

$$\eta(s) = \frac{\Delta u}{\Delta p / p_0} \tag{3.3}$$

where Δu is the deviation from the particle position on the nominal trajectory around the synchrotron ring.[17, cf. page 108 ff.]

With Equation 3.2, the horizontal and vertical beam bunch size can be calculated. Since there is no dispersion in the vertical plane, the beam size in y is simply dependent on the position spread due to the betatron oscillations.

$$\sigma_x = \sqrt{\epsilon_x \cdot \beta_x + (\eta \cdot \sigma_E / E)^2} \tag{3.4}$$

$$\sigma_y = \sqrt{\epsilon_y \cdot \beta_y} \tag{3.5}$$

As the beam parameters vary along the circumference of the DESY-II ring, the beam sizes are different at the certain positions, where the test beam lines originate from the synchrotron ring. The primary targets are positioned behind the DESY-II quadrupoles with the numbers 21, 22 and 24, after which the test beam lines were named.

Table 3.1 contains the beam parameters and the attained beam sizes for the three test beam lines 21, 22 and 24.[18]

TB line	β_x [m]	β_y [m]	η [m]	ϵ_x[nm·rad]	ϵ_y[nm·rad]	σ_E/E	σ_x [mm]	σ_y [mm]
21	4.943	16.193	0.819	345.96	35	$9.798 \cdot 10^{-4}$	**1.534**	**0.753**
22	13.870	6.039	1.319	345.96	35	$9.798 \cdot 10^{-4}$	**2.543**	**0.460**
24	11.350	7.249	1.500	345.96	35	$9.798 \cdot 10^{-4}$	**2.467**	**0.504**

Table 3.1.: *Table of the DESY-II beam parameters and sizes at the positions of the primary targets for test beam lines 21, 22 and 24. The horizontal and vertical beam sizes, σ_x and σ_y, are calculated with the given Equations 3.4 and 3.5.*

3.2. The test beam generation

The test beam generation can be split up into four steps: bremsstrahlung, photon conversion, energy selection and collimation. The test beam line components, responsible for the four steps, are illustrated in Figure 3.1.

As the primary target, a 25 μm thick bundle of carbon fibres is positioned in the electron/positron beam of the DESY-II synchrotron. The DESY-II beam has a Gaussian distributed beam energy around 6.3 GeV. The photons, that are emitted from the carbon fibre due to bremsstrahlung, show a $\frac{1}{E}$ dependency in their energy spectrum with a maximum energy of approximately 6.3 GeV. In Section 2.1.3, the theoretically derived formula for the bremsstrahlung spectrum is given. Because of that dependency, the intensity of photons with higher energies up to 6.3 GeV is much smaller than the intensity of low energy photons.

After travelling through about 18 m of air in the DESY tunnel, the bremsstrahlung photons that hit the converter, which is the secondary target, can convert into electron/positron pairs if their energies
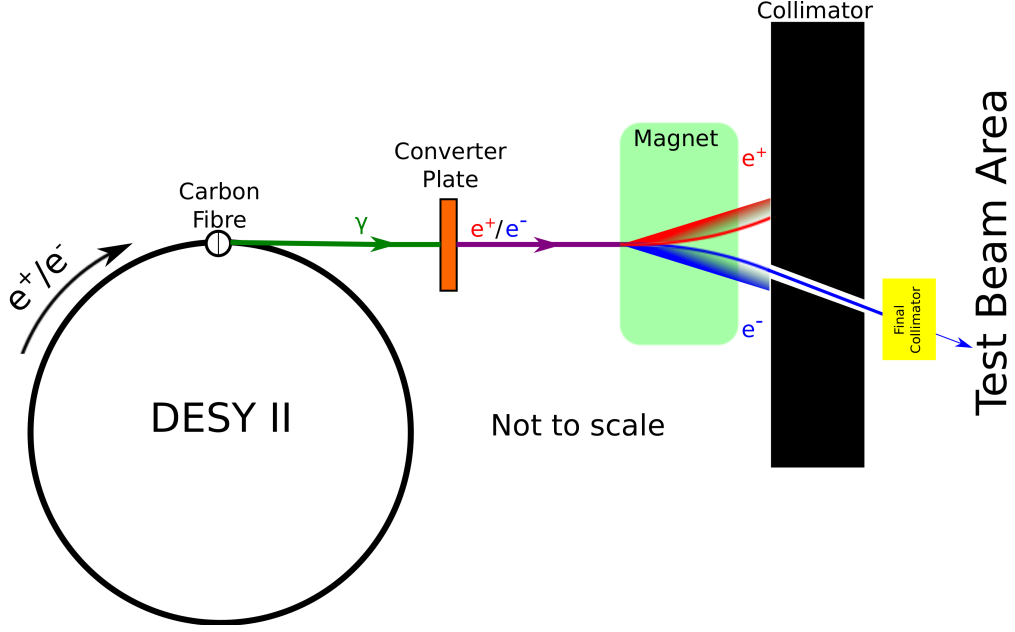
Figure 3.1.: *A scheme of the generation of the DESY test beams.[19]*

are $\geq 2 \cdot m_e$, where m_e is the rest mass of an electron. The converter can be selected from several aluminium or copper plates of variable thickness. The material as well as the thickness of the converter plate influence the final beam rate and can be chosen by the test beam user. A list of the available targets for each test beam line is obtainable on the DESY test beam web page [20] and also in Appendix A.1.2. Figure 3.2 shows the beam rates of the DESY test beam line 21 for different converter plate materials. [21]

With the high energy approximation of the total cross section for electron/positron pair production in Equation 2.11, the cross section in copper and aluminium can easily be calculated:

$$\sigma_{Cu} = \frac{7}{9} \frac{A_{Cu}}{X_{0,Cu} N_A} \tag{3.6}$$

$$= \frac{7}{9} \frac{63.546 \, \text{g mol}^{-1}}{12.86 \, \text{g cm}^{-2} \cdot 6.022 \cdot 10^{23} \, \text{mol}^{-1}} \tag{3.7}$$

$$= 6.38 \cdot 10^{-28} \, \text{m}^2 = 6.38 \, \text{barn} \tag{3.8}$$

$$\sigma_{Al} = \frac{7}{9} \frac{26.982 \, \text{g mol}^{-1}}{24.01 \, \text{g cm}^{-2} \cdot 6.022 \cdot 10^{23} \, \text{mol}^{-1}} \tag{3.9}$$

$$= 1.45 \cdot 10^{-28} \, \text{m}^2 = 1.45 \, \text{barn} \tag{3.10}$$

The cross section in copper is approximately four times the cross section in aluminium. The values for the atomic mass and radiation length can be found in particle list of the Review of Particle Physics of the Particle Data Group [5, page 116].

The test beam magnet and the collimator allow varying the final test beam energy accordingly to the choice of the user. As the deflection of charged particles in a homogeneous magnetic field is dependent on the sign of the particle charge q, the particle momentum p and the magnetic field strength B, the
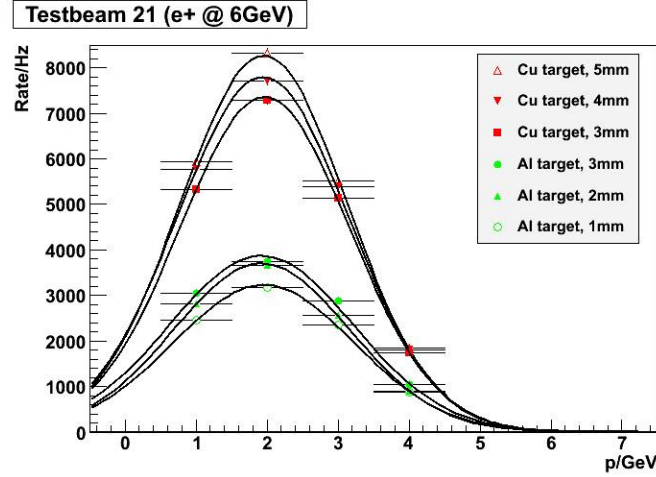
Figure 3.2.: *The measured rate of the positron beam for test beam line 21 is plotted as a function of the particle momentum. The rate is highly dependent on the material and thickness of the secondary target. In general, the thicker the material, the higher the conversion rate. Additionally, copper yields higher rates than aluminium, since the cross section for pair production is greater for copper than for aluminium.*

dipole magnet widens the electron/positron beam into a fan in the xz-plane. Section 2.4 derives the deflection radius and angle for a charged particle in a magnetic field.
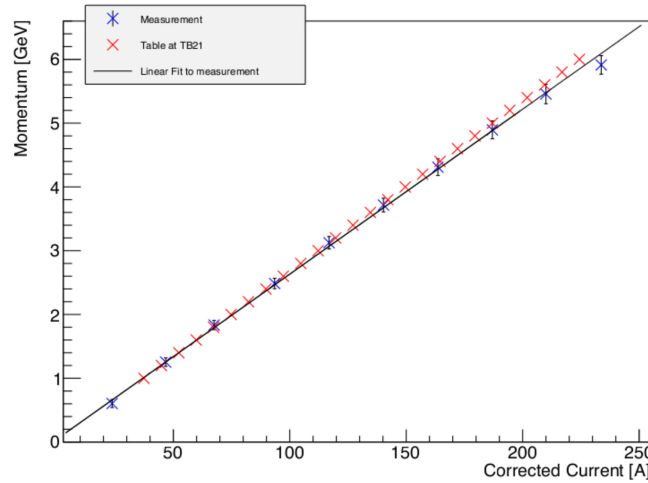
Figure 3.3.: *Plot of the particle momentum as a function of the current through the MR dipole magnet of the test beam line 21. [22]*

Electrons and positrons are deflected in opposite direction due to their opposite charge. The higher the momentum is, the bigger is the deflection radius, so that the particles are less deflected. In contrast to that, the stronger the magnetic field is, the smaller the radius.

The collimator positioned behind the magnet lets only a part of the beam pass. As the magnetic field strength can be adjusted by varying the current through the magnet, the radius of the particle

deflection varies according to $r = \frac{p}{e \cdot B}$. Therefore only the part of the beam with the desired beam energy passes the collimator and enters the test beam area. The energy of the final electron/positron beam has an energy up to 6.3 GeV, depending on the user's choice.

A table of the current through the dipole magnet (MR) and the corresponding beam energy is provided in the control huts of the single test beam areas and is also given in the table given in Appendix A.1.3. Figure 3.4 displays additionally the relationship between the current and the resulting magnetic field strength. The table was updated by a DESY summer student in 2013 in the course of his project [22], as the particle momentum of the test beam was measured in dependency of the current. This results shown in Figure 3.3 are compared and improved by this simulation.
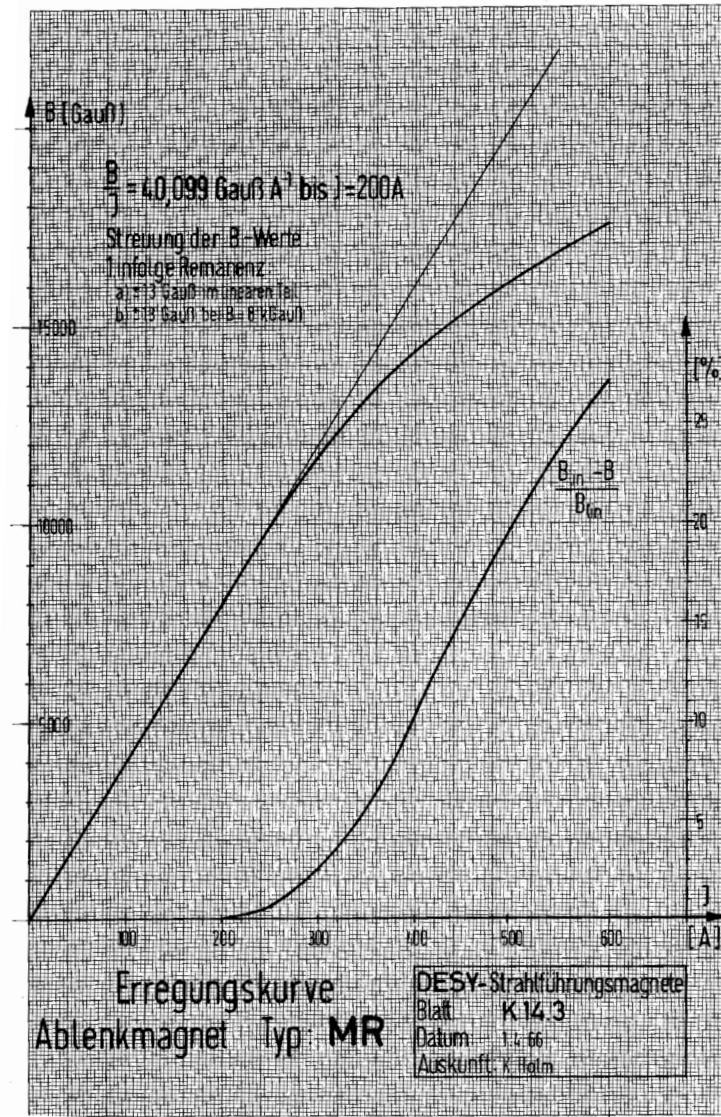
Figure 3.4.: *Plot of the magnetic field strength as a function of the current through the MR dipole magnet of the test beam lines. In the region of interest (up to about 0.9 T) the relationship between magnetic field strength and current is linear. [23]*

4 Chapter 4.

Description of the software used for the Geant4 Monte Carlo simulation and its functionality

For the Monte Carlo simulation of the physics processes and the analysis of the simulated data, the simulation package SLIC and several software packages of the software collection ILCSOFT are used. In the following, a short description of those packages will be given, as well as a description of the functionality of the Monte Carlo simulation itself. In Monte Carlo generators and simulators, particles are labelled with the PDG Monte Carlo numbering scheme, which is also briefly explained.

4.1. Software

4.1.1. SLIC

The "Simulator for the Linear Collider" SLIC [24] uses the GEANT4[1] toolkit for Monte Carlo simulation of particles passing through detector material. SLIC is used for concept studies of the "Silicon Detector" SiD, one of the two detectors of the future "International Linear Collider" ILC [25].

There are several options of event generators for a simulation with SLIC. The four supported types are StdHep, LCIO, GEANT4 General Particle Source and GEANT4 Particle Gun.

Both of the GEANT4 event generators are used for the simulation of the DESY test beam. Next to the particle type and number of events, the direction and energy of the initial particles can be set. In contrast to the GEANT4 Particle Gun, also spectral, spatial and angular distributions of the particle sources can be specified with the GEANT4 General Particle Source (GPS)[2]. It is possible to write all settings and specifications about the event generation into a macro that can be executed by SLIC. Figure 5.1 shows the energy and spatial distribution of a simulated particle beam, generated with a SLIC macro using GPS.

---

[1] GEANT4 is one of the "Geometry and Tracking" toolkits developed at CERN, the "European Organization for Nuclear Research", for the simulation of the particle passage through matter. It uses object oriented programming (C++) and is freely available on the internet. Its application areas cover high energy and accelerator physics as well as space science amongst others.

[2] The GPS manual contains lists of possible commands to specify an event source and explanations as well as an example macro file. The official General Particle Source manual was incorporated into the Application Developers Guide (see [26]).

For the simulations with SLIC, several different GEANT4 physics lists are available, which include the properties and decay modes of particles, parameters of pre-defined physics processes, e.g. Compton scattering, and their cross sections. The default GEANT4 physics list SLIC uses is *LCPhys*. *LCPhys* contains several classes for gamma, lepton, hadron and ion physics as well as particle decays. [27]

The geometry of the beam line components is defined in a GDML file. The "Geometry Description Markup Language" (GDML) is based on the human-readable XML language, and is used for describing detector geometries with arbitrary placements of objects. The GDML file is then included into a self created XML compact file, which additionally contains information about the world volume, tracking volume and other self defined logical volumes, as well as about sensitive detector planes and magnetic fields. The sensitive detectors collect data of the particles passing through, like the particle type, its charge, its momentum and the position. The XML compact detector description allows to simply define a detector as volumes made of material with placements.

As GEANT4 requires this information in triplicate, i.e. a solid, a physical volume and a logical volume, the XML file has to be converted into a format called "Linear Collider Detector Description" LCDD. The conversion to the LCDD format expands the basic information of the detector components into the verbose requirements of GEANT4 with the GEANT4 information hierarchy. For converting, the *detector-framework* software package from `org.lcsim`[3] is used.

SLIC's simulated events are created in the LCIO format, which stands for "Linear Collider Input/Output". It is a persistency framework and event data model for detector studies. As this framework is used by ILCSOFT, which also includes the LCIO software package, a description of LCIO follows in more detail in the next section 4.1.2.

The GDML geometry description format allows to construct every arbitrary geometry. A description of a solid box with a round shaped hole is shown below as an example GDML geometry. Complex composite shapes can be formed by using e.g. the operations `union` and `subtraction`. For unifying two solids or subtracting one solid from another, the second solid is placed with given position (and rotation) in the coordinate system of the first solid. In the given example, two tubes were combined and then subtracted from a solid box at pre-defined positions. The box has hence a hole in its centre in the form of the two tubes.

Materials of the solids and the world itself can be defined, as well as arbitrary placements of the objects in the world. A full GDML file is given in Appendix A.2.2.1.

GDML geometries can be visualised with different tools available. The example geometry is visualised using a VRML viewer, called SAP 3D Visual Enterprise Viewer [28]. The visualisation is shown in Figures 4.1 (a) and (b).

---

[3] The "Linear Collider Simulation" framework is based on Java and includes many features for event reconstruction and data analysis.

```
  <gdml>
...
   <solids>
     <box lunit="mm" name="Box"
         x="400." y="400." z="200."/>
     <tube name="Hole1"
         rmin="0." rmax="50." z="200." lunit="mm"
         deltaphi="360" startphi="0" aunit="deg"/>
     <tube name="Hole2"
         rmin="0." rmax="30." z="200." lunit="mm"
         deltaphi="360" startphi="0" aunit="deg" />
     <union name="Both_holes">
       <first ref="Hole1"/>
       <second ref="Hole2"/>
       <positionref ref="Union_position" />
     </union>
     <subtraction name="Box_with_holes">
       <first ref="Box"/>
       <second ref="Both_holes"/>
       <positionref ref="center" />
     </subtraction>
     <!- world volume ->
     <box lunit="mm" name="WorldBox"
         x="500." y="500." z="world_side" />
   </solids>
...
  </gdml>
```
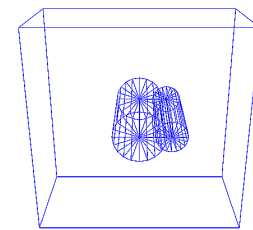

(a)
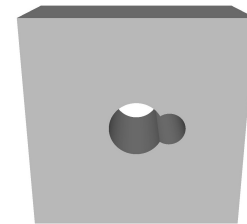
(b)

Figure 4.1.: *Example geometry of a solid box with a hole visualised with* VRML. *Figure (a) shows the grid of the solid. The two single tubes that are subtracted from the box are now visible. The solid surface of the shape is shown in Figure (b).*

4.1.2. ILCSoft

The ILCSOFT package was developed for the ILC for simulating the particle detectors. It contains a software package for GEANT4 simulation, event data models, a geometry package for reconstruction, a 3D event display and a `C++` application framework for reconstruction and data analysis. For more information about the single software packages and ILCSOFT in general see [29].

With the "Modular Analysis & Reconstruction for the Linear Collider" framework MARLIN, data analysis processors can be written and controlled with XML steering files, in which the order of used MARLIN processors and global parameters can be set. The steering files represent a full configuration of the MARLIN application.

As MARLIN also uses the LCIO model, the data simulated with SLIC can therefore be processed with MARLIN in a convenient way. Self defined data structures can also be created with the LCIO class *LCGenericObject*. As mentioned in the section before, self defined detector geometries can be used for the SLIC simulation. The LCIO class *LCGenericObject* is used to express the resulting data structures. Detailed documentations of the LCIO members and class references can be found at [30].

4.2. Functionality of the Geant4 Monte Carlo simulation

The input to every Geant4 Monte Carlo simulation with SLIC is the geometry of the world, with which the generated particles will interact. It is described in GDML and XML format and then converted to the LCDD format, as explained before in Section 4.1.1. The adjustment of the particle generation is done in a macro for SLIC, which also sets the address of the geometry file and the random engine. The random engine is seeded with the current time in milliseconds since 1 January 1970.

As mentioned before, there are two types of particle generators: the Geant4 Particle Gun and Geant4 General Particle Source, which in principle generate particles of set type, number, and energy. Also the position and direction of the initial particles can be defined, however only the Geant4 General Particle Source can generate a spread particle source with an adjustable energy distribution.

The generated particles move through the geometry following the laws of physics, that are set by the Geant4 physics list, like the *LCPhys* list (see Section 4.1.1). The Geant4 Monte Carlo method applies all the relevant physical models, which are explained in Chapter 2, and uses the radiation lengths of the materials in the geometry to predict whether the particle will decay or how much it will scatter off the matter it is passing through. For example, a particle hitting a block of lead with a certain momentum and direction, SLIC will go through the physics list of possible processes, and calculate the probability of a change in the particle's parameters for each process by using random fluctuations from the random engine. With the "Highland formula" (see Equation 2.12), e.g., it will calculate how the particle will scatter. An important parameter for SLIC is the step length, which is the distance at which the particle's parameters are updated. By setting the limit of the maximum step length in the geometry XML file to a small number, the simulation can be more accurate and realistic, but also more time-consuming at the same time. A compromise is to set the maximum step length down only in certain logical volumes of the geometry, like the volume where the magnetic field is effective.

In this way, SLIC is accurately reproducing the real world.

Leptons	
e^-	11
e^+	-11
μ^-	13
μ^+	-13

Gauge bosons	
γ	22

Baryons	
n	2112
p	2212

Mesons	
π^0	111
π^+	211
π^-	-211

Table 4.1.: *Table of example particles with their PDG Monte Carlo particle numbers. The antiparticle has the negative number of the particle.*

4.3. PDG Monte Carlo particle numbering scheme

The PDG Monte Carlo particle numbering scheme is a numbering system for all listed PDG particles of the standard model as well as for SUSY particles. The numbering scheme is used for different Monte Carlo event generators and detector simulators, so that the particle identification scheme is generalised and the translation between event generators and detector simulators is simplified. Quarks and leptons are numbered consecutively starting from 1 and 11 respectively. There are special rules of numbering diquarks, mesons, baryons and SUSY particles. In general, only particles are given. The particle code for the antiparticle is the particle's number with a negative sign. The particles relevant for this master's thesis are listed in Table 4.1.

The latest version PDG Monte Carlo particle numbering scheme is available on the Particle Data Group web page.[31]

5

Chapter 5.

The simulation of the test beam generation

This chapter is following the order of the test beam generation and describes the single test beam line parts successively, starting with the simulation of the DESY-II bunch and ending with the final collimated electron/positron beam. In the end, flux maps of the test beam lines out of simulated data are shown.

5.1. The DESY-II electron bunch

DESY-II is a synchrotron accelerator with a single bunch of 10^{10} electrons. The beam bunch hits the carbon fibre, the primary target of the test beam lines, and produces bremsstrahlung. The bremsstrahlung photons are converted to electron/positron pairs, which proceed to the test beam hall after selecting the desired beam energy. To be able to compare the particle fluxes of the simulation with the real particle fluxes, it is important to have a realistic simulation of the DESY-II beam bunch as an input for further simulations.

The SLIC macro used for simulating the DESY-II bunch uses the GEANT4 General Particle Source (GPS) as the event source. GPS offers the source type "Beam" along with others and allows the setting of the horizontal and vertical beam sizes. The type of energy distribution was adjusted to be Gaussian with a certain value of σ_E/E. The exact values for beam sizes and energy distribution are listed in table 3.1. The SLIC macro itself can be found in Appendix A.2.1.

After simulating 10^{10} electrons in the DESY-II bunch, one can plot the energy distribution as well as the spacial distribution of the beam bunch as shown in Figure 5.1. The Gaussian fit yields $\sigma_E = 0.0062\,\mathrm{GeV}$ which is approximately the energy width one can calculate with $\sigma_E/E \cdot 6.3\,\mathrm{GeV} = 9.798 \cdot 10^{-4} \cdot 6.3\,\mathrm{GeV} = 6.173\,\mathrm{MeV}$.

5.2. The primary target

The first part of the DESY test beam lines is the primary target, the carbon fibre bundle. The carbon fibres have a thickness of $25\,\mu\mathrm{m}$ and are positioned in the beam pipe of the DESY-II storage ring. Figure 5.2 shows the carbon fibre holder, which holds the actual primary target as well as replacements. If one target is broken, it is replaced by a new one by simply rotating the holder to the next position. [32]

As already explained, the DESY-II bunch hits the carbon fibre bundle and emits bremsstrahlung photons tangentially to their beam path, i.e. tangentially to the synchrotron ring. The direction of the emitted bremsstrahlung photons is henceforth defined to be the z-axis in a right handed coordinate

(a) *Energy distribution of the DESY-II beam bunch. A bunch contains 10^{10} electrons with a mean energy of $6.301\,GeV$. The Gaussian distribution has a sigma value of $\sigma_E = 0.0062\,GeV = 6.2\,MeV$.*

(b) *Spacial distribution of the electrons in the DESY-II beam bunch at ring position of test beam generation for test beam line 21. The horizontal and vertical beam sizes are calculated as $\sigma_y = 1.534\,mm$ and $\sigma_y = 0.753\,mm$.*

Figure 5.1.: *The energy and spacial distribution of the simulated 10^{10} electrons in the DESY-II beam bunch. The values for σ_E/E and the beam sizes σ_x and σ_y are listed in table 3.1.*
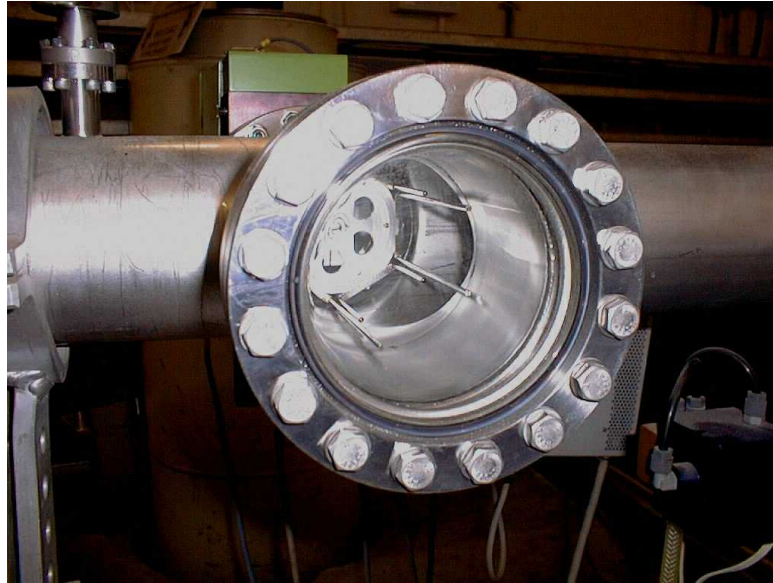
Figure 5.2.: *Picture of one of the carbon fibre holders in the DESY-II beam pipe. The holders are designed to hold several primary targets at different positions. The beam pipe has a window to see the fibres at their positions. Additionally, the holder is horizontally movable. In case of beam parameter testing and adjusting, the fibres can be moved perpendicularly through the beam.*

system, as is shown in Figure 5.3. On the first meters after emission, the photons pass through a beam pipe and an aluminium beam pipe window before entering the DESY-II tunnel.
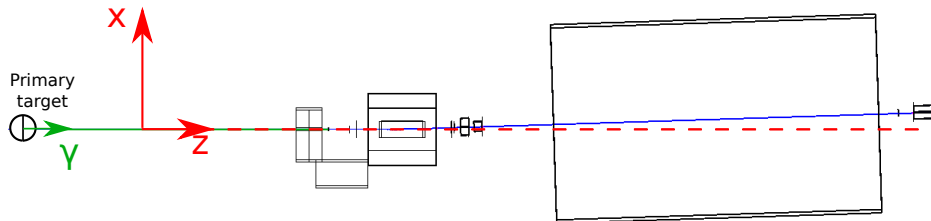
Figure 5.3.: *The scheme shows the definition of the coordinate system used for the test beam line simulation. The coordinate system is defined to be right handed in such a way that the z-axis is along the direction of the bremsstrahlung photons emitted from the primary target. In this figure, the y-direction is pointing out of the plane.*

In the event description for SLIC, the 10^{10} electrons in the DESY-II beam bunch are simulated with the same beam parameters as explained before in Section 5.1. The simulation's geometry description of the world contains the carbon fibre, which is hit by the beam bunch.

The simulation is split into 1000 parts, so that each simulation file contains 10^7 electrons hitting the primary target. By filling the number of photons from each file into a histogram, this attains in average 213 ± 14.24 bremsstrahlung photons per 10^7 electrons (see Figure 5.4 (a)). The combination of all files obtains an energy spectrum of all bremsstrahlung photons as shown in Figure 5.4 (b). A fit was applied to the spectrum with the Equation 2.9 from Chapter 2.1.3. The fit describes the data well, therefore the simulation yields a realistic spectrum of bremsstrahlung photons emitted by the electrons hitting the carbon fibre.

The spectrum of the photons serves as the input for subsequent simulation steps, which were already theoretically explained in Chapter 3.2. To do so, the photons have to be subtracted from the initial electrons of the DESY-II beam. In reality the electrons don't leave the DESY-II synchrotron but are bend along the storage ring. The simulation doesn't take this into account, as the whole DESY-II synchrotron would have to be simulated, but allows the electrons to continue along with the bremsstrahlung photons. A `C++` code was written to create a spacial map containing the number of the bremsstrahlung photons and their energy. Hence, the information about number and energy of the particles is combined with the information about their position. Such a map is shown in Figure 5.5. To be noted is that the TH2F histogram has only 7×7 bins for clarity, in contrast to that the map, which is used for further steps, contains 21×2 1 bins with smaller bin sizes in the centre.

A script in the programming language *PERL*[1] was written to automatically create SLIC macros for the next simulation steps with the particle source information attained from the map mentioned before.

---

[1] *PERL*, "Practical Extraction and Reporting Language" is a family of general-purpose, interpreted programming languages and includes *PERL 5* and *PERL 6*. The languages are designed for text processing and combine features for instance from shell scripting and other programming languages like C.

(a)

(b)
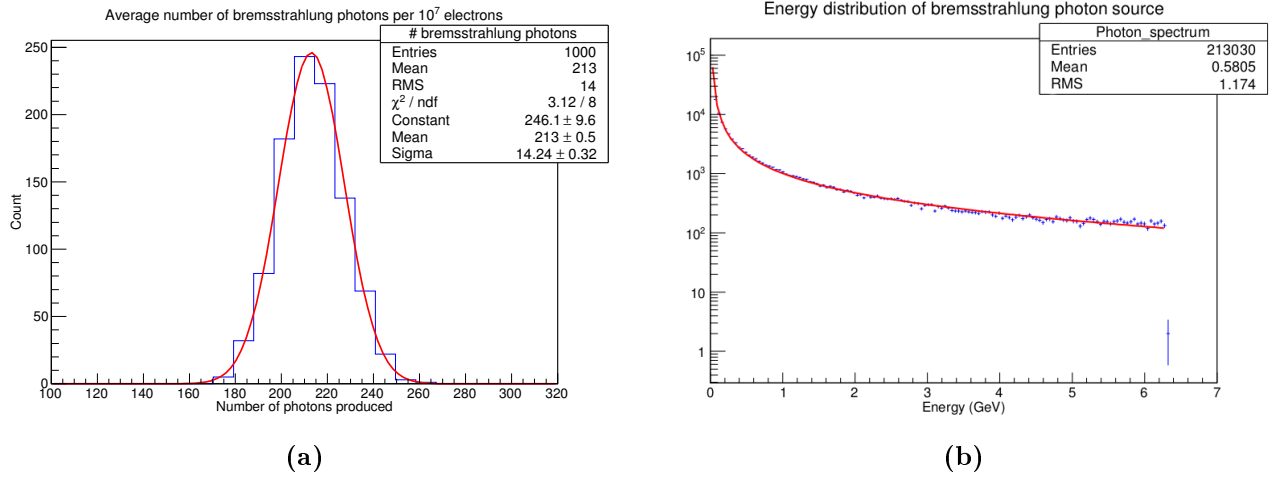
Figure 5.4.: *Due to hitting the carbon fibre, the beam bunch of 10^{10} electrons generates in total about $2 \cdot 10^5$ bremsstrahlung photons. Figure (a) shows the Gaussian distribution of the number of bremsstrahlung photons per 10^7 electrons. The bremsstrahlung spectrum of all photons combined is shown if Figure (b). It ends at about $6.3\,GeV$, because the maximum energy of the photons cannot exceed the maximum energy of the respective electrons. Mostly low energy photons in the MeV range are produced.*
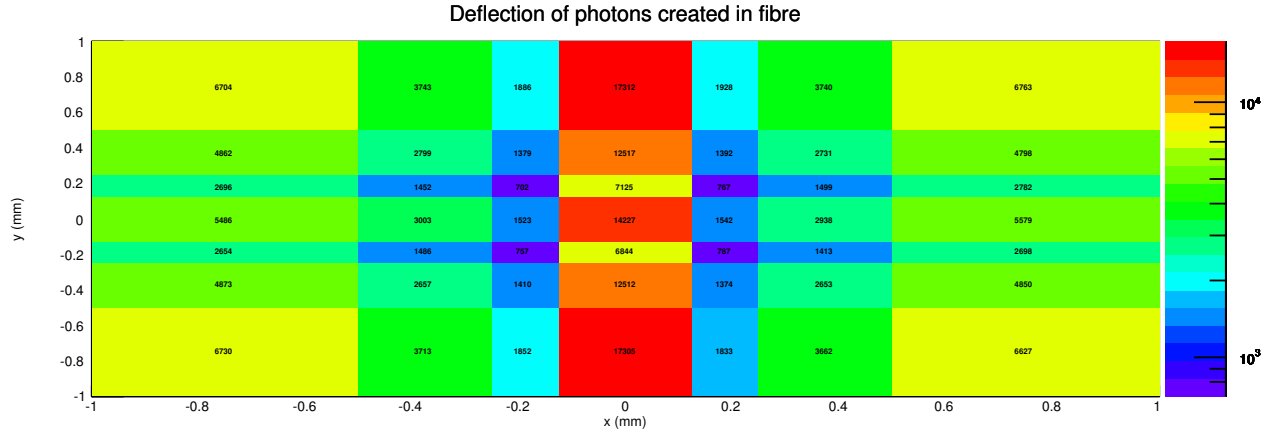
Figure 5.5.: *Large meshed spacial map of the bremsstrahlung photons emitted by the electron beam hitting the primary target. The single numbers in the bins stand for the number of photons located between x_1 and x_2 and y_1 and y_2, the bin's limits. To be noted is that the bin sizes are getting smaller towards the centre in order to have a higher spatial resolution. Due to that smaller bins show a lower number of photons and are coloured with cold colours, but nevertheless the majority of photons is in the very centre of the plot.*

5.3. The lead shielding

The bremsstrahlung photons emitted from the primary target do not simply travel through an evacuated beam pipe until they hit the secondary target, which is described in detail in Section 5.4. They leave the pipe through an aluminium beam pipe window and travel about 18.5 m in air before they reach the secondary target. Along the way, secondary particles are produced due to interactions with the beam pipe material, the beam pipe window, pair-production in the air, and also hadronic interactions with matter. Giant dipole resonances (GDR) (see Chapter 2.3.2) cause neutron fluxes in the test beam line, where only electromagnetic interactions are expected. The occurrence of neutrons was discovered in the simulation of the test beam generation along with the other secondary particles, which are listed in Table 5.1. The table lists all simulated particles occurring in the simulation of the bremsstrahlung photons passing through the beam pipe with beam pipe window and the air in the simulated world. Their energy distributions are plotted in Figure 5.6.

Nevertheless, not only the secondary particles accompany the bremsstrahlung photons, but also synchrotron radiation from the DESY-II synchrotron ring.
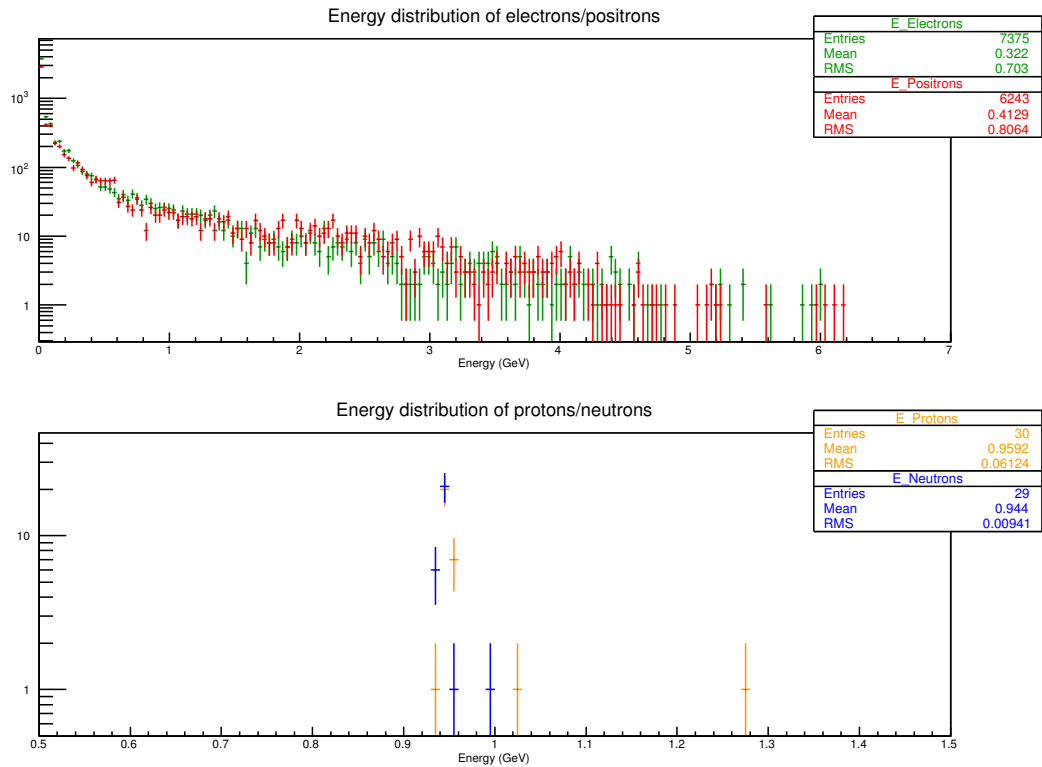
Figure 5.6.: *These plots show the energy distributions of the secondary electrons/positrons and protons/neutrons listed in Table 5.1. They occur in the simulation as secondary particles of the bremsstrahlung photons before the secondary target. The energy distribution of the protons and neutrons starts at about 0.9 GeV, as this is their rest mass taken into account in the plotted energy.*

The secondary particles, the synchrotron radiation, and bremsstrahlung photons deviating from the ideal test beam path, cause problems in different ways. Firstly, the flux destroyed scintillators that

were set up near to the beam line. The scintillators were not designed for such high particle fluxes. Secondly, they either reach the secondary target and interact with its material or directly enter the test beam magnet. Both cases lead to particles continuing on the test beam path and entering the test beam area, even though that is undesirable. The noticeable and measurable effect of this is broader momentum distributions of the final test beam because of this background rate. The much greater effect is a measurable particle rate in the test beam area in case of a switched off test beam magnet, which should reduce the test beam rate to zero in an ideal environment. To avoid all this, a shielding is

Particle	PDG code	#	%
all		228,256	100.00
γ	22	214,577	94.01
e^-	11	7,375	3.23
e^+	-11	6,243	2.74
n	2112	29	$1.27{\cdot}10^{-2}$
p	2212	30	$1.31{\cdot}10^{-2}$
π^0	111	2	$8.76{\cdot}10^{-4}$

Table 5.1.: *Table of particles occurring in the simulation of the test beam generation before the secondary target.*

necessary, that is designed in such a way that the undesired particles are stopped, and only the desired beam particles are allowed to continue on the test beam line. A shielding was suggested to be built up in front of the secondary target, but with a hole for the particles on the ideal test beam path.

As an additional achievement of this Master's thesis project, the decision making on the material and thickness of the shielding was supported by simulation studies of the stopping ability of certain materials. Hence, photons were simulated hitting shielding walls of different materials and thickness. For this test simulation, 450,000 photons with an energy of 5 GeV were generated to pass through a beam pipe and the DESY-II tunnel and to hit the shielding wall. Therefore, the circumstances of the actual test beam bremsstrahlung photons and the secondary particles were used. As the first material, a lead wall was chosen, since lead prevents undesired electrons/positrons and photons from hitting the secondary target. For stopping neutrons and protons, both concrete and acrylic glass were suggested and compared in simulation. The chemical name for acrylic glass is Poly(methyl methacrylate) or PMMA. It is a transparent thermoplastic and often known under the trademark name Plexiglas™.

Figure 5.7 shows the ability of stopping photons, electrons/positrons, protons and neutrons in a shielding wall of different materials. The first 20 cm thick layer is lead. For the second layer, the plot shows the number of stopped particles in concrete of 20 cm thickness and PMMA of 5 cm thickness. The shielding effect of concrete and PMMA can now be easily compared. Additionally, the momentum distributions of the particles in heavy concrete and PMMA of each the same thicknesses as before are compared (see Figure 5.8).

As a result, the acrylic glass plane and the concrete wall show the same ability to stop neutrons and protons. Also the difference in the stopping ability between 20 cm and 40 cm thick concrete walls is negligible. Since heavy concrete bricks and blocks were already available in the DESY test beam facility, it was decided to built the shielding up from a lead brick wall and heavy concrete brick wall, each 20 cm thick and with a beam path hole. Figures 5.9 and 5.10 show schemes and pictures of the final test beam shielding for test beam line 21.
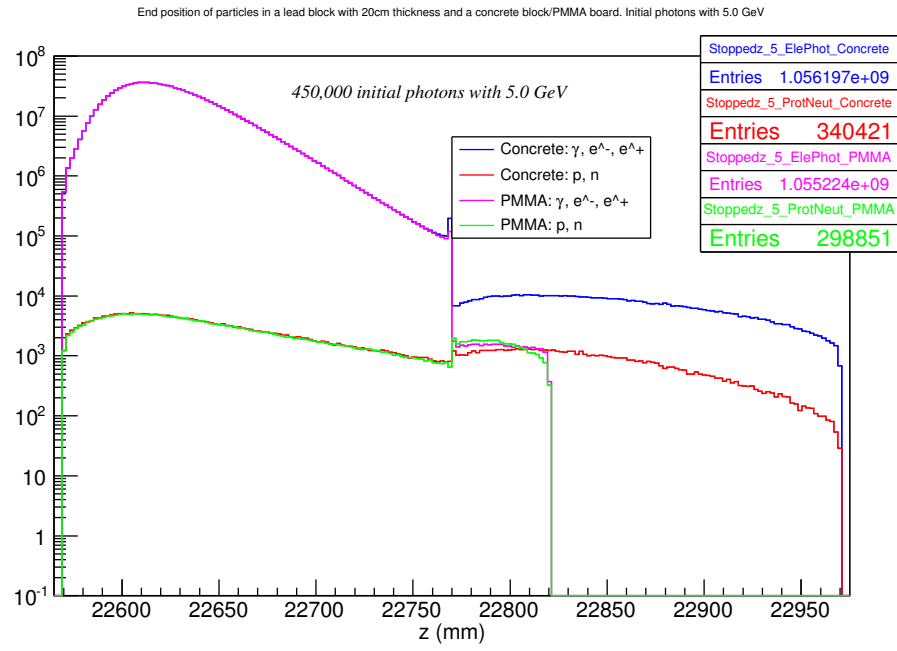
Figure 5.7.: *Simulation of electrons, photons, neutrons and protons in a lead/concrete or lead/PMMA shielding. The plot shows the number of stopped particles along the z-axis in the material. The lead and concrete layers have each a thickness of 20 cm. The acrylic glass or "PMMA" plane is only 5 cm thick.*
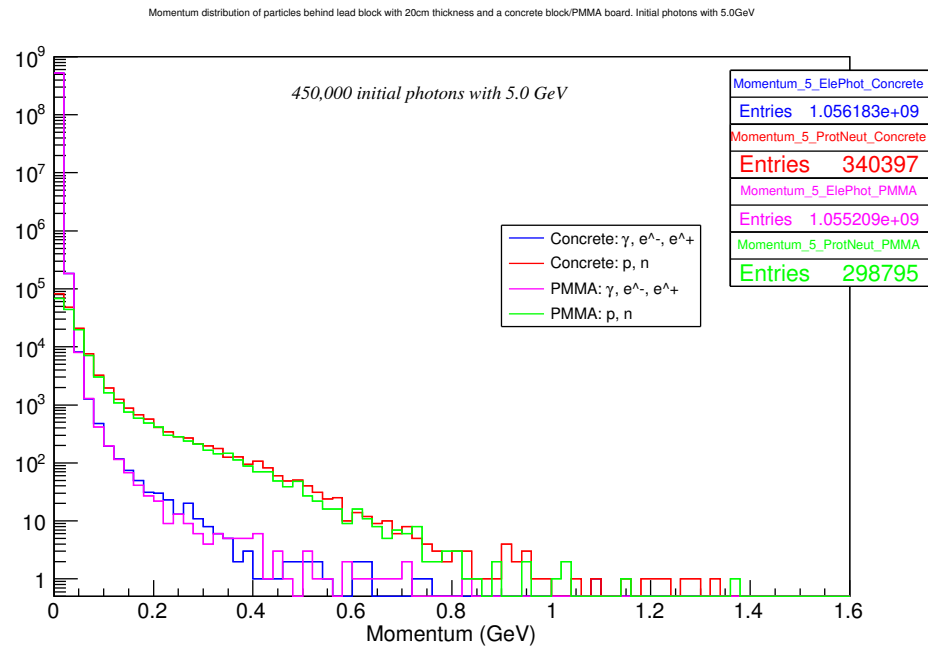
Figure 5.8.: *Simulation of electrons, photons, neutrons and protons in a heavy concrete wall with 20 cm thickness or a PMMA plane of 5 cm thickness.*

(a)   (b)
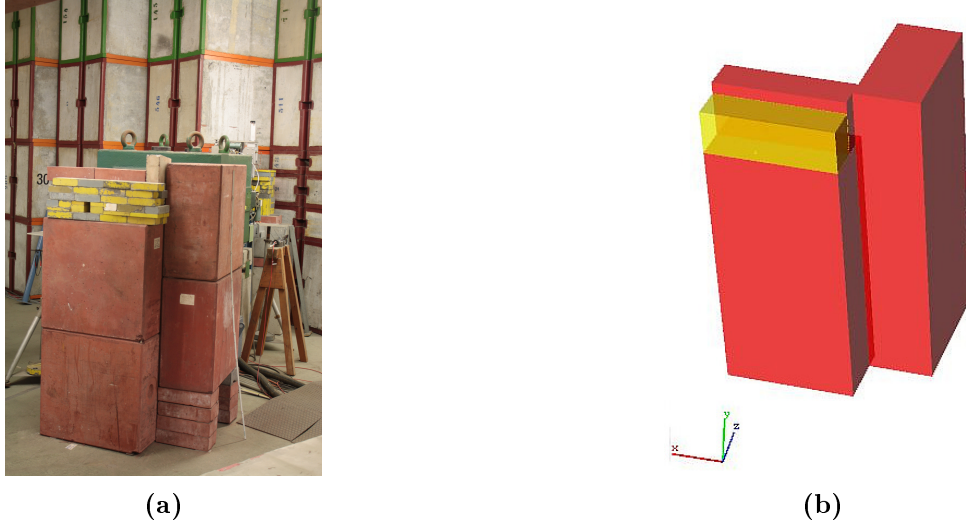
Figure 5.9.: *Figure (a) is a picture of the lead and concrete shielding built up in front of the dipole bending magnet in the test beam line 21. Figure (b) shows the three dimensional model of its simulation visualised with a* VRML *viewer.*

(a)   (b)
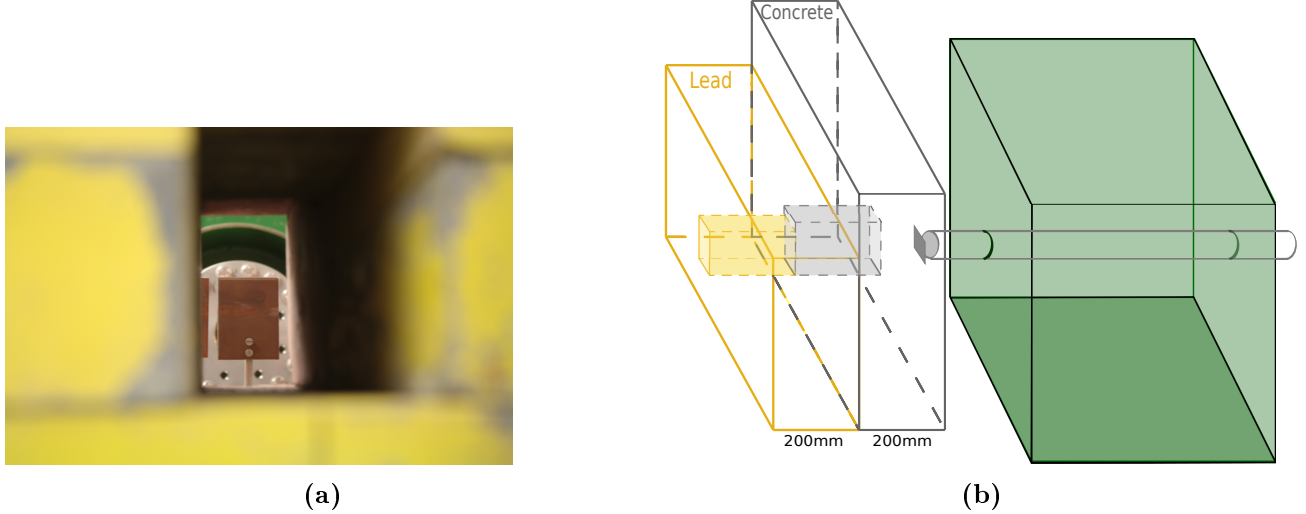
Figure 5.10.: *Figure (a) shows a picture of the secondary target through the beam path hole in the lead and concrete in front of the test beam dipole magnet. The three dimensional scheme in Figure (b) illustrates the relative positions and sizes of the beam path holes in the lead and concrete shielding.*

5.4. The secondary target

The secondary target serves as a converter of the bremsstrahlung photons to electron/positron pairs. In Chapter 3.2 it was already mentioned that the rate of the final test beam depends on the material and thickness of the secondary target. The reason for this is the dependency of the cross section for pair production on the atomic mass and radiation length of the material. Because of that, the test beam users are offered a selection of different converter plates to chose from appropriately to their needs. The test beam lines have slightly different secondary targets, but in general there are copper plates with a thickness of 5 mm, 4 mm and 3 mm, aluminium plates with a thickness of 3 mm, 2 mm and 1 mm and copper wires with a diameter of 1 mm. The most commonly used converter target is the a copper target with 5 mm thickness as it yields the highest particle rate. In Figure 5.11 and Figure 5.15 the different secondary targets are shown for test beam 21 and 24.
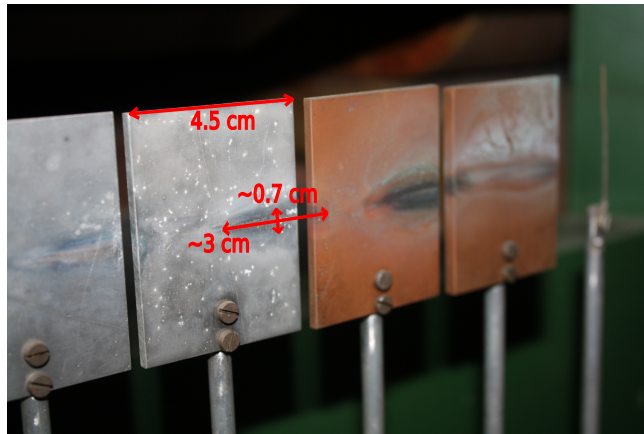
Figure 5.11.: *Picture of the different converter plates of test beam line 24. The copper and aluminium plates have a size of 4.5 cm × 6 cm and various thicknesses. Also copper wires are available as the secondary target. The dark ovals on the converter plates originate from the bremsstrahlung photons hitting the plates. The size of the bremsstrahlung photon beam is directly observable.*

The numbers of electrons and positrons attained by the conversion in the different converters of test beam line 21 are compared in Figure 5.13. As expected also from Figure 3.2 in Chapter 3.2, the copper targets yield higher electron rates than the aluminium targets. The dependency on the material thickness also becomes clear: the thicker the material, the more photons are converted into electron/positron pairs. The copper wire with a diameter of 1 mm yields the least electron/positron pairs. Table 5.2 additionally lists calculated conversion efficiencies of the simulated converter targets. The difference in the distributions between Figure 5.13 and 3.2 is due to the point of measuring the number of electrons/positrons. The simulation shows the electron rate directly behind the secondary targets. On the contrary, the particle beam was collimated twice before the rate was measured in the test beam area in order to create the plot in Figure 3.2. Therefore, the particles, that deviate from the ideal beam path, are removed by the collimation.
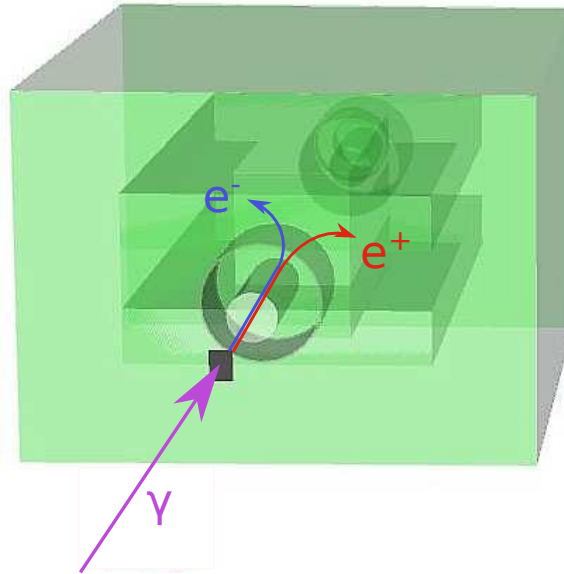
Figure 5.12.: *The simulation of a converter plate in front of the dipole magnet of the test beam line is visualised with a* VRML *viewer and shown here together with a scheme of a photon conversion to an e^+/e^- pair. The electrons and positrons are entering the dipole bending magnet and are bent in opposite direction in the xz-plane.*

5.5. The test beam magnet

The actual test beam magnet is a dipole magnet, for which the technical drawings are available on the DESY test beam web page.[23] One of the drawings of the magnet is shown in Figure 5.14. The magnet casing and the pole in the middle of the copper coil are made out of iron. The magnetic dipole field strength increases linearly with the current through the magnet as shown in Figure 3.4. After the photon conversion to electron/positron pairs in the secondary target, the electron/positron pairs enter an evacuated beam pipe and then the test beam magnet. The magnet is positioned about 60 cm behind the converter plate (see Figure 5.15). As discussed before, charged particles are deflected in a homogeneous magnetic field. The deflection radius is dependent on the magnetic field strength and the particle momentum. Also the particle charge affects the deflection: electrons and positrons are deflected in opposite directions because of their opposite charge. The electron/positron beam is spread into a particle fan and separated into electrons and positrons. The low energy particles are strongly deflected, while the high energy particles are hardly deflected. Neutral particles, like the unconverted photons, are not influenced by the magnetic field and continue on their initial path if not scattered or stopped. A model of the simulated dipole magnet is given in Figure 5.16.

About 15 cm behind the test beam magnet, the beam pipe has a kink in such a way that the original and the new beam path draw an angle of 32 mrad. Also the subsequent components of the test beam line are not positioned in the straight line behind the magnet, but along this new beam path. The reason for this is to separate the deflected charged particles from the photons, which leave the magnet undeflected and would pass through the further beam pipe and enter the test beam area. With a kink in the beam pipe and the test beam line in general, only the desired electrons/positrons continue on the test beam line.

Energy distribution of electrons and positrons behind the converter plate
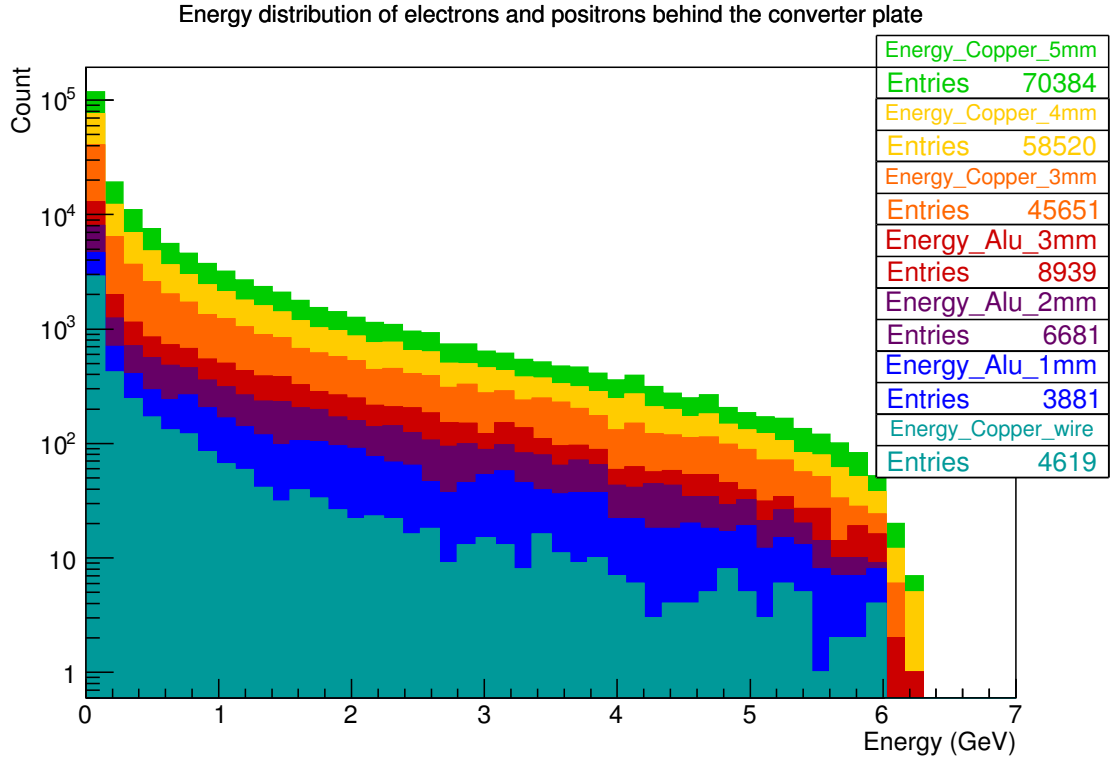
Figure 5.13.: *The plot shows the energy distribution of electrons and positrons behind the secondary target of the test beam line 21. It is a direct comparison between the different secondary targets and their photon conversion efficiencies. The plot is a stacked histogram.*

Converter	#	%
Copper 5 mm	70,384	17.13
Copper 4 mm	58,520	14.24
Copper 3 mm	45651	11.11
Aluminium 3 mm	8939	2.17
Aluminium 2 mm	6681	1.63
Aluminium 1 mm	3881	0.94
Copper wire	4619	1.12

Table 5.2.: *Table of efficiency to convert a photon to a electron/positron pair in different converter materials. To be noted is that the given efficiencies are approximated, as the number of photons hitting the secondary target varies for every simulated run. The number of photons taken for this calculation is 205,500, taken from one simulation of the test beam line 21.*
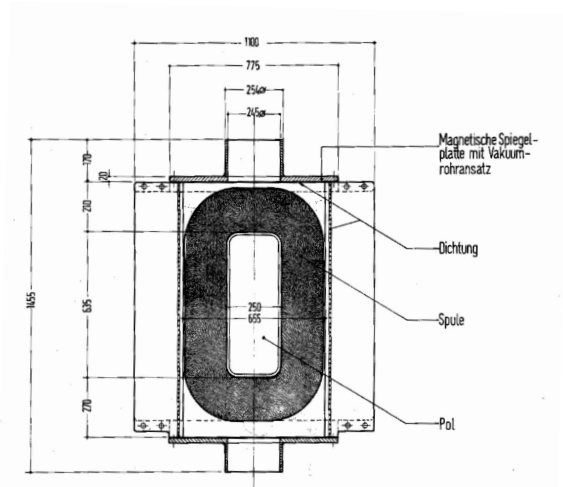
Figure 5.14.: *Technical drawing of the dipole magnet of the test beam lines. The view on the magnet is from above, so that due to the cut through the magnet the iron body, the coil and the iron pole are visible.*

Figure 5.15.: *Picture of the different converter plates of test beam line 21 in front of the bending dipole magnet. The aluminium beam pipe is evacuated and has a Kapton beam window. The green iron pipe around it belongs to the magnet surrounding and does not serve any special purpose.*

Only one part of the fan has the right deflection angle to move along the kinked beam pipe and to enter the test beam area. As the particles are sorted continuously by energy within the fan, the particles of this part of the fan have similar energies. The test beam user can choose the energy of the test beam by changing the current flowing through the magnet. The magnetic field strength varies linearly with the current and therefore the particle deflection radius, such that the appropriate part of the particle fan is deflected into the kink pipe.

Before starting the simulation of the particles passing through the world and the magnetic field, the step size at which SLIC will recalculate the physics processes has to be limited, otherwise the program would step past the magnetic field. Hence, a limit has to be set in the LCDD file by adding the following lines to the volume, where the magnetic field is effective:

```
<limits>
  <limitset name="StepLimitSet">
    <limit name="step_length_max" particles="*" value="1.0" unit="mm"/>
  </limitset>
</limits>
```

For all particles entering the logical volume of the magnet, the step size for SLIC is limited to a maximum of 1.0 mm. The volume is therefore split into many 1.0 mm thick strips, for which one after the

other the processes of all particles in that volume are recalculated with the particles' (varied) parameters.

Figures 5.17 and 5.18 show some histograms of the position of the deflected charged particles in the xy-plane directly behind the dipole magnet. The dots therefore represent the position, where the according particle leaves the magnet.The particle fan is clearly visible as well as the dependency on the particle charge. Oppositely charged particles are deflected in opposite directions, because of which there are two particle fans. Due to the colour axis, it is clear that the particle density across the fans is not uniform. The density in the fans peaks near the centre and smears out towards the sides. The figures do not only show the particle positions for the cases of different polarity of the magnetic field, but also for different values of the magnetic field strength. In comparison of the peaks in the particle fans in both Figures 5.17 (a) and (b), the peaks are further apart in the case of a higher magnetic field strength (here B = 0.75 T). As the radius of deflection is inversely proportional to the magnetic field strength (see Equation 2.24), the radius is smaller and the deflection stronger with a higher magnetic field strength. That means that particles with the same energy are deflected more in Figure 5.17 (b) than in (a). This also results in a lower number of particles leaving the magnet, when the magnetic field strength is higher. The particles are deflected more, and therefore less particles enter the beam pipe to leave the magnet.

The particles within the black circles, which illustrate the contour of the beam pipe, enter the beam pipe behind the magnet. However, only the particles that are bent in the positive x-direction are able to proceed further on the test beam line, since the beam pipe is kinked as mentioned above. Figures 5.18 therefore explain why the magnetic field has to be reversed, if positrons are wanted as the final test beam particles. They only reach the test beam area for negative magnetic field strengths.
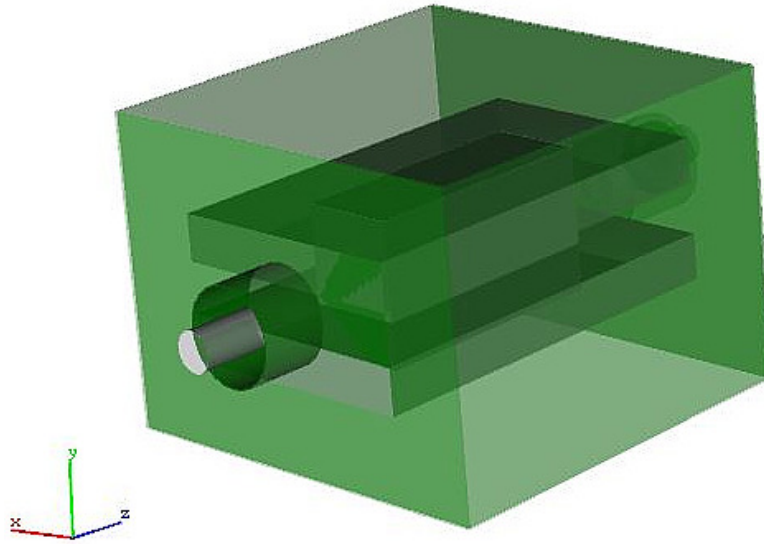
Figure 5.16.: *The simulation of the dipole magnet of the test beam lines is visualised with a* VRML *viewer. The copper coils of the magnet are visible, which are 13 cm apart from each other. Both of the coils have an iron pole, which only leaves a gap between the iron poles of 10 cm. In this free evacuated volume, the simulated magnetic field is effective.*

(a) *B = -0.3 T*

(b) *B = 0.75 T*
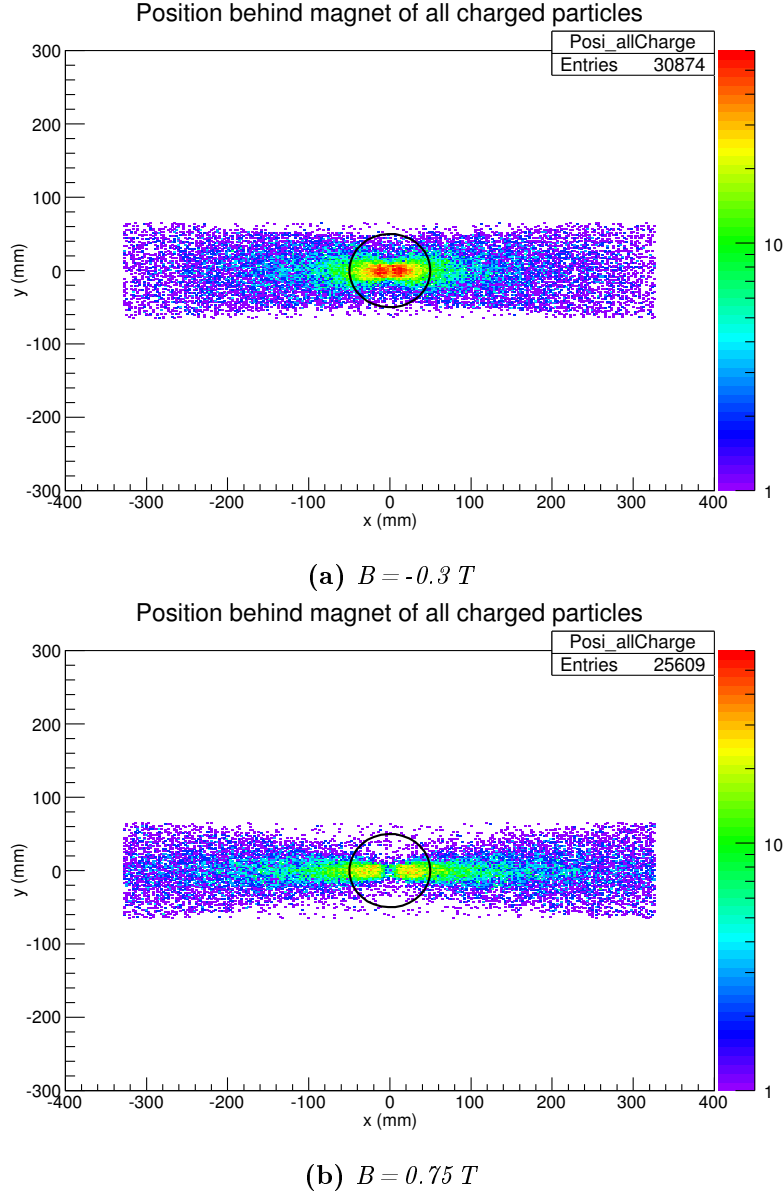
Figure 5.17.: *The plots show the x-/y-position of all charged particles directly behind the test beam magnet. It is therefore a view in the xy-plane on the back of the magnet. The points represent the x/y position, where the particles leave the magnet. The black circle illustrates the beam pipe coming out of the magnet. The distinct area, where most of the particles are, is the area between the magnet coils and the outer iron walls of the magnet surrounding, in other words the area where the magnetic field is effective. The magnet's material around that area absorbs all other particles.*

Figure (a) shows the particle position for a magnetic field strength of B = -0.3 T, Figure (b) for B = 0.75 T, respectively. For a lower magnetic field strength, more particles will leave the magnet than for the higher one. This is due to the fact that the deflection radius is smaller for a higher magnetic field strength, so that the particles are deflected more. The result is that less particles enter the beam pipe but hit the magnet surrounding material.

(a) *Negatively charged particles, B = -0.3 T*   **(b)** *Positively charged particles, B = -0.3 T*

(c) *Negatively charged particles, B = 0.75 T*   **(d)** *Positively charged particles, B = 0.75 T*
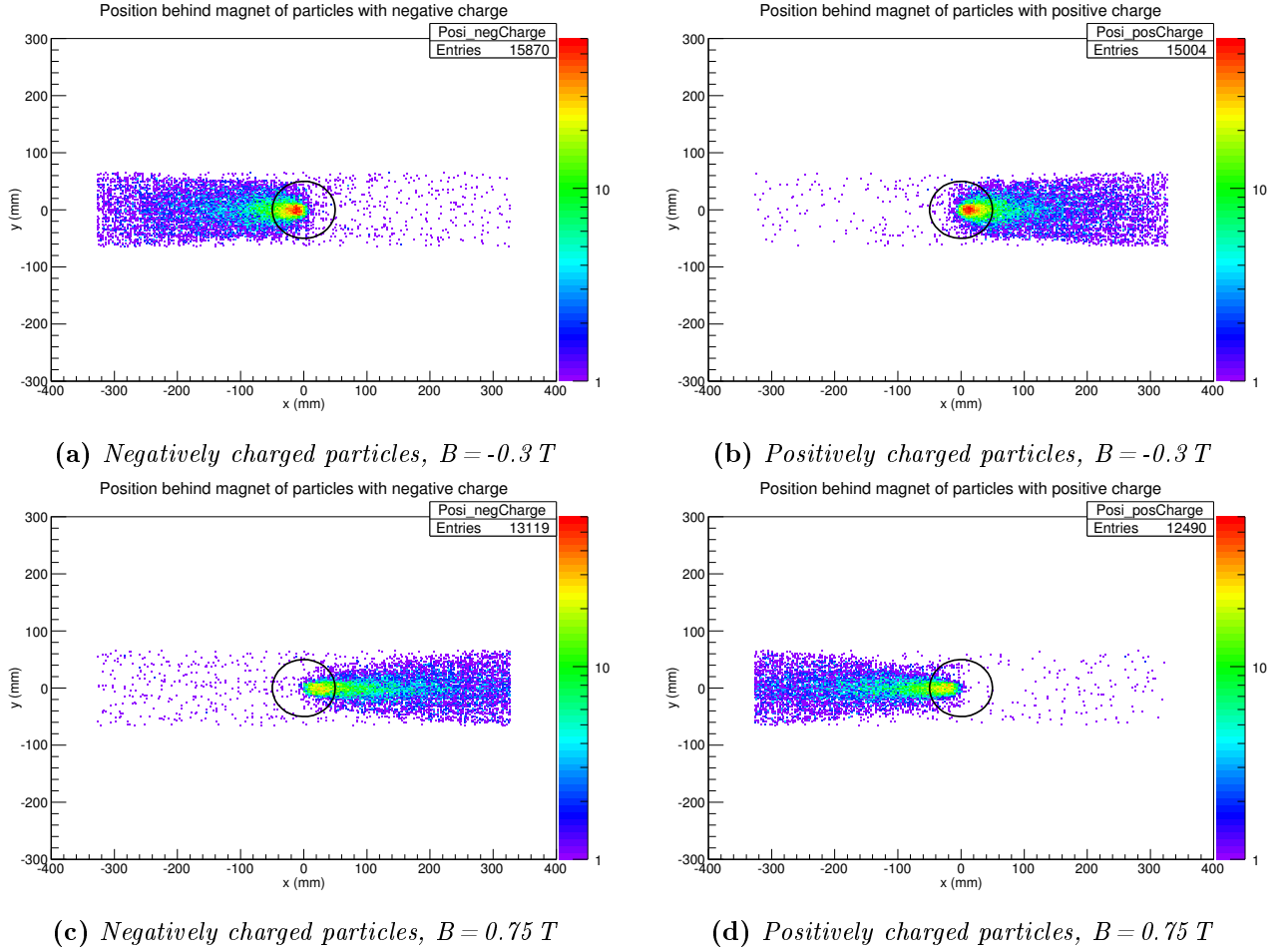
Figure 5.18.: *The plots show the x-/y-position of negatively/positively charged particles directly behind the test beam magnet, therefore the points represent the positions, where the particles leave the magnet. The black circle illustrates the beam pipe coming out of the magnet. Figures (a) and (b) show the particle position for a magnetic field strength of B = -0.3 T, Figures (c) and (d) for B = 0.75 T, respectively. As the polarity of the magnetic field is reversed for Figures (c) and (d), the negatively/positively charged particles are deflected in the opposite direction than in (a) and (b). The particles with 0 mm < x < 400 mm in Figures (a) and (d), and those with -400 mm < x < 0 mm in Figures (b) and (c) are scattered particles. They either entered the magnet with an angle to the z-axis or scattered off the material in the magnet or both.*

With the simulated data, the deflection angle θ can be calculated as the angle between two vectors with Equation 5.1. The first vector $\vec{v}$ is a vector between the position $\vec{s_1} = (x_1, y_1, z_1)$, at which the particle enters the magnetic field, and the position $\vec{s_2} = (x_2, y_2, z_2)$, at which it leaves the magnet again, as can be seen in Figure 5.20. The second vector is the momentum vector at the first position, the start of the magnetic field. Two sensitive tracking planes were put in front and behind the test beam magnet in the geometry for the simulation in order to gain precise information about the particles' position

and momentum. These tracking planes are defined to be less than 1 nm thick, and their material is set to be vacuum to only allow additional readout and not to affect the particles' passage.

$$
\begin{aligned}
cos(\theta) &= \frac{\vec{v} \cdot \vec{p_1}}{|\vec{v}| \cdot |\vec{p_1}|} \\
\theta &= \frac{(\vec{s_2} - \vec{s_1}) \cdot \vec{p_1}}{|\vec{s_2} - \vec{s_1}| \cdot |\vec{p_1}|} \\
\rightarrow \theta[°] &= \frac{360°}{2\pi} \frac{(x_2 - x_1)p_{1,x} + (y_2 - y_1)p_{1,y} + (z_2 - z_1)p_{1,z}}{\sqrt{(x_2 - x_1)^2 + (y_2 - y_1)^2 + (z_2 - z_1)^2}\sqrt{p_{1,x}^2 + p_{1,y}^2 + p_{1,z}^2}}
\end{aligned}
\tag{5.1}
$$

	B [T]
E [GeV]	0.3
1	1.832°
2	0.916°
3	0.610°
4	0.458°
5	0.360°
6	0.305°

Figure 5.19.: *Table of deflection angles in degree calculated for magnetic field strength of B = 0.5 T and certain particle energies with Equation 2.26. The range d, over which the magnetic field expands in z-direction, is defined as 0.710 m for this example.*
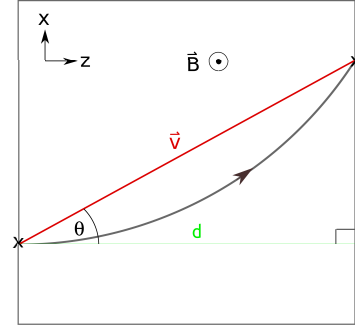
Figure 5.20.: *Scheme of the deflection on a circular path of a negatively charged particle in a homogeneous magnetic field. The crosses identify the points of entering and leaving the magnetic field, which are connected by the vector $\vec{v}$. The angle between $\vec{v}$ and the z-direction can be calculated with Equation 5.1.*

By filling θ calculated as in Equation 5.1 into a profile plot, so that the deflection angle distribution is plotted as a function of the particle energy, the distribution can be fitted with Equation 2.26 derived in Chapter 2.4. The plot is shown in Figure 5.21. The free parameter was chosen to be the length of passage in the magnetic field, which comes to 0.7099 m ± 0.0001 m. In the GDML geometry description of the dipole magnet, the magnetic field was defined to range over 710 mm in the z-direction and to have a field strength of B = 0.3 T. The comparison of the ranges of the magnetic field from the fit and the geometry definition shows that the theoretically derived formula for the deflection angle describes the data well. The χ^2/ndof value is 134.2/130.

Table 5.19 lists some deflection angles theoretically calculated for certain particle energies with Equation 2.26. The values for the magnetic field and the range, over which the magnetic field expands in the z-direction, match the definitions in the GDML geometry description. Since data and theoret-

ical prediction meet, these values can be found in Figure 5.21. Specifically for a particle energy of $3\,\mathrm{GeV} \pm 0.05\,\mathrm{GeV}$, Figure 5.22 shows a Gaussian distribution for the deflection angle θ. Its mean value 0.6101 matches precisely the value in Table 5.19.
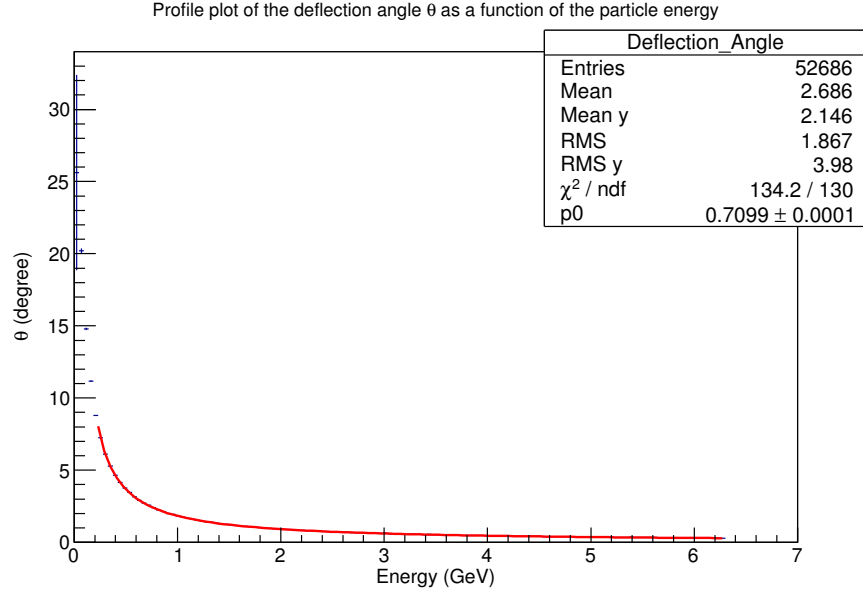
Figure 5.21.: *Profile plot of the deflection angle as a function of the particle energy attained with simulated data. For the applied fit, the derived Equation 5.1 for the deflection angle was used.*
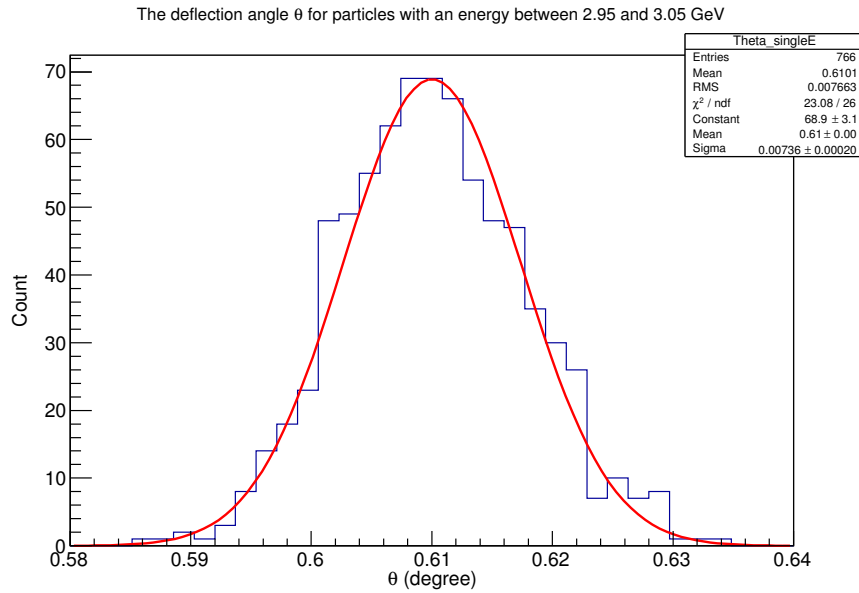
Figure 5.22.: *Plot of the deflection angle for a particle energy of $3\,GeV \pm 0.05\,GeV$. The Gaussian fit yields a mean value of $0.610°$.*
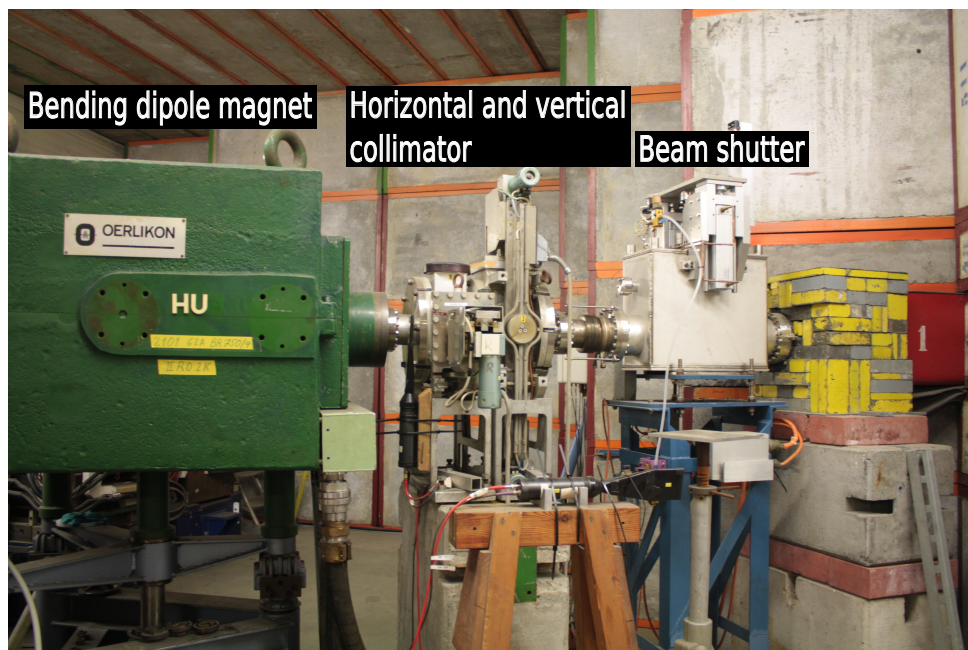
Figure 5.23.: *Picture of the bending magnet, the horizontal and vertical collimators and the beam shutter of test beam line 21. The bent electrons/positrons, that have such a deflection angle that they follow the beam pipe, are collimated first horizontally and then vertically. If the beam shutter is open, they enter the test beam area through the concrete wall on the right hand side of the picture. The beam shutter is made out of a lead block which can be lowered into the beam path whenever the test beam user pushes the button in the control hut that controls the beam shutter. At that point, the user is allowed to be in the test beam area.*

5.6. The test beam collimator

It was already indicated in Section 5.5 before, that only a certain part of the spread particle fan has the right deflection angle to follow the kinked beam pipe. As the deflection is dependent on the particle energy, these particles have similar energies. The energy is Gaussian distributed about an ideal energy for this specific deflection angle. The particles with this energy are moving along the ideal path through the beam pipe.

The part of the particle fan, which entered the kinked beam pipe, is then collimated by a horizontal and vertical collimator in order to narrow the Gaussian energy distribution. The collimators are both built up by two tungsten blocks close to each other. The particles hitting the tungsten blocks are stopped, the others continue through the gap between the two blocks.

The test beam users can here make a choice again. The two blocks of both the horizontal and the vertical collimator can be moved apart or brought together arbitrarily. The collimation is therefore less (stronger) and the Gaussian energy distribution broader (narrower). The most commonly used setting is a gap of 1 cm between the two blocks for both collimators (see Figure 5.24). In Figure 5.25 plots of the electron position in the xy-plane are shown directly after the collimation by the horizontal and vertical collimator.
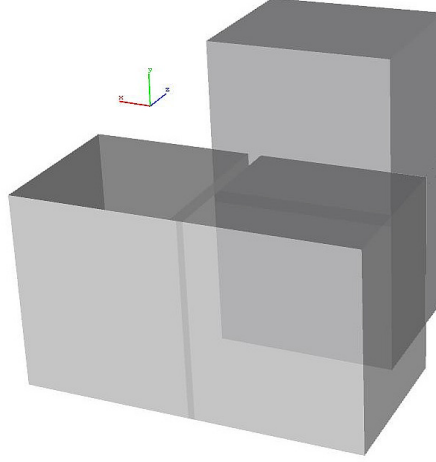
Figure 5.24.: *The simulation of the horizontal and vertical collimators of the test beam lines are visualised with a VRML viewer. The gap between the tungsten blocks of both of the collimators is here set to 1 cm. The horizontal and vertical collimators are about 7.9 cm apart from each other.*

(a)   (b)
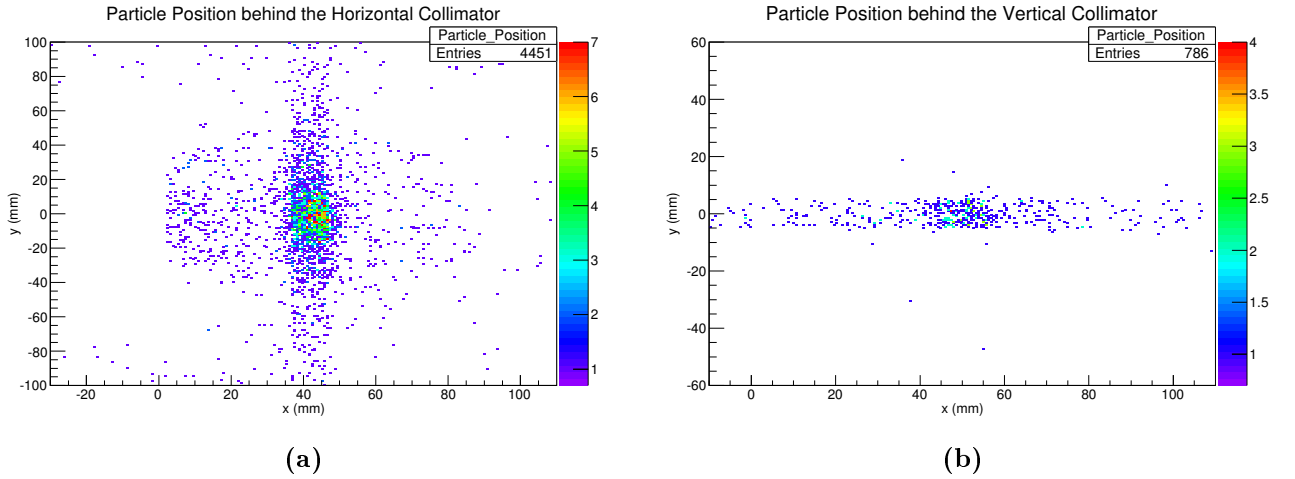
Figure 5.25.: *Plots of the electron x-/y-position directly behind the horizontal and vertical collimator of test beam line 21. The gaps between the blocks of both of the collimators are defined to be 1 cm. The blocks absorb particles that do not pass through the collimator gaps.*

Figure 5.26.: *Photos of the collimator in the test beam areas. The beam enters the test beam area through the beam pipe and is collimated by the shown collimator. The user can chose from insertions with holes of different sizes from 2 mm × 2 mm up to 1 cm × 1 cm.*

5.7. Final collimation in the test beam area

Finally, the test beam enters the test beam area through the beam pipe window. Between the DESY-II tunnel and the test beam hall with its areas, there are up to 5 m thick walls made out of radiation safety concrete, which contains about 90 % iron.[2] Figure 5.27 shows the simulated test beam line with a trajectory of a geantino, which is a virtual particle for GEANT4 simulations and only undergoes transportation processes. [33]

In the test beam area, the test beam is again collimated. This final collimation is dependent on the choice of the test beam user, since there are several insertions with different hole sizes available for the collimator block. One of the insertion is shown in Figure 5.26. Like the collimator block, the insertions are made out of lead.
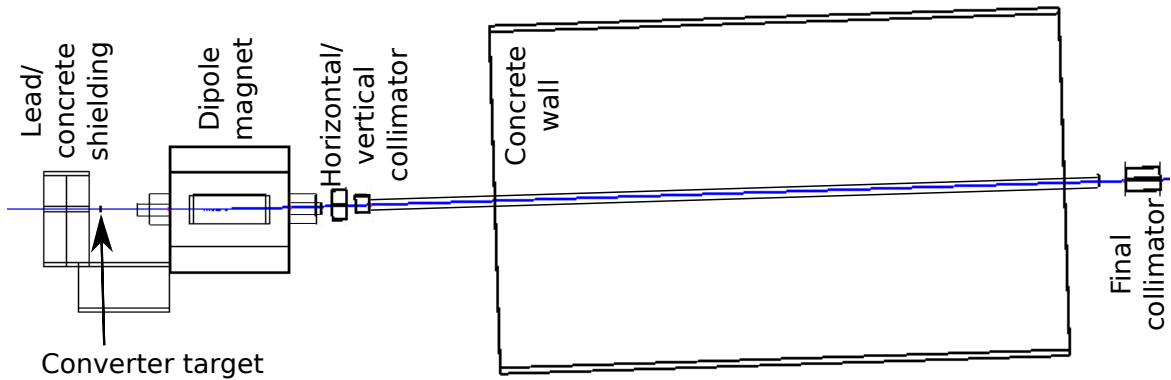
Figure 5.27.: *Visualisation of a geantino trajectory in the test beam line 21. The view is on top of the geometry, so that the particle is coming in from the left hand side and passes through the single components of the test beam line.*

---

[2]Heavy concrete contains in comparison to radiation safety concrete only about 5 % iron.

As the DESY-II synchrotron beam bunch hits the primary targets of the test beam lines with a rate of 1 MHz [18], the measured test beam rates are overlying particle streams from several different DESY-II beam bunches. The mean rate of the final test beam in the test beam areas is about 8 kHz for the copper converter target with 5 mm thickness. Translating this to the number of final test beam particles from only one DESY-II beam bunch, yields a number of 0.008 particles.

Hence, for significant statistics, the simulation of the test beam generation with one beam bunch was repeated 200 times each for six different magnetic field strengths. Additionally, the size of the final collimator hole was set to be 1 cm×1 cm, which is the largest possible hole size. The following plots show data from these repeated simulations, which are taken directly behind the final collimator.

The sensitive tracker planes, that are put behind the final collimator in the geometry description, retain information about the time of the hit in respect to the start of the simulation. Figure 5.28 shows this time distribution for the electrons of the final test beam generated in the test beam line 21 from 200 DESY-II bunches. The small tail of the time distribution is caused by beam particles whose path along the test beam line is slightly longer due to, for example, multiple scattering.
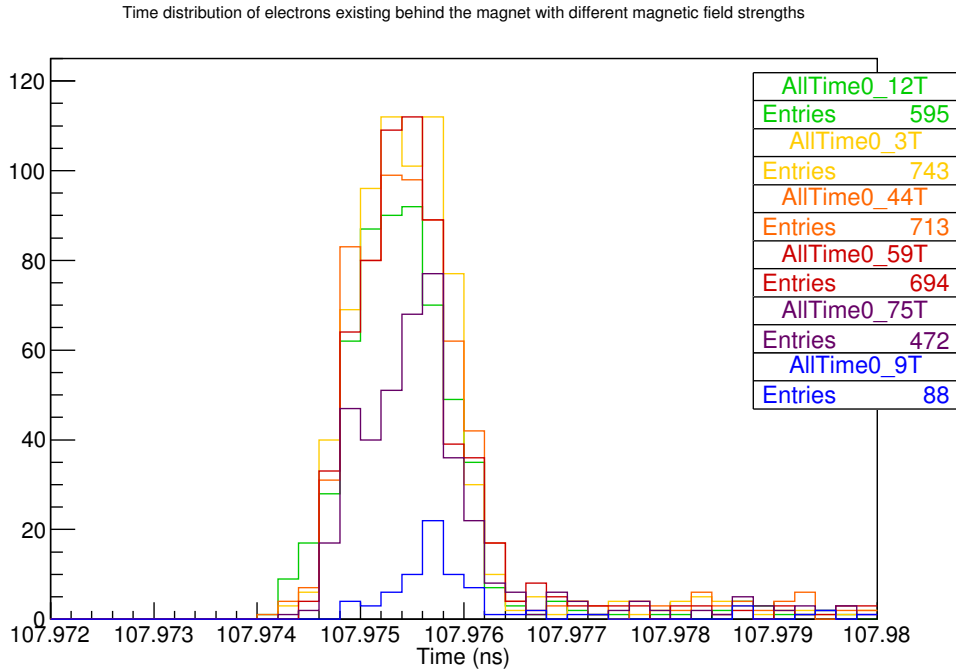
Figure 5.28.: *Plot of the time distribution of the test beam generation for the test beam line 21. The plotted time is the time between the start of the simulation, i.e. the DESY-II beam bunch hitting the primary target, and the test beam particles entering the test beam area. The simulation of the test beam was done for six different magnetic field strengths between B = 0.12 T and 0.9 T. Due to the different magnetic field strengths, the final test beam has a different mean energy, e.g. B = 0.9 T corresponds with a test beam energy of about 6 GeV (cf. Figure 5.29).*

Of great interest is the energy distributions of the test beam for different dipole magnet settings. Since the beam is collimated twice, the Gaussian energy distributions are narrow. Measured distributions have a width of about 5 %. Additionally, the linear dependency between the magnetic field strength of

the test beam magnet and the particle energy is shown for a comparison to the plot in Figure 3.3.
Figure 5.29 shows the energy distributions for six different magnetic field strengths between 0.12 T and 0.9 T. With the given statistics, the distributions have a spread of 1.5% - 12.8%.

An interesting point is that for all magnetic field strengths, there is a small number of particles with energies below 0.5 GeV. In Figure 5.30 (b) which shows the added up distributions of the particle energy, this leads to a significant count of particles with energies of 1 GeV and lower. When a cut is applied on the simulated data such that only particles with energies of the mean value$\pm\sigma$ from the single energy distribution fits are taken into account, the plot of the particle count in dependency on their energy becomes a Gaussian distribution (see Figure 5.30 (a)) as expected from Figure 3.2 in Chapter 3.2. However, Figure 3.2 only shows the expected rate for a certain particle energy. The simulation indicates that there are always particles with energies smaller than 0.5 GeV, because of particle interactions with the collimator and shielding material. The rate for particles with energies smaller than 1 GeV is therefore higher than expected, as shown is Figure 5.30 (a).
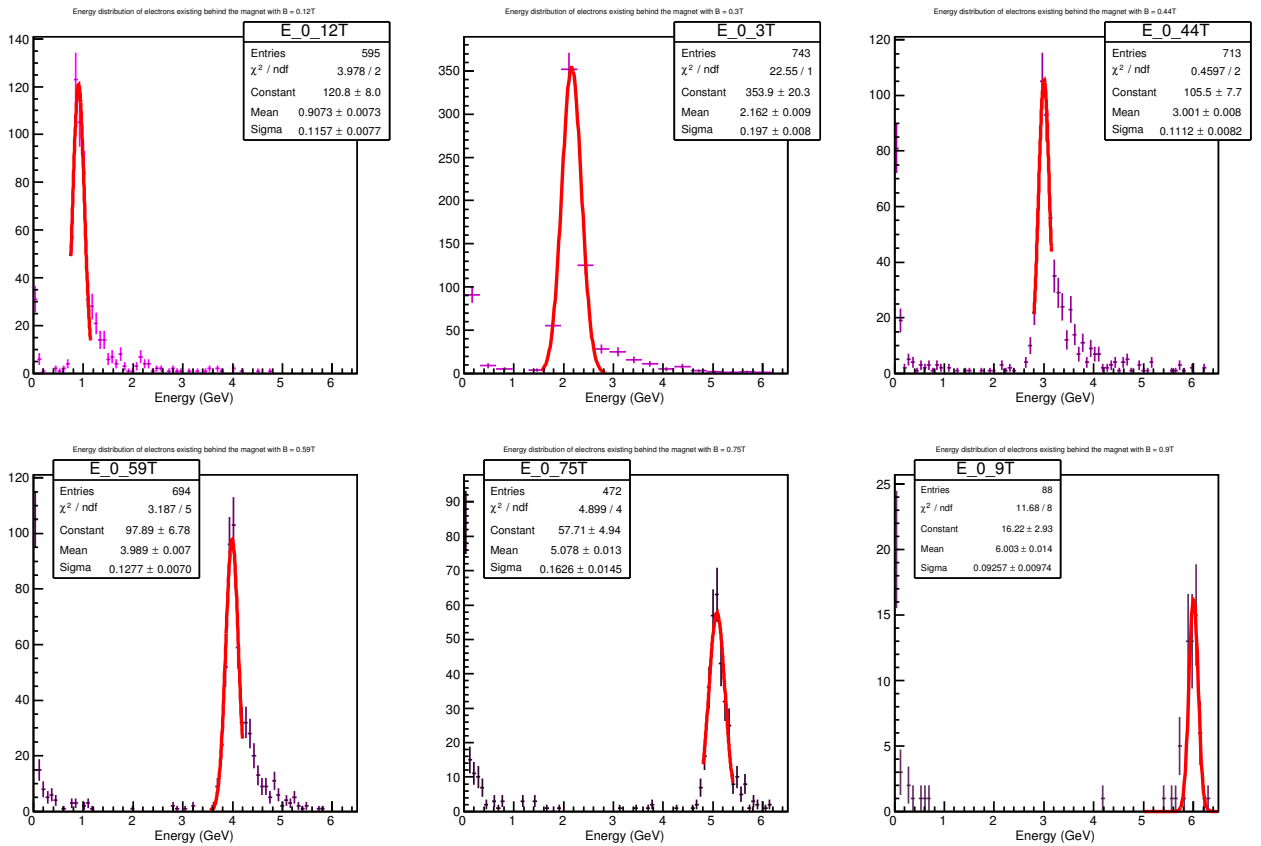
Figure 5.29.: *Plots of the energy distributions of the simulated test beam for different magnetic field strengths of the dipole magnet of the test beam line 21. The magnetic field strengths range from 0.12 T to 0.9 T. For each plot, the full simulation of the test beam line was repeated 200 times, so that the distributions are directly comparable.*

Finally, the particle energy is plotted over the magnetic field strength (see Figure 5.31). The plot is a profile plot and shows the average energy of the final test beam for a certain magnetic field strength

(a)

(b)
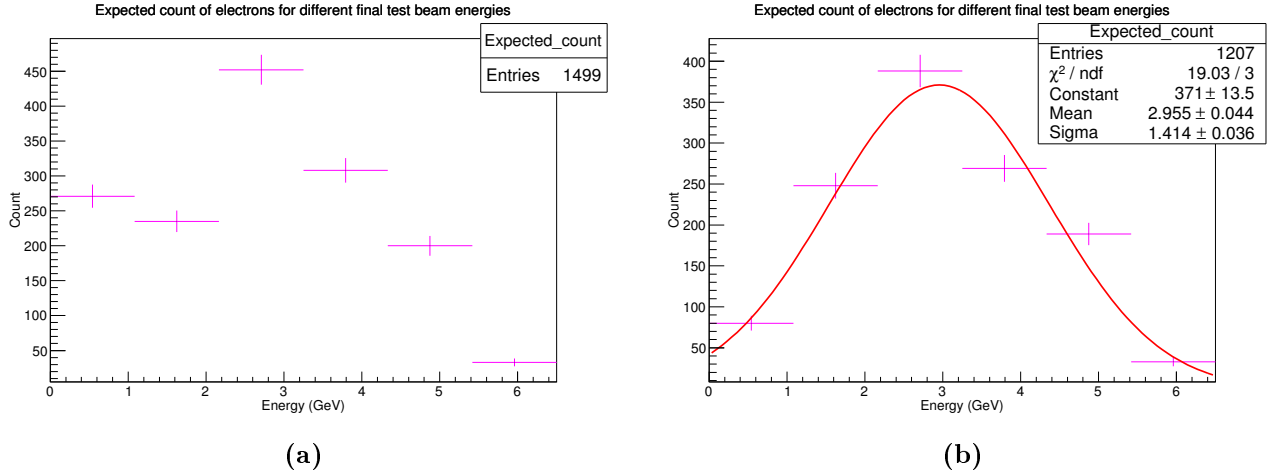
Figure 5.30.: *Plots of the electron count in the test beam area after the final collimation with respect to the electron energy. Figure (a) shows a plot of the added up energy distributions of Figure 5.29 for the six different magnetic field strengths. Due to the count of particles with energies smaller than 0.5 GeV, Figure (a) shows a higher count of particles with energies up to 1 GeV than expected. When a cut is applied on the particle energy for the first bin such that only particles with energies around the mean value of the energy distribution (from Figure 5.29) contribute to the distribution, the particle count is Gaussian distributed (Figure (b)).*

of the dipole magnet. Hence, one can read from the figure which beam energy is to be expected, when a specific magnetic field strength is set for the test beam magnet. The relationship between the energy and the field strength is linear, as expected from Figure 3.3.

The experimental setup of the test beam users is built up about 2 m behind the final collimator or further. The ideal beam path has an angle of 32 mrad to the z-axis in the xz-plane (since the beam line is kinked by 32 mrad), and no angle in the yz-plane. Figures 5.32 (a) and (b) show that the angle between the path of the particles coming out of the collimator and the z-axis in the xz- and yz-plane is Gaussian distributed about the ideal beam path angles, which means that the beam widens isotropically. The maximum angle to the ideal beam path is about 0.002 rad (0.115°). With a quick calculation as in Equation 5.2, one can obtain that the beam will widen in such a way that 2 m behind the collimator its radius will have a value of about 23 cm.

$$tan(\alpha) = \frac{x}{z}$$
$$\rightarrow x = 2\,\text{m} \cdot tan(0.002\,\text{rad}) \tag{5.2}$$
$$x = 0.23\,\text{m}$$

As the DESY-II beam bunch hits the primary targets of the test beam lines with a rate of 1 MHz, the particle counts shown here in Figures 5.29 and 5.30 have to be scaled up with a factor of 5 000 Hz $\left(\frac{1\,\text{MHz}}{200}\right)$. This leads with a maximum count of about 350 simulated particles (for 200 simulated DESY-II beam bunches) to a maximum rate of about 1,750,000 Hz. The discrepancy to the measured rates in the test beam area could be due to the fact that the simulated rate is given directly behind the final

Particle energy as a function of the magnetic field strength

E_vs_B_pfx	
Entries	2760
Prob	0.006509
p0	0.4908 ± 0.0257
p1	6.045 ± 0.060

B (T)
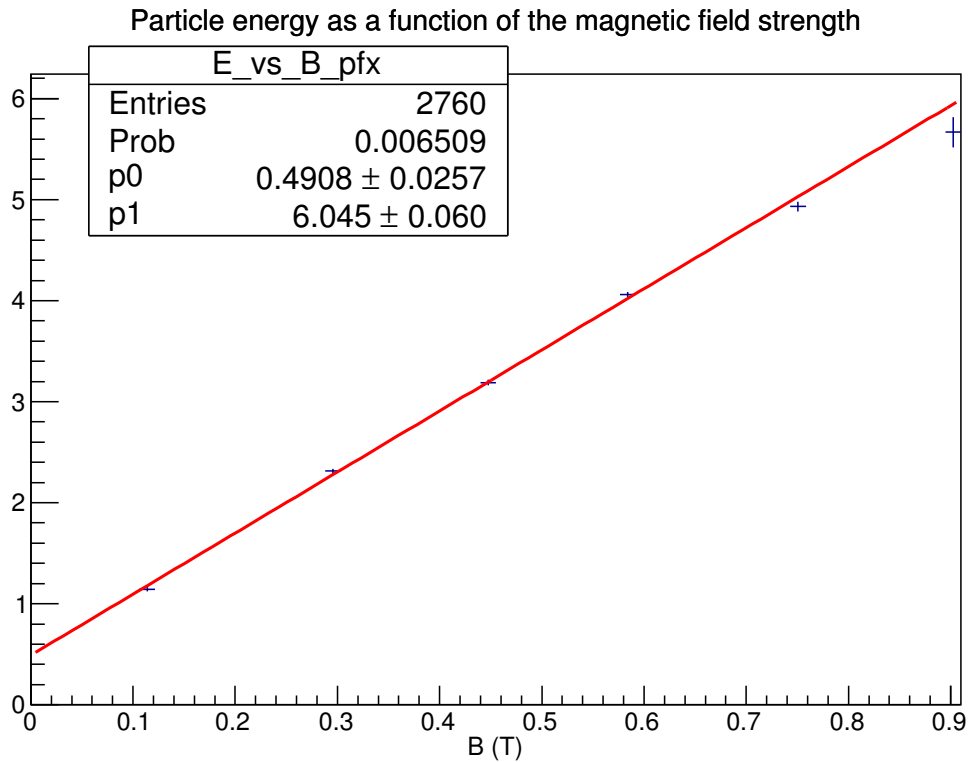
Figure 5.31.: *Profile plot of the particle energy of the simulated test beam as a function of the magnetic field strength of the dipole magnet of the test beam line 21. The plot shows the average energy for one magnetic field strength. As so far only six different magnetic field strengths were simulated, six average energies are plotted.*

collimator, whereas the measured rates were measured in the test beam area metres away from the collimator. Because the final test beam widens isotropically, only a fraction of the beam was measured. Further investigations on the beam rates are necessary to explain this large discrepancy.

5.8. The flux maps of the test beam lines

With the knowledge of the particles' properties as well as of the vertex, its endpoint, and certain positions in the simulated world, one can obtain a propagation path of the test beam particles in the simulated world.

A distinction is made between several cases of particle propagation: along a straight path outside the magnetic field, along a bent path in the magnetic field of the dipole magnet and along a continued path after being bent in the field. By taking the different cases into account, the particle's path can calculated. The position along this path after every 1 mm can be filled into a two dimensional plot, which has bins of size 1 mm × 1 mm. As the defined coordinate system for the simulation is a right handed one with the z-axis as the beam path, the two dimensional maps show the xz plane. For a high number of particles, one can read the flux of particles through an area of 1 mm × 1 mm from the map. Bins along a single particle's path show therefore the trajectory of that particular particle. The colour

(a)   **(b)**
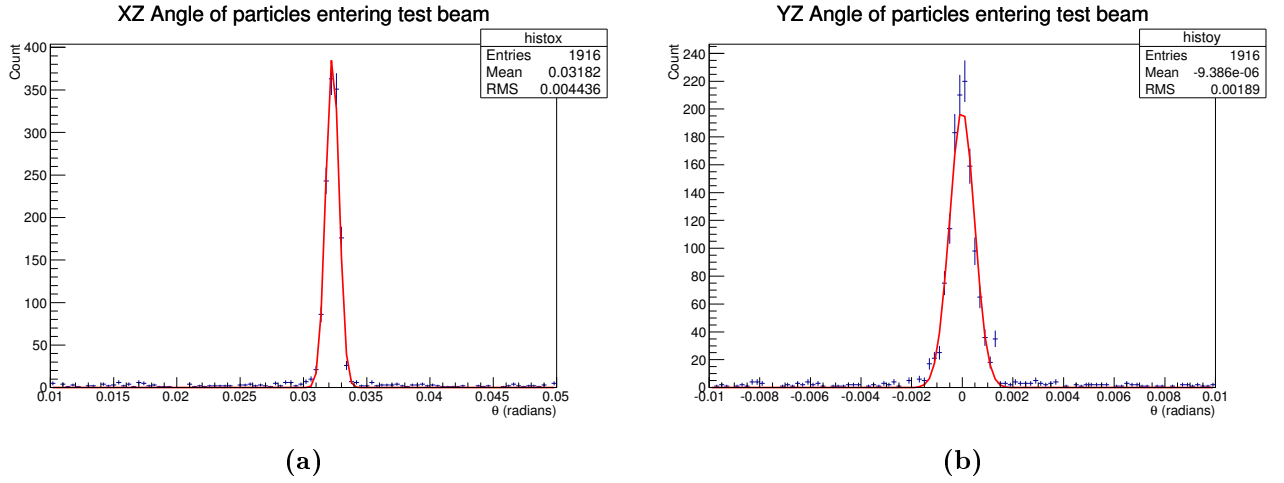
Figure 5.32.: *The plots show the angle in Radians between the particle's path and the z-axis for particles which entered the test beam area. As the test beam line is kinked in the xz-plane after the test beam magnet, it has an angle of 32 mrad to the z-axis. This is visible in Figure (a) as the mean value of the angle distribution in the xz-plane for the particles entering the test beam area. In Figure (b), which shows the angle between the path and the z-axis in the yz-plane, the distribution is centred at zero and uniformly spread in positive and negative directions. The particles therefore leave the final collimator isotropically.*

(a)   **(b)**
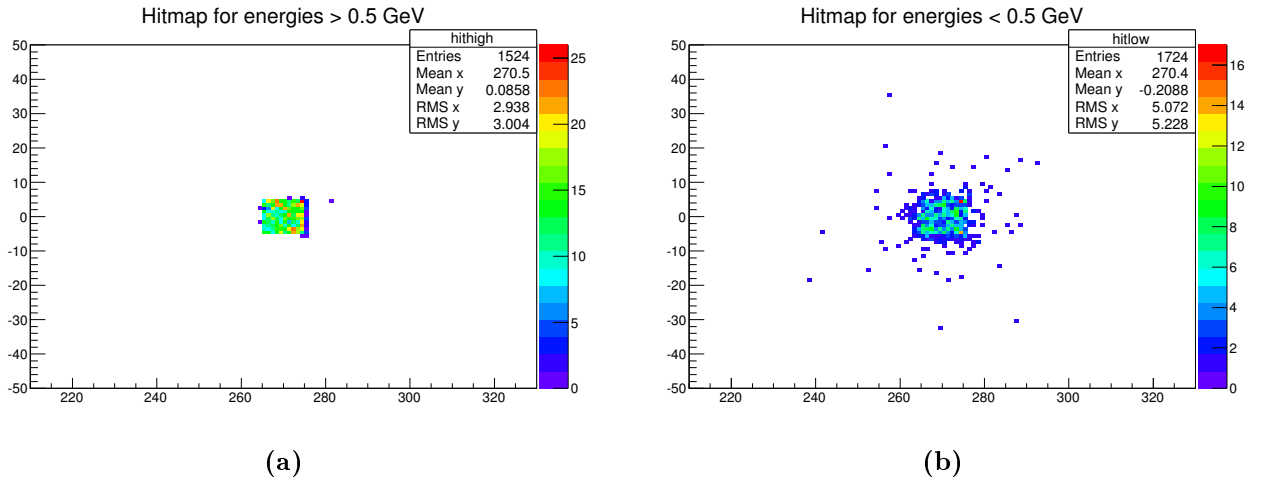
Figure 5.33.: *These two scatter plots show the position in the xy-plane of particles entering the test beam area through the final collimator. It is therefore a view on the back of the collimator, which has a hole of 1 cm×1 cm. Figure (a) shows the particle positions for all particles with kinetic energies of higher than 0.5 GeV, Figure (b) in contrast shows only particles with kinetic energies of less than 0.5 GeV.*

axis of the plots indicates the number of particles for the single bins.

The `C++` program is written in such a way that a flux map can easily be drawn for single particle types as well as for all particles. Figure 5.34 shows hence the trajectories of electrons and positrons, Figure 5.35 of photons passing through the simulated world before the dipole magnet of the test beam line.
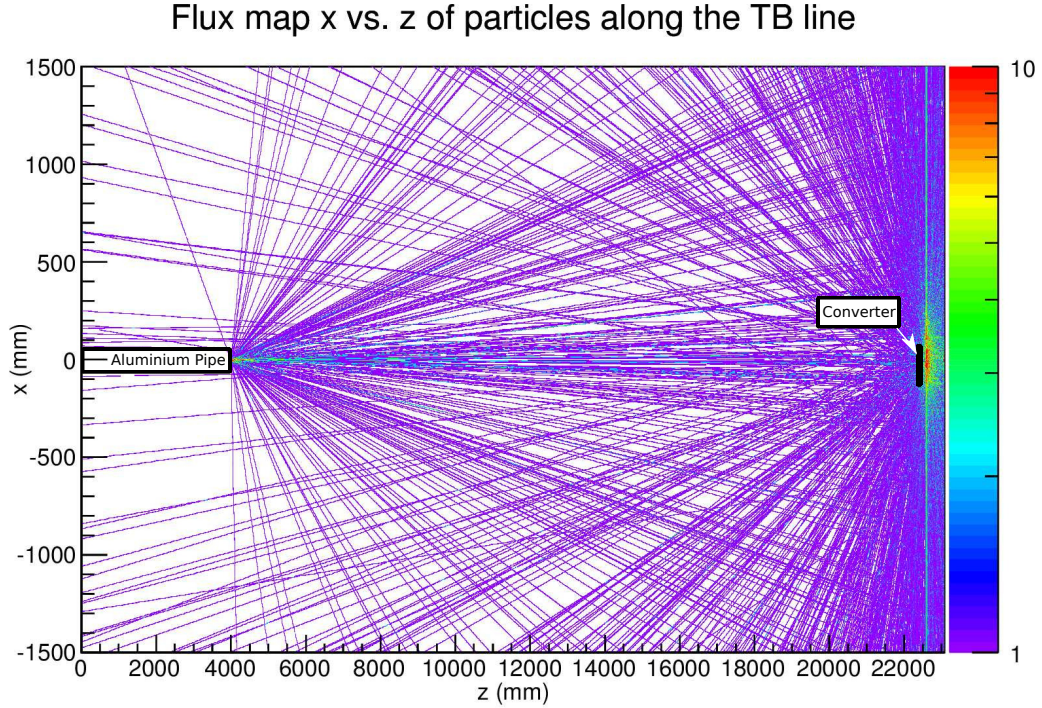
Figure 5.34.: *A xz-flux map of electron and positron fluxes at the DESY test beam line 21. The primary target is positioned at (0, 0), the converter plate at (0, 23069 mm). At (0, 4000 mm), the beam pipe ends with an aluminium window, where electrons and positrons are created due to pair production. The z-scale is only going up to 10, as the majority of electrons and positrons are created not before the converter plate. The number of secondary electrons/positrons is small so that the single trajectories are visible.*

It is clear that the vast majority of electrons and positrons are produced in the converter target due to photon conversion, but also that there are secondary electrons/positrons before the secondary target. The flux map shows that these secondary electrons/positrons originate primarily at (0, 4000 mm). This is the position of the aluminium beam pipe window of the beam pipe connected to the DESY-II synchrotron ring. Figure 5.35 shows the occurring photons in the simulation, it becomes clear that at (0, 4000 mm) the bremsstrahlung photons hit the aluminium pipe window and pair produce these secondary electron/positron pairs. Behind the converter target at (0, 23069 mm), the electrons and positrons, as well as unconverted and scattered photons are entering the bending dipole magnet. Figure 5.36 shows the deflection of electrons in the homogeneous magnetic field. With the knowledge of the particle momentum and charge the radius of the circular path was calculated with Equation 2.23 from Chapter 2.4. After small step sizes of the deflection angle, the particle position is recalculated and filled into the flux map.
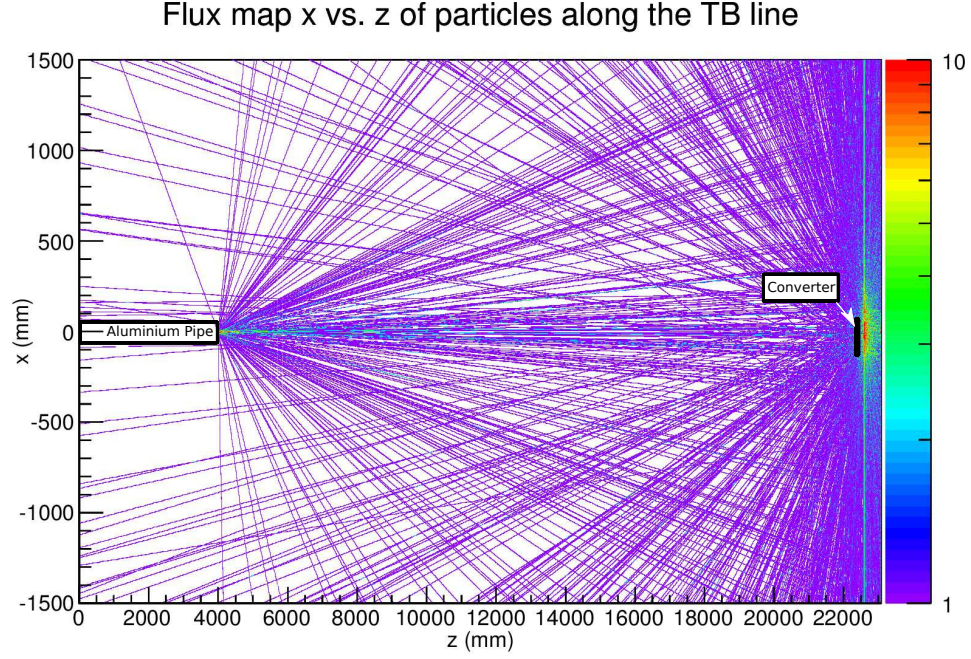
Figure 5.35.: *A xz-flux map of photon fluxes at the DESY test beam line 21. The primary target is positioned at (0, 0), the converter plate at (0, 23069 mm). The distinct photon beam at $x \approx 0$ mm is the primary bremsstrahlung photon beam emitted from the carbon fibre. The photons also scatter with the beam pipe window at (0, 4000 mm) and primarily with the secondary target.*
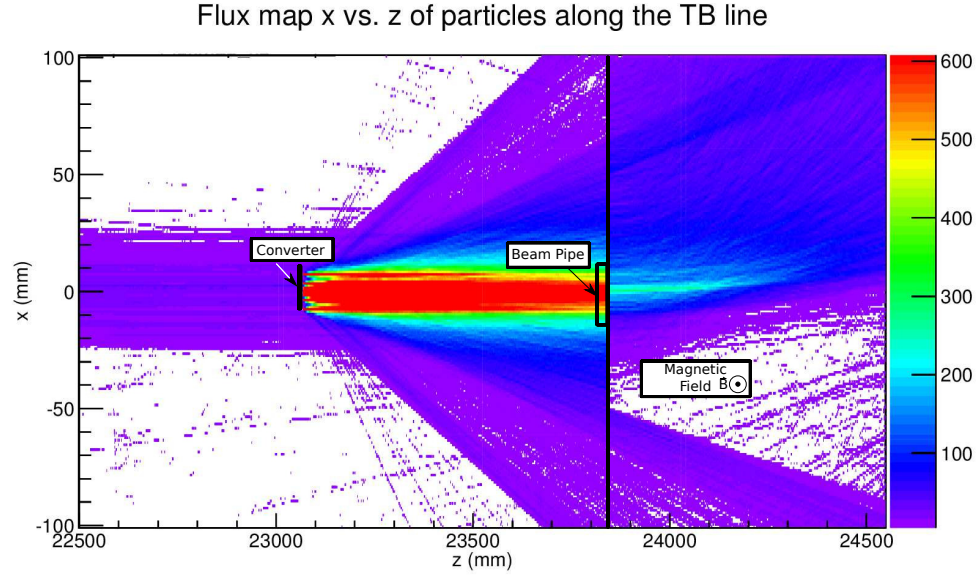
Figure 5.36.: *A xz-flux map of electron fluxes in the dipole magnet of the DESY test beam line 21. The particles were simulated in a full test beam line simulation, for a magnetic field strength of $B = 0.59$ T. The magnetic field reaches from $z = 23845$ mm to $z = 24555$ mm.*

6 Chapter 6.
Results and conclusion

After a short summary, a conclusion about this Master's Thesis and a reflection about possible improvements of the simulation of the DESY-II test beam lines follow.

For the GEANT4 Monte Carlo simulation of the DESY-II test beam lines, the geometry of the test beam line components was described in GDML format, and different GEANT4 event generators were tested. From the GDML geometry descriptions, VRML files were created to visualise the simulated components and to check for flaws in the geometry description. The simulation model is highly flexible, such that changes in the geometry description and adding new test beam line components is easily implemented. The whole geometry of the test beam line 21 is shown in Figure 6.1, which is the visualisation of the simulated test beam line geometry.

The first step was to simulate the beam bunch of the DESY-II synchrotron, which consists of 10^{10} electrons at an energy of 6.3 GeV. By hitting the primary target, bremsstrahlung photons are emitted, travel along the test beam line and are converted to electron/positron pairs. The physics processes of the test beam generation were studied by analysing the simulated data and visualising the particles' positions at different points along the beam path. With the information about the particle momentum and position, two dimensional maps of the particles' trajectories and the particle flux in the xz-plane were created.

By verifying the particles' paths and the beam composition, it was noticed that secondary hadronic particles, like neutrons and protons, and secondary electrons and positrons, are also occurring during the test beam generation. The cause of their occurrence is the interaction of the bremsstrahlung photons and the synchrotron radiation from the DESY-II synchrotron with the material of the test beam line components. The simulation of GeV particles hitting different shielding materials was used to study the shieldings' performance at stopping undesired particles. The results were taken into account for the decision on the material and the thickness of shieldings in front of the secondary targets. A direct result of this project is that secondary particles as well as synchrotron radiation from the DESY-II synchrotron ring are now stopped from hitting the secondary target and from entering the test beam dipole magnet.

Different converter targets were simulated to compare their photon conversion efficiency. The simulation of a magnetic dipole field was tested in several ways by calculating theoretically the deflection angle between the initial and final direction of a particle with a certain energy, and comparing the prediction to the simulation. In the end, 1200 full simulations of the test beam lines were performed to gain adequate statistics for plotting the energy and its spread of the final test beam for different
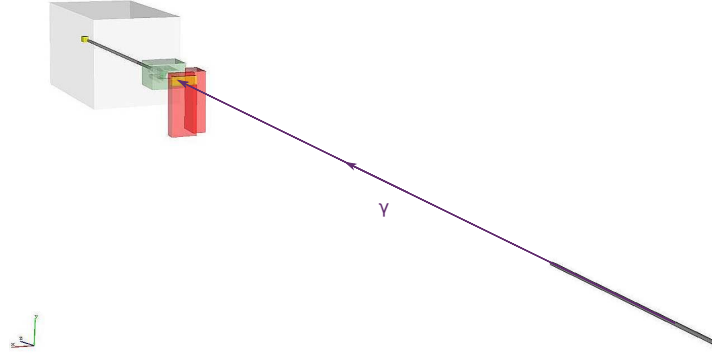
Figure 6.1.: *The simulation of the test beam line 21 is visualised with a* VRML *viewer. Additionally, the direction of the bremsstrahlung photon passage towards the lead/concrete shielding and the secondary target is schematically drawn into the model.*

magnetic field strengths of the test beam magnet. The results for the particle energy and its spread are listed in Table 6.1. The rate of the final test beam is dependent on the magnetic field strength and has a maximum at a magnetic field strength of about 0.44 T, which yields a final test beam energy of about 3 GeV. Scaling up the particle counts to beam rates with respect to the number of simulated DESY-II bunches leads to values in the MHz range. The large discrepancy between the simulated and measured test beam rates has to be investigated further.

Additionally, the distribution of the time between the start of the simulation and the final beam entering the test beam area was shown. The time distributions are very narrow with similar mean values between 107.974 ns and 107.977 ns, so that the dispersion of the test beam is small. The strength of the magnetic field does not therefore affect the time of flight of the final test beam particles.

The simulation done in the course of this Master's Thesis comprises a model of the DESY-II synchrotron beam bunch and a full description of the components of the DESY test beam lines which allow the generation of the test beams. With this, various studies of the physics processes of the test beams and their beam attributes can be done by varying the simulation's settings and observing the effect on the simulated test beam. Such studies can be, for example, extending the simulation of the test beam lines in respect of implementing all possible settings for all test beam lines, such as different converter materials and thickness, different collimator gaps, and magnetic field strengths of the test beam line magnets. More full simulations with different settings will reduce statistical errors in the analysis, and also provide the test beam users with tables of possible settings of the test beam lines and the effect to be expected on the final test beam attributes. The three test beam lines are very similar but have slightly different geometries, hence a precise measurement of the components and distances between the component positions would reduce systematic errors, as the simulation's result is highly dependent on the geometry description.

Additional improvements would be to implement a full field map of the dipole magnets into the simulation to guarantee a even more realistic deflection of the particles in the dipole magnets. It requires precise measurements of the magnetic field strength over the full volume of the test beam magnets. By studying new materials for the secondary target, an optimal converter target could be found to provide higher rates of the final test beam. Further potential extensions of the simulation might be the optimisation of the positions of present or additional collimators in order to minimise the energy spread of the test beam.

B (T)	Mean energy (GeV)	σ (GeV)	Energy spread (%)
0.12	0.907	0.116	12.752
0.30	2.162	0.197	9.112
0.44	3.001	0.111	3.705
0.59	3.989	0.128	3.201
0.75	5.078	0.163	3.202
0.90	6.003	0.093	1.542

Table 6.1.: *Table of the final results for the particle energy and its spread for the final test beam (cf. Figure 5.29). The results are gained from 200 full simulations for each magnetic field strength.*

In respect to the studies of the beam purity, a great optimisation of the simulation would be to accurately model the synchrotron radiation emitted from the DESY-II accelerator. The synchrotron radiation photons interact with the test beam line components and produce secondary particles, which not only affect the particle rates in the DESY-II tunnel but have also a high probability to continue on the test beam line. They will be visible as off-momentum background particles and lead to a higher energy spread.

Regarding the simulation program, the event generation could be improved by feeding the Geant4 General Particle Source with user defined distributions of the particles' energy and their positions and directions. These user defined distributions can for example come from histograms of measured data of the test beam or the DESY-II beam bunch. Since the DESY-II synchrotron is a pre-accelerator and injector, it is mainly running in top-up mode for PETRA-III. Implementing a full DESY-II machine cycle with its injection and extraction modes into the simulation would lead to a real time visualisation of the particle fluxes and test beam attributes. By doing so and additionally introducing more readout points in the simulation, the tracks of the individual particles can be stored and used for tracking the simulated particle. A precise analysis and creating flux maps matching reality will be possible.

Measuring the beam attributes at several points along the beam line and the test beam generation would allow a comparison between simulated and measured data, and at the same time give the possibility to use the measured data for tuning the event generators and the settings of the simulated test beam line towards even more realistic simulations.

The complete understanding of the beam parameters and behaviour will reduce systematic uncertainties for detector studies, as the test beam users can adjust their experimental setup and analysis tools appropriately with the help of the available simulation results.

With the simulations done for this Master's Thesis and the very precise modelling of the test beam lines, it is the first time that a Geant4 simulation for the DESY test beam facility has been implemented. By making the simulation tool available on GitHub many further studies are now possible.

7 Chapter 7.
Summary

As one of very few test beam facilities in the world, the DESY-II test beam facility provides users from all over the world with three high rate particle beams in the GeV range. For gaining detailed understanding of the test beam generation and its dependency on the beam attributes, a GEANT4 Monte Carlo simulation of the test beam lines was set up.

A realistic modelling of the beam bunch of the DESY-II synchrotron as well as the very precise geometry description of all test beam line components were needed to implement this full simulation tool. The magnetic field strength of the simulated test beam dipole magnet was varied to examine the dependency on the final beam energy and its spread.

The analysis of the simulated data also yielded knowledge about the particle fluxes of primary and secondary particles, so that the simulation of the test beam lines already provided essential input for the 2014 shutdown maintenance work. Additional shieldings were built up for stopping undesired particles from continuing on the test beam lines and affecting the energy distribution and beam purity of the final test beams.

The set up simulation will be used as a fully flexible GEANT4 Monte Carlo tool for further simulation studies of the DESY-II test beam lines. Due to its ease of use, more detailed studies are now possible to find possible optimisations of the geometry of the test beam lines. The information gained will then be useful for the shutdown activities and DESY-II test beam upgrades in following years.

A Appendix

The appendix contains parts of `C++` programs written so far for the simulation of the secondary target. Explanations to single lines in the code are given as comments in the programs themselves.

A.1. Appendix I

A.1.1. Physical constants and variables

Symbol	Definition	Value/ unit
K	$4\pi N_A r_e^2 m_e c^2$	0.307075 MeV mol^{-1} cm^2
α	Fine structure constant $\frac{e^2}{4\pi\epsilon_0 \hbar c}$	$\approx 1/137.036$
N_A	Avogadro's number	$6.02214129(27) \times 10^{23}$ mol^{-1}
r_e	classical electron radius $\frac{e^2}{4\pi\epsilon_0 m_e c^2}$	$2.8179403267(27)$ fm
$m_e c^2$	electron mass $\times c^2$	$0.510998928(11)$ MeV
z	charge number of incident particle	
Z	atomic number of absorber	
A	atomic mass of absorber	g mol^{-1}
β	ratio of velocity v to the speed of light c	
γ	Lorentz factor $\frac{1}{\sqrt{1-v^2/c^2}} = \frac{1}{\sqrt{1-\beta^2}}$	
δ	density effect correction to ionization energy loss as a function of $\beta\gamma$	
W_{max}	maximum energy transfer in a single collision $\frac{2m_e c^2 \beta^2 \gamma^2}{1+2\gamma m_e/M+(m_e/M)^2}$; $W_{max} = 2m_e c^2 \beta^2 \gamma^2$ (for $2\gamma m_e \ll M$) $W_{max} = Mc^2\beta^2\gamma$ (for $2\gamma m_e \gg M$)	
M	mass of incident particle	MeV/c^2
I	mean excitation energy	eV

Table A.1.: *Table of variables used in various equations in Chapter 2.*

A.1.2. List of converter target for the test beam lines 21, 22 and 24

A list of all available converter targets for the test beam lines 21, 22 and 24 is available on the DESY
test beam web page [20]. The pdf file is shown here:

```
Norbert Meyners, MEA (3321, norbert.meyners@desy.de)

Conversion targets

There are different conversion targets available. They are
controlled from a NIM-box in the hut and can be changed by
choosing a new number at the box.


Testbeam 21              (Last update  February 7, 2007)

number  target  thickness       seize (w x h)
1               Cu              5mm             45mm x 60mm
2               Cu              4mm             45mm x 60mm
3               Cu              3mm             45mm x 60mm
4               Al              3mm             45mm x 60mm
5               Al              2mm             45mm x 60mm
6               Al              1mm             45mm x 60mm
7               Cu wire         1mm
8               notthing
(Please note that there is a 0.5mm Aluminium
window roughly 20m before the conversion target.)


Testbeam 22              (Last update  February 7, 2007)

number  target  thickness       seize (w x h)
1               Cu              5mm             45mm x 60mm
2               Cu              1mm             45mm x 60mm
3               Cu              3mm             45mm x 60mm
4               Al              4mm             45mm x 60mm
5               Al              3mm             45mm x 60mm
6               Al              1mm             45mm x 60mm
7               Cu              10mm            45mm x 60mm
8               notthing
(Please note that there is a 0.5mm Aluminium
window roughly 16m before the conversion target.)


Testbeam 24              (Last update  February 7, 2007)

number  target  thickness       seize (w x h)
1               Cu wire         1mm
2               Cu              4mm             45mm x 60mm
3               Cu              3mm             45mm x 60mm
4               Al              3mm             45mm x 60mm
5               Al              2mm             45mm x 60mm
6               Al              1mm             45mm x 60mm
7               Cu wire         1mm
8               notthing
(Please note that there is a 0.5mm Aluminium
window roughly 50mm before the conversion target.)

--------------------------------------------------------------
                targets.txt page        August 27, 2002 16:31
```

A.1.3. Table of settings for the magnet currents and corresponding beam energies

The given list of the settings for the current through the dipole magnets of the test beam lines and the corresponding final beam energies is given currently in the control huts of the test beam areas.

	TB21 + 22 + 24	TB24
PS:	ER400/xx	MK1500/xx
Energy	Magnet_MR	Magnet_MB
[GeV]	I[A]	I[A]
1	37,462	66,92
1,2	45,0	80,30
1,4	52,4	93,69
1,6	59,9	107,07
1,8	67,4	120,45
2	74,9	133,84
2,2	82,4	147,22
2,4	89,9	160,61
2,6	97,4	173,99
2,8	104,9	187,37
3	112,4	200,76
3,2	119,9	214,14
3,4	127,4	227,53
3,6	134,9	240,91
3,8	142,4	254,29
4	149,8	267,68
4,2	157,3	281,06
4,4	164,8	294,44
4,6	172,3	307,83
4,8	179,8	321,21
5	187,3	334,60
5,2	194,8	347,98
5,4	202,3	361,36
5,6	209,8	374,75
5,8	217,3	388,13
6	224,8	401,51

N.Meyners, MEA1   22.02.2011

Figure A.1.: *Table of the currents through the magnets of test beam line 21, 22 and 24 and the corresponding beam energies.[1]*

A.2. Appendix II: Code sections from programs for the simulation and analysis

A.2.1. DESY-II beam bunch: SLIC macro using GPS as the event generator

```
 /lcio/PDGFlag true
/lcio/filename DESY_II_beam.slcio
/lcdd/url ./DESY_II_beam.lcdd

/run/initialize
/generator/select gps
/gps/particle e-
/gps/pos/type Beam
/gps/pos/halfx 1.53 mm
/gps/pos/halfy 0.753 mm
/gps/pos/centre 0 0 0 cm
/gps/direction 0.  0.  1.
/gps/ene/type Gauss
/gps/ene/mono 6.3 GeV
/gps/ene/sigma 6.17249 MeV

/random/seed
/run/beamOn 10000000000
```

A.2.2. TB line 21: Full geometry description

A.2.2.1. The GDML file

```
<gdml>
 <define>
    <constant name="world_side" value="32370." />
    <position name="Position_of_LeadShieldingHole" x="100." y="-50." z="0." />
    <position name="Position_of_ConcreteShieldingHole" x="100." y="-75." z="0." />
    <rotation name="RotatePassthrough" y="-0.032" unit="rad"/>
    <position name="BeamPipe_Connection_HolePosition1" x="-30." y="0." z="0." unit="mm"/>
    <position name="BeamPipe_Connection_HolePosition2" x="5." y="0." z="0." unit="mm"/>
    <position name="center" x="0." y="0." z="0." unit="mm"/>
 </define>

 <materials>
    <element Z="1" formula="H" name="H">
      <atom type="A" unit="g/mol" value="1.00794" />
    </element>
    <element Z="6" formula="C" name="C">
      <atom type="A" unit="g/mol" value="12.0107" />
```

```
</element>
<element Z="7" formula="N" name="N">
  <atom type="A" unit="g/mol" value="14.0068" />
</element>
...more elements...

<material name="Air">
  <D type="density" unit="g/cm3" value="0.0012" />
  <fraction n="0.754" ref="N" />
  <fraction n="0.234" ref="O" />
  <fraction n="0.012" ref="Ar" />
</material>

<material name="Aluminium">
  <D type="density" value="2.702" unit="g/cm3"/>
  <fraction n="1.0" ref="Al"/>
</material>

<material name="Lead">
  <D type="density" value="11.342" unit="g/cm3"/>
  <fraction n="1.0" ref="Pb"/>
</material>

<material name="Iron">
  <D type="density" value="7.874" unit="g/cm3"/>
  <fraction n="1.0" ref="Fe"/>
</material>

<material name="Copper">
  <D type="density" value="8.96" unit="g/cm3"/>
  <fraction n="1.0" ref="Cu"/>
</material>

<material name="Kapton">
  <D type="density" value="1.42" unit="g/cm3"/>
  <fraction n=".026362" ref="H"/>
  <fraction n=".691133" ref="C"/>
  <fraction n=".073270" ref="N"/>
  <fraction n=".209235" ref="O"/>
</material>

<material name="Tungsten_S17">
  <D type="density" value="17.0" unit="g/cm3"/>
  <fraction n="0.90" ref="W"/>
  <fraction n="0.05" ref="Cu"/>
  <fraction n="0.05" ref="Ni"/>
```

```
      </material>

      <material name="heavyConcrete">
        <D type="density" value="3.7" unit="g/cm3"/>
        <fraction n="0.65" ref="CaO"/>
        <fraction n="0.20" ref="SiO2"/>
        <fraction n="0.10" ref="Al2O3"/>
        <fraction n="0.05" ref="Fe2O3"/>
      </material>

      <material name="Radiation_safety_Concrete">
        <D type="density" value="3.7" unit="g/cm3"/>
        <fraction n="0.065" ref="CaO"/>
        <fraction n="0.03" ref="SiO2"/>
        <fraction n="0.005" ref="Al2O3"/>
        <fraction n="0.9" ref="Fe2O3"/>
      </material>

      <material name="Stainless_steel_1.4435">
        <D type="density" value="8" unit="g/cm3"/>
        <fraction n="0.0003" ref="C"/>
        <fraction n="0.01" ref="Si"/>
        <fraction n="0.02" ref="Mn"/>
        <fraction n="0.00045" ref="P"/>
        <fraction n="0.0003" ref="S"/>
        <fraction n="0.0011" ref="N"/>
        <fraction n="0.18" ref="Cr"/>
        <fraction n="0.03" ref="Mo"/>
        <fraction n="0.14" ref="Ni"/>
        <fraction n="0.61785" ref="Fe"/>
      </material>
    </materials>

    <solids>
      <!-- Beam Pipe -->
      <tube name="BeamPipe" rmin="33." rmax="35." z="4000."
          deltaphi="360" startphi="0" aunit="deg" lunit="mm"/>
      <!-- Beam Pipe Window -->
      <tube name="BeamPipeWindow" rmin="0" rmax="35." z="5.0
          deltaphi="360" startphi="0" aunit="deg" lunit="mm"/>
      <!-- Lead Shielding -->
      <box lunit="mm" name="LeadShieldingBox" x="800." y="275." z="200."/>
      <box lunit="mm" name="LeadShieldingHole" x="50." y="75." z="200." />
      <subtraction name="LeadShieldingWall">
        <first ref="LeadShieldingBox"/>
        <second ref="LeadShieldingHole"/>
```

```xml
    <positionref ref="Position_of_LeadShieldingHole" />
</subtraction>
<!-- Concrete Shielding -->
<box lunit="mm" name="ConcreteShieldingBox" x="800." y="350." z="200."/>
<box lunit="mm" name="ConcreteShieldingHole" x="50." y="100." z="200."/>
<subtraction name="ConcreteShieldingWall">
  <first ref="ConcreteShieldingBox"/>
  <second ref="ConcreteShieldingHole"/>
  <positionref ref="Position_of_ConcreteShieldingHole" />
</subtraction>
<!-- Concrete Shielding Fundament -->
<box lunit="mm" name="ConcreteFundament" x="800." y="1625." z="400."/>
<!-- Concrete Shielding SideBlock -->
<box lunit="mm" name="ConcreteSideBlock" x="400." y="1975." z="800."/>
<!-- Converter Target -->
<box lunit="mm" name="ConverterTarget" x="45." y="60." z="5."/>
<!-- Beam Pipe Window -->
<tube name="BeamPipeWindow2" rmin="0" rmax="52." z="0.1"
    deltaphi="360" startphi="0" aunit="deg" lunit="mm"/>
<!-- Beam Pipe -->
<tube name="BeamPipe2" rmin="50." rmax="52." z="276.25
    deltaphi="360" startphi="0" aunit="deg" lunit="mm"/>
<!-- Iron Pipe -->
<tube name="IronPipe" rmin="122.5" rmax="127." z="172.5"
    deltaphi="360" startphi="0" aunit="deg" lunit="mm"/>
<!-- Dipole Magnet -->
<!-- First Iron Layer -->
<box lunit="mm" name="FirstIronLayerWall" x="1100." y="806." z="7.5"/>
<tube name="FirstIronLayerHole" rmin="0." rmax="52." z="7.5
    deltaphi="360" startphi="0" aunit="deg" lunit="mm"/>
<subtraction name="FirstIronLayer">
  <first ref="FirstIronLayerWall"/>
  <second ref="FirstIronLayerHole"/>
  <positionref ref="center" />
</subtraction>
<!-- Iron Box -->
<box lunit="mm" name="IronBox" x="1100." y="806." z="1040."/>
<box lunit="mm" name="IronBoxHole" x="655." y="370." z="1040."/>
<subtraction name="IronSurrounding">
  <first ref="IronBox"/>
  <second ref="IronBoxHole"/>
  <positionref ref="center" />
</subtraction>
<!-- Upper Magnet Coil -->
<box lunit="mm" name="UpperCopperBlock" x="655." y="120." z="1040."/>
<box lunit="mm" name="UpperCopperBlockHole" x="250." y="120." z="635."/>
```

```
<subtraction name="UpperMagnetCoil">
  <first ref="UpperCopperBlock"/>
  <second ref="UpperCopperBlockHole"/>
  <positionref ref="center" />
</subtraction>
<!-- Lower Magnet Coil -->
<box lunit="mm" name="LowerCopperBlock" x="655." y="120." z="1040."/>
<box lunit="mm" name="LowerCopperBlockHole" x="250." y="120." z="635."/>
<subtraction name="LowerMagnetCoil">
  <first ref="LowerCopperBlock"/>
  <second ref="LowerCopperBlockHole"/>
  <positionref ref="center" />
</subtraction>
<!-- Iron Pole -->
<box lunit="mm" name="IronBlock" x="250." y="370." z="635."/>
<box lunit="mm" name="IronBlockHole" x="250." y="100." z="635."/>
<subtraction name="IronPole">
  <first ref="IronBlock"/>
  <second ref="IronBlockHole"/>
  <positionref ref="center" />
</subtraction>
<!-- Last Iron Layer -->
<box lunit="mm" name="LastIronLayerWall" x="1100." y="806." z="7.5"/>
<tube name="LastIronLayerHole" rmin="0." rmax="52." z="7.5
    deltaphi="360" startphi="0" aunit="deg" lunit="mm"/>
<subtraction name="LastIronLayer">
  <first ref="LastIronLayerWall"/>
  <second ref="LastIronLayerHole"/>
  <positionref ref="center" />
</subtraction>
<!-- Iron Pipe -->
<tube name="IronPipe2" rmin="122.5" rmax="127." z="240.
    deltaphi="360" startphi="0" aunit="deg" lunit="mm"/>
<!-- Beam Pipe -->
<tube name="BeamPipe3" rmin="50." rmax="52." z="222.5
    deltaphi="360" startphi="0" aunit="deg" lunit="mm"/>
<!-- Beam Pipe Connection -->
<!-- Beam Pipe Connection Lid -->
<tube name="BeamPipe_Lid" rmin="0." rmax="92." z="2.
    deltaphi="360" startphi="0" aunit="deg" lunit="mm"/>
<tube name="BeamPipe_Hole" rmin="0." rmax="52." z="2."
    deltaphi="360" startphi="0" aunit="deg" lunit="mm"/>
<subtraction name="BeamPipe_ConnectionLid">
  <first ref="BeamPipe_Lid"/>
  <second ref="BeamPipe_Hole"/>
  <positionref ref="BeamPipe_Connection_HolePosition1" />
```

```xml
</subtraction>
<!-- Beam Pipe Connection Pipe -->
<tube name="BeamPipe_ConnectionPipe" rmin="90." rmax="92." z="46."
    deltaphi="360" startphi="0" aunit="deg" lunit="mm"/>
<!-- Beam Pipe Connection Lid -->
<tube name="BeamPipe_Lid2" rmin="0." rmax="92." z="2."
    deltaphi="360" startphi="0" aunit="deg" lunit="mm"/>
<tube name="BeamPipe_Hole2" rmin="0." rmax="52." z="2."
    deltaphi="360" startphi="0" aunit="deg" lunit="mm"/>
<subtraction name="BeamPipe_ConnectionLid2">
  <first ref="BeamPipe_Lid2"/>
  <second ref="BeamPipe_Hole2"/>
  <positionref ref="BeamPipe_Connection_HolePosition2" />
</subtraction>
<!-- Beam Pipe -->
<tube name="BeamPipe_Kink" rmin="50." rmax="52." z="100."
    deltaphi="360" startphi="0" aunit="deg" lunit="mm"/>
<!-- Collimator -->
<!-- Horizontal Collimator -->
<box lunit="mm" name="HorizontalCollimatorBlock" x="260." y="150." z="125."/>
<box lunit="mm" name="HorizontalCollimatorHole" x="10." y="150." z="125."/>
<subtraction name="HorizontalCollimator">
  <first ref="HorizontalCollimatorBlock"/>
  <second ref="HorizontalCollimatorHole"/>
  <positionref ref="center" />
</subtraction>
<!-- Beam Pipe -->
<tube name="BeamPipe_Kink2" rmin="50." rmax="52." z="79."
    deltaphi="360" startphi="0" aunit="deg" lunit="mm"/>
<!-- Vertical Collimator -->
<box lunit="mm" name="VerticalCollimatorBlock" x="150." y="260." z="125."/>
<box lunit="mm" name="VerticalCollimatorHole" x="150." y="10." z="125."/>
<subtraction name="VerticalCollimator">
  <first ref="VerticalCollimatorBlock"/>
  <second ref="VerticalCollimatorHole"/>
  <positionref ref="center" />
</subtraction>
<!-- Beam Pipe -->
<tube name="BeamPipe_Kink3" rmin="50." rmax="52." z="6400."
    deltaphi="360" startphi="0" aunit="deg" lunit="mm"/>
<!-- Beam Pipe Window -->
<tube name="BeamPipeWindow3" rmin="0" rmax="52." z="0.1"
    deltaphi="360" startphi="0" aunit="deg" lunit="mm"/>
<!-- Concrete Wall -->
<box lunit="mm" name="ConcreteWallBlock" x="3000." y="3000." z="5000."/>
<tube name="ConcreteWallHole" rmin="0." rmax="52." z="5000."
```

```
        deltaphi="360" startphi="0" aunit="deg" lunit="mm"/>
   <subtraction name="ConcreteWall">
     <first ref="ConcreteWallBlock"/>
     <second ref="ConcreteWallHole"/>
     <positionref ref="center" />
   </subtraction>
   <!-- TB Collimator -->
   <box lunit="mm" name="TBCollimatorBlock" x="200." y="200." z="300."/>
   <box lunit="mm" name="TBCollimatorHole" x="5." y="5." z="300."/>
   <subtraction name="TBCollimator">
     <first ref="TBCollimatorBlock"/>
     <second ref="TBCollimatorHole"/>
     <positionref ref="center" />
   </subtraction>

   <!-- world volume -->
   <box lunit="mm" name="WorldBox" x="4500." y="4500." z="world_side" />
</solids>

<structure>
   <volume name="BeamPipe_vol">
     <materialref ref="Aluminium" />
     <solidref ref="BeamPipe" />
   </volume>
   <volume name="BeamPipeWindow_vol">
     <materialref ref="Aluminium" />
     <solidref ref="BeamPipeWindow" />
   </volume>
   <volume name="LeadShielding_vol">
     <materialref ref="Lead"/>
     <solidref ref="LeadShieldingWall"/>
   </volume>
   <volume name="ConcreteShielding_vol">
     <materialref ref="heavyConcrete"/>
     <solidref ref="ConcreteShieldingWall"/>
   </volume>
   <volume name="ConcreteFundament_vol">
     <materialref ref="heavyConcrete"/>
     <solidref ref="ConcreteFundament"/>
   </volume>
   <volume name="ConcreteSideBlock_vol">
     <materialref ref="heavyConcrete"/>
     <solidref ref="ConcreteSideBlock"/>
   </volume>
   <volume name="ConverterTarget_vol">
     <materialref ref="Copper"/>
```

```
    <solidref ref="ConverterTarget"/>
</volume>
<volume name="BeamPipeWindow2_vol">
  <materialref ref="Kapton"/>
  <solidref ref="BeamPipeWindow2"/>
</volume>
<volume name="BeamPipe2_vol">
  <materialref ref="Stainless_steel_1.4435"/>
  <solidref ref="BeamPipe2"/>
</volume>
<volume name="IronPipe_vol">
  <materialref ref="Iron"/>
  <solidref ref="IronPipe"/>
</volume>
<volume name="FirstIronLayer_vol">
  <materialref ref="Iron"/>
  <solidref ref="FirstIronLayer"/>
</volume>
<volume name="IronSurrounding_vol">
  <materialref ref="Iron"/>
  <solidref ref="IronSurrounding"/>
</volume>
<volume name="UpperMagnetCoil_vol">
  <materialref ref="Copper"/>
  <solidref ref="UpperMagnetCoil"/>
</volume>
<volume name="LowerMagnetCoil_vol">
  <materialref ref="Copper"/>
  <solidref ref="LowerMagnetCoil"/>
</volume>
<volume name="IronPole_vol">
  <materialref ref="Iron"/>
  <solidref ref="IronPole"/>
</volume>
<volume name="LastIronLayer_vol">
  <materialref ref="Iron"/>
  <solidref ref="LastIronLayer"/>
</volume>
<volume name="IronPipe2_vol">
  <materialref ref="Iron"/>
  <solidref ref="IronPipe2"/>
</volume>
<volume name="BeamPipe3_vol">
  <materialref ref="Stainless_steel_1.4435"/>
  <solidref ref="BeamPipe3"/>
</volume>
```

```
<volume name="BeamPipe_ConnectionLid_vol">
  <materialref ref="Stainless_steel_1.4435"/>
  <solidref ref="BeamPipe_ConnectionLid"/>
</volume>
<volume name="BeamPipe_ConnectionPipe_vol">
  <materialref ref="Stainless_steel_1.4435"/>
  <solidref ref="BeamPipe_ConnectionPipe"/>
</volume>
<volume name="BeamPipe_ConnectionLid2_vol">
  <materialref ref="Stainless_steel_1.4435"/>
  <solidref ref="BeamPipe_ConnectionLid2"/>
</volume>
<volume name="BeamPipe_Kink_vol">
  <materialref ref="Stainless_steel_1.4435"/>
  <solidref ref="BeamPipe_Kink"/>
</volume>
<volume name="BeamPipe_Kink2_vol">
  <materialref ref="Stainless_steel_1.4435"/>
  <solidref ref="BeamPipe_Kink2"/>
</volume>
<volume name="HorizontalCollimator_vol">
  <materialref ref="Tungsten_S17"/>
  <solidref ref="HorizontalCollimator"/>
</volume>
<volume name="VerticalCollimator_vol">
  <materialref ref="Tungsten_S17"/>
  <solidref ref="VerticalCollimator"/>
</volume>
<volume name="BeamPipe_Kink3_vol">
  <materialref ref="Stainless_steel_1.4435"/>
  <solidref ref="BeamPipe_Kink3"/>
</volume>
<volume name="BeamPipeWindow3_vol">
  <materialref ref="Kapton"/>
  <solidref ref="BeamPipeWindow3"/>
</volume>
<volume name="ConcreteWall_vol">
  <materialref ref="Radiation_safety_Concrete"/>
  <solidref ref="ConcreteWall"/>
</volume>
<volume name="TBCollimator_vol">
  <materialref ref="Lead"/>
  <solidref ref="TBCollimator"/>
</volume>

<volume name="tracking_volume" >
```

```
<materialref ref="Air" />
<solidref ref="WorldBox" />
<physvol>
   <volumeref ref="BeamPipe_vol" />
   <position name="BeamPipe_vol_position" x="0." y="0." z="2000." />
</physvol>
<physvol>
   <volumeref ref="BeamPipeWindow_vol" />
   <position name="BeamPipeWindow_vol_position" x="0." y="0." z="4002.5" />
</physvol>
<physvol>
   <volumeref ref="LeadShielding_vol" />
   <position name="LeadShielding_vol_position" x="-100." y="50." z="22670." />
</physvol>
<physvol>
   <volumeref ref="ConcreteShielding_vol" />
   <position name="ConcreteShielding_vol_position" x="-100." y="87.5" z="22870." />
</physvol>
<physvol>
   <volumeref ref="ConcreteFundament_vol" />
   <position name="ConcreteFundament_vol_position" x="-100." y="-900." z="22770." />
</physvol>
<physvol>
   <volumeref ref="ConcreteSideBlock_vol" />
   <position name="ConcreteSideBlock_vol_position" x="-700." y="-725." z="23270." />
</physvol>
<physvol>
   <volumeref ref="ConverterTarget_vol" />
   <position name="ConverterTarget_vol_position" x="0." y="0." z="23068.75" />
</physvol>
<physvol>
   <volumeref ref="BeamPipeWindow2_vol" />
   <position name="BeamPipeWindow2_vol_position" x="0." y="0." z="23396.25" />
</physvol>
<physvol>
   <volumeref ref="BeamPipe2_vol" />
   <position name="BeamPipe2_vol_position" x="0." y="0." z="23534.375" />
</physvol>
<physvol>
   <volumeref ref="IronPipe_vol" />
   <position name="IronPipe_vol_position" x="0." y="0." z="23586.25" />
</physvol>
<physvol>
   <volumeref ref="FirstIronLayer_vol" />
   <position name="FirstIronLayer_vol_position" x="0." y="0." z="23676.25" />
</physvol>
```

```
<physvol>
   <volumeref ref="IronSurrounding_vol" />
   <position name="IronSurrounding_vol_position" x="0." y="0." z="24200." />
</physvol>
<physvol>
   <volumeref ref="UpperMagnetCoil_vol" />
   <position name="UpperMagnetCoil_vol_position" x="0." y="125." z="24200." />
</physvol>
<physvol>
   <volumeref ref="LowerMagnetCoil_vol" />
   <position name="LowerMagnetCoil_vol_position" x="0." y="-125." z="24200." />
</physvol>
<physvol>
   <volumeref ref="IronPole_vol" />
   <position name="IronPole_vol_position" x="0." y="0." z="24200." />
</physvol>
<physvol>
   <volumeref ref="LastIronLayer_vol" />
   <position name="LastIronLayer_vol_position" x="0." y="0." z="24723.75" />
</physvol>
<physvol>
   <volumeref ref="IronPipe2_vol" />
   <position name="IronPipe2_vol_position" x="0." y="0." z="24847.5" />
</physvol>
<physvol>
   <volumeref ref="BeamPipe3_vol" />
   <position name="BeamPipe3_vol_position" x="0." y="0." z="24838.75" />
</physvol>
<physvol>
   <volumeref ref="BeamPipe_ConnectionLid_vol" />
   <position name="BeamPipe_ConnectionLid__vol_position" x="30." y="0." z="24951." />
</physvol>
<physvol>
   <volumeref ref="BeamPipe_ConnectionPipe_vol" />
   <position name="BeamPipe_ConnectionPipe__vol_position" x="30." y="0." z="24975." />
</physvol>
<physvol>
   <volumeref ref="BeamPipe_ConnectionLid2_vol" />
   <position name="BeamPipe_ConnectionLid2__vol_position" x="30." y="0." z="24999." />
</physvol>
<physvol>
   <volumeref ref="BeamPipe_Kink_vol" />
   <position name="BeamPipe_Kink_vol_position" x="35.92" y="0." z="25049.84" />
   <rotationref ref="RotatePassthrough" />
</physvol>
<physvol>
```

```
            <volumeref ref="HorizontalCollimator_vol" />
            <position name="HorizontalCollimator_vol_position" x="39.52" y="0." z="25162.28" />
            <rotationref ref="RotatePassthrough" />
        </physvol>
        <physvol>
            <volumeref ref="BeamPipe_Kink2_vol" />
            <position name="BeamPipe_Kink2_vol_position" x="42.78" y="0." z="25264.23" />
            <rotationref ref="RotatePassthrough" />
        </physvol>
        <physvol>
            <volumeref ref="VerticalCollimator_vol" />
            <position name="VerticalCollimator_vol_position" x="46.05" y="0." z="25366.17" />
            <rotationref ref="RotatePassthrough" />
        </physvol>
        <physvol>
            <volumeref ref="BeamPipe_Kink3_vol" />
            <position name="BeamPipe_Kink3_vol_position" x="150.43" y="0." z="28627.00" />
            <rotationref ref="RotatePassthrough" />
        </physvol>
        <physvol>
            <volumeref ref="BeamPipeWindow3_vol" />
            <position name="BeamPipeWindow3_vol_position" x="252.81" y="0." z="31825.41" />
            <rotationref ref="RotatePassthrough" />
        </physvol>
        <physvol>
            <volumeref ref="ConcreteWall_vol" />
            <position name="ConcreteWall_vol_position" x="163.18" y="0." z="29025.30" />
            <rotationref ref="RotatePassthrough" />
        </physvol>
        <physvol>
            <volumeref ref="TBCollimator_vol" />
            <position name="TBCollimator_vol_position" x="265.27" y="0." z="32214.67" />
            <rotationref ref="RotatePassthrough" />
        </physvol>
    </volume>
  </structure>

  <setup name="Default" version="1.0">
    <world ref="tracking_volume"/>
  </setup>

</gdml>
```

A.2.2.2. The XML file

```
<lccdd>
 <info name="TB line upt to horizontal and vertical collimators">
<comment>Simulation of test beam line up to collimators</comment>
 </info>

 <define>
   <!-- world -->
   <constant name="world_side" value="32370.*mm"/>
   <constant name="world_x" value="4500.*mm"/>
   <constant name="world_y" value="4500.*mm"/>
   <constant name="world_z" value="world_side"/>
   <!-- tracking region -->
   <constant name="tracking_region_radius" value="3000.*mm"/>
   <constant name="tracking_region_min" value="5.0*mm"/>
   <constant name="tracking_region_zmax" value="world_side"/>
   <!-- magnetic field strength -->
   <constant name="constBField" value="0.59"/>
 </define>

 <materials>
   <!-- Set the world material to air.  -->
   <material name="WorldMaterial">
     <D type="density" unit="g/cm3" value="0.001225"/>
     <fraction n="1.0" ref="Air"/>
   </material>
   <!-- Set tracking material to vacuum.  -->
   <material name="TrackingMaterial">
     <D type="density" unit="g/cm3" value="0.0000000000000001"/>
     <fraction n="1.0" ref="Vacuum"/>
   </material>
 </materials>

 <detectors>
   <detector id="1" name="PhantomTracker1" type="HPSTracker2" readout="PhantomTrackerHits">
     <comment>Phantom plane to register hits</comment>
     <module name="PhantomPlane1">
        <box x="1100.*mm" y="806.*mm"/>
        <module_component thickness="0.000000001*cm" material="Vacuum" sensitive="true">
           <dimensions x="1100.*mm" y="806.*mm"/>
        </module_component>
     </module>
     <layer id="2">
        <!-- before magnet -->
        <module_placement name="PhantomPlane1" id="0" x="0." y="0." z="23672.5*mm"
```

```
             rx="0" ry="0" rz="-PI/2"/>
    </layer>
</detector>
<detector id="2" name="PhantomTracker2" type="HPSTracker2" readout="PhantomTrackerHits2">
    <comment>Phantom plane to register hits</comment>
    <module name="PhantomPlane2">
        <box x="1100.*mm" y="806.*mm"/>
        <module_component thickness="0.000000001*cm" material="Vacuum" sensitive="true">
            <dimensions x="1100.*mm" y="806.*mm"/>
        </module_component>
    </module>
    <layer id="3">
        <!-- behind magnet -->
        <module_placement name="PhantomPlane2" id="0" x="0." y="0." z="24727.5*mm"
            rx="0" ry="0" rz="-PI/2"/>
    </layer>
</detector>
<detector id="3" name="MagnetFieldVolume" type="HPSTracker2" readout="MagnetFieldHits">
    <comment>Volume to set stepping limits</comment>
    <module name="FieldBox">
        <box x="250.*mm" y="100.*mm"/>
        <module_component thickness="710.*mm" material="Vacuum" sensitive="false">
            <dimensions x="250.*mm" y="100.*m"/>
        </module_component>
    </module>
    <layer id="1">
        <!-- inside magnet -->
        <module_placement name="FieldBox" id="0" x="0." y="0." z="24200."
            rx="0" ry="0" rz="-PI/2"/>
    </layer>
</detector>
<detector id="4" name="PhantomTracker3" type="HPSTracker2" readout="PhantomTrackerHits3">
    <comment>Phantom plane to register hits</comment>
    <module name="PhantomPlane3">
        <box x="300.*mm" y="300.*mm"/>
        <module_component thickness="0.000000001*cm" material="Vacuum" sensitive="true">
            <dimensions x="300.*mm" y="300.*mm"/>
        </module_component>
    </module>
    <layer id="4">
        <!-- behind horizontal collimator -->
        <module_placement name="PhantomPlane3" id="0" x="40." y="0." z="25226.0*mm"
            rx="0" ry="0" rz="-PI/2"/>
    </layer>
</detector>
<detector id="5" name="PhantomTracker4" type="HPSTracker2" readout="PhantomTrackerHits4">
```

```
      <comment>Phantom plane to register hits</comment>
      <module name="PhantomPlane4">
         <box x="300.*mm" y="300.*mm"/>
         <module_component thickness="0.000000001*cm" material="Vacuum" sensitive="true">
            <dimensions x="300.*mm" y="300.*mm"/>
         </module_component>
      </module>
      <layer id="5">
         <!-- behind vertical collimator -->
         <module_placement name="PhantomPlane4" id="0" x="46." y="0." z="25429.0*mm"
            rx="0" ry="0" rz="-PI/2"/>
      </layer>
   </detector>
   <detector id="6" name="PhantomTracker5" type="HPSTracker2" readout="PhantomTrackerHits5">
      <comment>Phantom plane to register hits</comment>
      <module name="PhantomPlane5">
         <box x="300.*mm" y="300.*mm"/>
         <module_component thickness="0.000000001*cm" material="Vacuum" sensitive="true">
            <dimensions x="300.*mm" y="300.*mm"/>
         </module_component>
      </module>
      <layer id="6">
         <!-- before final collimator -->
         <module_placement name="PhantomPlane5" id="0" x="265." y="0." z="32062.0*mm"
            rx="0" ry="0" rz="-PI/2"/>
      </layer>
   </detector>
   <detector id="7" name="PhantomTracker6" type="HPSTracker2" readout="PhantomTrackerHits6">
      <comment>Phantom plane to register hits</comment>
      <module name="PhantomPlane6">
         <box x="300.*mm" y="300.*mm"/>
         <module_component thickness="0.000000001*cm" material="Vacuum" sensitive="true">
            <dimensions x="300.*mm" y="300.*mm"/>
         </module_component>
      </module>
      <layer id="7">
         <!-- behind final collimator -->
         <module_placement name="PhantomPlane6" id="0" x="265." y="0." z="32366.0*mm"
            rx="0" ry="0" rz="-PI/2"/>
      </layer>
   </detector>
</detectors>

<readouts>
   <readout name="PhantomTrackerHits">
      <id>
```

```
            system:6,barrel:3,layer:4,module:12,sensor:1,side:32:-2,strip:12
      </id>
    </readout>
    <readout name="PhantomTrackerHits2">
      <id>
            system:6,barrel:3,layer:4,module:12,sensor:1,side:32:-2,strip:12
      </id>
    </readout>
    <readout name="MagnetFieldHits">
      <id>
            system:6,barrel:3,layer:4,module:12,sensor:1,side:32:-2,strip:12
      </id>
    </readout>
    <readout name="PhantomTrackerHits3">
      <id>
            system:6,barrel:3,layer:4,module:12,sensor:1,side:32:-2,strip:12
      </id>
    </readout>
    <readout name="PhantomTrackerHits4">
      <id>
            system:6,barrel:3,layer:4,module:12,sensor:1,side:32:-2,strip:12
      </id>
    </readout>
    <readout name="PhantomTrackerHits5">
      <id>
            system:6,barrel:3,layer:4,module:12,sensor:1,side:32:-2,strip:12
      </id>
    </readout>
    <readout name="PhantomTrackerHits6">
      <id>
            system:6,barrel:3,layer:4,module:12,sensor:1,side:32:-2,strip:12
      </id>
    </readout>
  </readouts>
  <fields>
    <field type="BoxDipole" name="TBDipole"
            x="0." y="0." z="24200." dx="100." dy="50.0" dz="355."
            lunit="Tesla" bx="0.0" by="constBField" bz="0.0"/>
  </fields>
  <includes>
    <gdmlFile file="Pipe_LeadShielding_Converter_Magnet_Collimator_WALL_TBCollimator.gdml"/>
  </includes>
</lccdd>
```

Bibliography

[1] Table of the DESY Test Beam Magnet settings. `http://testbeam.desy.de/e130574/e130575/e131178/e131191/MagnetSettings.pdf`, .

[2] Dr. Marcel Stanitzki (DESY). *The DESY testbeam facility*. June 30, 2014.

[3] Official webpage of the Helmholtz Association. `http://www.helmholtz.de/`.

[4] Description of the DESY Test Beam Attributes. Map of the DESY-II tunnel and the test beam lines. `http://testbeam.desy.de/e130573/e130905/e130916/hall2-beamequipment-a0.pdf`, .

[5] K.A. Olive et al. (Particle Data Group). *Review of Particle Physics*, volume 38. 2014. doi: 10.1088/1674-1137/38/9/090001. URL `http://pdg.lbl.gov/2014/download/rpp2014-Chin.Phys.C.38.090001.pdf`.

[6] The National Institute of Standards and Technology - List of excitation energies of certain materials. `http://physics.nist.gov/PhysRefData/XrayMassCoef/tab1.html`.

[7] PDG, Atomic and Nuclear Properties of Materials: Energy loss of particles. `http://physics.nist.gov/PhysRefData/Star/Text/ESTAR.html`, `http://pdg.lbl.gov/2013/AtomicNuclearProperties/index.html`.

[8] Yung-Su Tsai. Pair production and bremsstrahlung of charged leptons. *Rev. Mod. Phys.*, 46:815–851, Oct 1974. doi: 10.1103/RevModPhys.46.815. URL `http://link.aps.org/doi/10.1103/RevModPhys.46.815`.

[9] Ludwig Bergmann, Clemens Schaefer, Herausgegeben Von Wilhelm Raith, Mit Beitragen Von H. Kleinpoppen, N. Risch, and M. Fink. *Lehrbuch Der Experimentalphysik: Band 4: Bestandteile Der Materie: Atome, Molekule, Atomkerne, Elementarteilchen (German Edition)*. Walter De Gruyter Inc, 2003. ISBN 3110168006.

[10] Klaus Wille. *The Physics of Particle Accelerators: An Introduction*. Oxford University Press, 2001. ISBN 0198505507.

[11] John David Jackson. *Classical Electrodynamics Third Edition*. Wiley, 1998. ISBN 9780471309321.

[12] DESY-II synchrotron radiation spectrum. Private communication with Ulrich Kötz, DESY.

[13] G. C. Baldwin and G. S. Klaiber. Photo-fission in heavy elements. *Phys. Rev.*, 71:3–10, Jan 1947. doi: 10.1103/PhysRev.71.3. URL `http://link.aps.org/doi/10.1103/PhysRev.71.3`.

[14] B. L. Berman and S. C. Fultz. Measurements of the giant dipole resonance with monoenergetic photons. *Rev. Mod. Phys.*, 47:713–761, Jul 1975. doi: 10.1103/RevModPhys.47.713. URL `http://link.aps.org/doi/10.1103/RevModPhys.47.713`.

[15] M. Goldhaber and E. Teller. On nuclear dipole vibrations. *Phys. Rev.*, 74:1046–1049, Nov 1948. doi: 10.1103/PhysRev.74.1046. URL `http://link.aps.org/doi/10.1103/PhysRev.74.1046`.

[16] Description of the LINAC-II and PIA at DESY. `http://petra3-project.desy.de/storage_ring/work_packages/pre_accelerators/linac_ii_and_pia/index_eng.html`.

[17] William W MacKay Mario Conte. *An Introduction to the Physics of Particle Accelerators*. World Scientific Publishing Co. Pte. Ltd., Singapore, second edition, 2008. ISBN 9812779604.

[18] DESY-II beam parameters. Private communication with Heiko Ehrlichmann, DESY MDE, Leader of Machine-Division group for the DESY-II synchrotron accelerator.

[19] Scheme of the DESY Test Beam generation. Cf. `http://testbeam.desy.de/e130573/e130913/testbeamlayout.pdf` - redesigned by Phillip Hamnett, PhD, DESY, January 2015.

[20] Description of the DESY Test Beam, list of available secondary targets for the test beam lines. `http://testbeam.desy.de/e130574/e130922/conversion_targets.pdf`, .

[21] Description of the DESY Test Beam, beam rates of test beam 21. `http://testbeam.desy.de/sites2009/site_testbeam/content/e130573/e130791/e183839/rate_vs_p_t21.gif`, .

[22] Paul Schütze. *Energy calibration of the DESY test beam in beamline 21*. September 11, 2013. URL `http://www.desy.de/f/students/2013/reports/schuetze.pdf.gz`.

[23] Technical drawings for test beam magnet MR. `http://testbeam.desy.de/e130575/e131178/e131193/MR-Data-6Pages.pdf`.

[24] Simulator for the Linear Collider (SLIC). `http://www.lcsim.org/software/slic/`.

[25] The official SLIC FAQ website. `https://confluence.slac.stanford.edu/display/ilc/SLIC+FAQ`, .

[26] Manual for the Geant4 General Particle Source. `https://geant4.web.cern.ch/geant4/UserDocumentation/UsersGuides/ForApplicationDeveloper/html/ch02s07.html`.

[27] Geant4 physics list LCPhys. `https://confluence.slac.stanford.edu/display/ilc/What+is+LCPhys`, .

[28] SAP 3D Visual Enterprise Viewer. `https://store.sap.com/sap/cpa/ui/resources/store/html/SolutionDetails.html?pid=0000012810`.

[29] ILCSoft Documentation. `http://ilcsoft.desy.de/portal`.

[30] LCIO Documentation. `http://lcio.desy.de/v01-07/doc/doxygen_api/html/classEVENT_1_1LCIO.html`.

[31] 42. Monte Carlo particle numbering scheme. `http://pdg.lbl.gov/2014/reviews/rpp2014-rev-monte-carlo-numbering.pdf`.

[32] Description of the DESY Test Beam Attributes. Primary target holder. `http://testbeam.desy.de/e130573/e130905/`.

[33] Geant4 Users' Guide. `https://geant4.web.cern.ch/geant4/UserDocumentation/UsersGuides/ForApplicationDeveloper/html/ch05s03.html`.

Acknowledgements